THE UNIVERSITY *of* EDINBURGH

School of Biological Sciences

Self-organisation in mixtures of microtubules and motor proteins

Ivan Maryshev

Thesis submitted in the fulfilment of the requirements for the degree of Doctor (Ph.D.) in Sciences.

Supervisor: Prof. A. Goryachev
Co-supervisor: Prof. D. Marenduzzo

Edinburgh, 2018

Contents

Физик испытывает природу.
Что испытывает к нему природа — догадаться нетрудно.
Александр Кондратьев

Abstract

Self-organisation of mixtures of biological polymers and molecular motors provides a fascinating manifestation of active matter. Microtubules re-oriented by the molecular motors can form far-from-equilibrium cell-scale structures, such as the mitotic spindle apparatus. It is believed that different motor types favour formation of distinct patterns: clustering motors control the formation of spindle poles and asters, while microtubule-sliding motors organise antiparallel bundles presenting in the spindle central part.

The link between individual microscopic motor-induced interactions of filaments and the macroscopic dynamics at cell-size scales is poorly understood. Here we enhance our understanding of this problem and formulate a theoretical approach, based on a Boltzmann-like kinetic equation, to describe pattern formation in two-dimensional mixtures of microtubular filaments and molecular motors.

In the first part of the thesis, we derive hydrodynamic equations that govern the collective behaviour of microtubules in the presence of clustering motors. We build on a kinetic method developed earlier by Aranson and Tsimring and model the motor-induced reorientation of microtubules as collision rules. The procedure of coarse-graining yields a set of equations for local density and orientation of the microtubules. We study its behaviour by performing a linear stability analysis and direct numerical simulations. We discuss the observed patterns including asters and chaotic stripe-like structures and consider the ensuing phase diagram.

In the second part of this study, we consider molecular motors which can push apart antiparallel microtubules and cluster parallel ones. Using the developed approach, we obtain a set of equations for the microtubular density, orientation, and tensor of alignment. Through numerical simulations, we show that this model generically creates either stable stripes with the antiparallel arrangement of filaments inside them or an ever-evolving pattern where stripes periodically form, rotate, self-extend and then split up. We derive a minimal model which displays the same instability as the full model and clarifies the underlying mechanism. We argue that our minimal model unifies various previous observations of chaotic behaviour in the dry active matter into a general universality class.

Finally, we discuss obtained models, compare them to identify common features, and offer the directions of future advances.

Acknowledgement

I would like to thank my scientific advisors, Prof. Andrew Goryachev and Prof. Davide Merrenduzzo. I also would like to express my sincere gratitude to Dr. Alexander Morozov, whose contribution to this work is hard to overestimate. It has been an honour to be a PhD student under the supervision of these outstanding scientists. I am very grateful for their knowledge and, particularly, for their vision of science that they have shared with me.

I am grateful to Dr. Teuta Pilizota for the support and concern. Discussions with Prof. Igor Aranson and Dr. Lev Tsimring are also kindly acknowledged.

I would like to thank my family. I am especially grateful to my beloved sister Dr. Alina Dubovskaya who inspired me to become a scientist.

I also thank my friends Dr. Ivan Erofeev and Illya Ivanov for personal support.

I thank all my teachers and mentors.

Finally, I want to express my gratitude to the closest friend of my life, my wife.

Declaration

Except otherwise stated, the research undertaken in this thesis was the work of the author.

Parts of this thesis have been published (Maryshev et al. Phys. Rev. E **97** (2), 022412, 2018).

Ivan Maryshev

21 December 2018

Introduction

Immanuel Kant defined life as a "self-organised, self-reproducing" process in 1790 [1]. Nowadays this definition becomes more and more profound, and the origin of ordered states and associated functions is one of the most fundamental problems in biology [2].

The self-organisation in biological systems is dynamic; it emerges from the collective behaviour of the active 'agents' and usually implies energy dissipation. Note, that dynamics is defined by the character of interaction between agents rather than by the properties of agents themselves. This phenomenon can be found at all levels of the biological hierarchy, including cellular and intracellular structures such as the microtubular cytoskeleton.

Microtubular cytoskeleton plays a crucial role in all eukaryotic cells. It not only helps to shape the cell and provides tracks for the intracellular transport but also orchestrates many spatiotemporal processes in the cell. Self-organization in this case arises from the collective behaviour of microtubules (MTs) and molecular motors (MMs) [3] with the energy input obtained from the hydrolysis of adenosine triphosphate (ATP). Microtubules can be organised into many special structures that are connected with different cellular functions. For example, during mitosis, MTs, molecular motors work cooperatively to construct a mitotic spindle [4].

Microtubules control intracellular traffic of molecular motors. In turn, MTs transport and orientation are themselves controlled by the heterogeneous distribution of molecular motors. Because of this feedback, the dynamics of the microtubular cytoskeleton can be considered as a new type of pattern formation process [3].

Spontaneous transitions to various ordered states and patterns has been extensively studied in several *in vitro* experiments with cell extracts [5, 6] and in the reconstituted systems with purified components, such as quasi 2-dimensional motor-microtubule solution [7–11]. These well-controlled *in vitro* assays recapitulate the formation of microtubular structures with a polar [7–9] or nematic [10, 11] order, and provide a promising platform for an investigation of the pattern formation in MT cytoskeleton. The motivation for this work is to enhance the understanding of self-organisation processes in the MT cytoskeleton from the bottom up, and it is this type of systems will be considered further in the current thesis.

It is currently believed that different types of motors enable distinctive rules of interaction between microtubules. The details of such interactions are understood to a certain degree [12], e.g. motors can cluster parallel filaments and push apart antiparallel ones, or prefer one of these interactions. However, it is presently unclear how the particular interaction type gives rise to the partic-

ular macroscopic pattern formation. Consequently, the theoretical description of microtubule-motor mixtures is stymied by the paucity of approaches able to connect individual microscopic motor-induced interactions of filaments to the macroscopic dynamics. The main goal of this thesis is to create an adequate mean-field formalism and computational tools to bridge these to scales.

The fundamental principles by which a group of interacting agents evolves to a particular dynamic spatial pattern are intensively investigated in the active matter physics [13, 14]. This framework provides a promising tool for a theoretical investigation of collective behaviour including the self-organisation processes in MT-MM mixtures, and inherent instabilities.

Multiple approaches had been developed in the active matter physics to advance our understanding of the dynamics typical of microtubule-motor mixtures. Besides direct agent-based simulations [8, 15], mean field equations have been derived first on the basis of symmetry considerations [16–18], and from the detailed microscopic rules of interaction [19–22]. The latter avenue is useful as it allows one to determine the effective parameters of the continuum theory in terms of the geometrical and physical quantities appearing in the microscopic model.

In the kinetic approach employed by Aranson and Tsimring [19, 23, 24], pairwise motor-mediated interactions of microtubules were treated as instantaneous collisions. These authors considered plus-directed clustering motors, which can align microtubules in a parallel way. Hydrodynamic equations for slow variables, filament concentration and orientation, were derived by coarse-graining of the corresponding Boltzmann-type equation for the probability distribution function (PDF).

In this thesis we revisit this technique. Firstly, we develop our formalism and consider mixtures of MTs and clustering motors; then we use our theory to derive equations governing the pattern formation in microtubules in the presence of molecular motors providing both clustering and sliding of MTs.

Thesis Outline

In **Chapter 1**, we introduce ingredients of our model and provide the analysis of literature. We describe microtubules, multivalent molecular motors, and their mechanochemical cycle. Then we consider motor-induced interactions between the microtubules. We catalogue microtubular structures experimentally observed *in vivo* and *in vitro*. Next, we concentrate on the MM-MT mixtures and associated instabilities. We also discuss MT pattern formation in terms of the active matter physics and introduce the brief classification of active matter models of the MT cytoskeleton. Finally, we justify the choice of dry kinetic model for the MT-MM mixtures investigation.

In **Chapter 2**, we derive hydrodynamic equations that govern the collective behaviour of microtubules in the presence of clustering motors. We build on a kinetic method developed earlier by Aranson and Tsimring [19, 23] and model the motor-induced reorientation of microtubules as collision rules. We introduce our kinetic model, re-derive the hydrodynamic equations obtained in [19] and critically discuss the approximations used in this derivation. We demonstrate that the model exhibits bundling instability and argue for the need to include excluded volume effects and present the derivation of such excluded volume terms. Then we discuss the evaluation of the interaction integrals. Our equations of motion are presented in the Section 2.5: these are derived according to two different types of closure. We perform a stability analysis of the equations of motion corresponding to both these closure schemes, present the corresponding phase diagrams, and provide the results of numerical simulations. The last section contains a discussion of the obtained model.

In **Chapter 3**, we consider molecular motors which can push apart antiparallel microtubules and cluster parallel ones. Using the approach developed in Chapter 2, we obtain a set of equations for the microtubular density, orientation, and tensor of alignment. Through the numerical simulationst we show that this model generically creates either stable stripes with the antiparallel arrangement of filaments inside them or a never-settling pattern where stripes periodically form, rotate and then split up. We derive a minimal model which displays the same instability as the full model and dissect the underlying mechanisms. We argue that our minimal model unifies various previous observations of chaotic behaviour in the dry active matter into a general universality class. The last Section contains a discussion of the obtained model.

Finally, in a short **Summary** we briefly recapitulate the results. We discuss the common features and discrepancies between obtained models, draw the contours of possible advances, and highlight the sphere of application.

References

[1] E. Kant, "Critique de la faculté de juger (1790)," *L. Delamarre, etc., Paris Gall.*, 1985.

[2] E. Karsenti, "Self-organization in cell biology: a brief history," *Nat. Rev. Mol. Cell Biol.*, vol. 9, no. 3, pp. 255–262, 2008.

[3] J. Howard, S. W. Grill, and J. S. Bois, "Turing's next steps: the mechanochemical basis of morphogenesis," *Nat. Rev. Mol. Cell Biol.*, vol. 12, pp. 400–406, 2011.

[4] A. Mogilner and E. Craig, "Towards a quantitative understanding of mitotic spindle assembly and mechanics," *J. Cell Sci.*, vol. 123, pp. 3435–3445, 2010.

[5] P. A. Nguyen, A. C. Groen, M. Loose, *et al.*, "Spatial organization of cytokinesis signaling reconstituted in a cell-free system," *Science (80-.).*, vol. 346, pp. 244–247, 2014.

[6] J. Brugués and D. Needleman, "Physical basis of spindle self-organization.," *Proc. Natl. Acad. Sci. U. S. A.*, vol. 111, pp. 18496–500, 2014.

[7] F. J. Nédélec, T. Surrey, a. C. Maggs, and S. Leibler, "Self-organization of microtubules and motors.," *Nature*, vol. 389, no. September, pp. 305–308, 1997.

[8] T. Surrey, "Physical Properties Determining Self-Organization of Motors and Microtubules," *Science (80-.).*, vol. 292, no. 5519, pp. 1167–1171, 2001.

[9] C. Hentrich and T. Surrey, "Microtubule organization by the antagonistic mitotic motors kinesin-5 and kinesin-14," *J. Cell Biol.*, vol. 189, no. 3, pp. 465–480, 2010.

[10] T. Sanchez, D. Welch, D. Nicastro, and Z. Dogic, "Cilia-Like Beating of Active Microtubule Bundles," *Science (80-.).*, vol. 333, pp. 456–459, 2011.

[11] T. Sanchez, D. T. N. Chen, S. J. Decamp, M. Heymann, and Z. Dogic, "Spontaneous motion in hierarchically assembled active matter," *Nature*, vol. 491, no. 11591, pp. 1–5, 2012.

[12] R. A. Cross and A. McAinsh, "Prime movers: the mechanochemistry of mitotic kinesins," *Nat. Rev. Mol. Cell Biol.*, vol. 15, no. 4, pp. 257–271, 2014.

[13] M. C. Marchetti, J.-F. Joanny, S. Ramaswamy, *et al.*, "Hydrodynamics of soft active matter," *Rev. Mod. Phys.*, vol. 85, no. 3, p. 1143, 2013.

[14] S. Ramaswamy and R. A. Simha, "The mechanics of active matter: Broken-symmetry hydrodynamics of motile particles and granular layers," *Solid State Commun.*, vol. 139, no. 11-12, pp. 617–622, 2006.

[15] R. Loughlin, R. Heald, and F. Nédélec, "A computational model predicts Xenopus meiotic spindle organization," *J. Cell Biol.*, vol. 191, pp. 1239–1249, 2010.

[16] H. Y. Lee and M. Kardar, "Macroscopic equations for pattern formation in mixtures of microtubules and molecular motors," *Phys. Rev. E*, vol. 64, no. 5, p. 056113, 2001.

[17] S. Sankararaman, G. I. Menon, and P. B. Sunil Kumar, "Self-organized pattern formation in motor-microtubule mixtures," *Phys. Rev. E*, vol. 70, p. 031905, 2004.

[18] E. Putzig, G. S. Redner, A. Baskaran, and A. Baskaran, "Instabilities, defects, and

defect ordering in an overdamped active nematic," *Soft Matter*, vol. 12, no. 17, pp. 3854–3859, 2016.

[19] I. S. Aranson and L. S. Tsimring, "Theory of self-assembly of microtubules and motors," *Phys. Rev. E*, vol. 74, p. 31915, 2006.

[20] T. B. Liverpool and M. C. Marchetti, "Instabilities of Isotropic Solutions of Active Polar Filaments," *Phys. Rev. Lett.*, vol. 90, p. 138102, 2003.

[21] A. Ahmadi, M. C. Marchetti, and T. B. Liverpool, "Hydrodynamics of isotropic and liquid crystalline active polymer solutions," *Phys. Rev. E*, vol. 74, p. 061913, 2006.

[22] M. J. Shelley, "The Dynamics of Microtubule/Motor-Protein Assemblies in Biology and Physics," *Annu. Rev. Fluid Mech.*, vol. 48, pp. 487–506, 2016.

[23] I. S. Aranson and L. S. Tsimring, "Pattern formation of microtubules and motors: Inelastic interaction of polar rods," *Phys. Rev. E*, vol. 71, p. 050901, 2005.

[24] F. Ziebert, I. S. Aranson, L. S. Tsimring, *et al.*, "Effects of cross-links on motor-mediated filament organization," *New J. Phys.*, vol. 9, p. 421, 2007.

Chapter 1

Aspects of active microtubular cytoskeleton

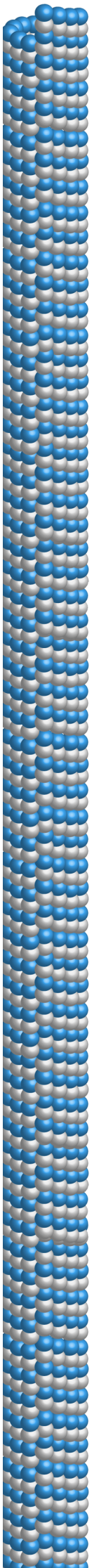

Abstract

In this Chapter, we introduce ingredients of our model and provide the analysis of literature. We describe microtubules, multivalent molecular motors, and their mechanochemical cycle. Then we consider motor-induced interactions between the microtubules. We catalogue microtubular structures experimentally observed *in vivo* and *in vitro*. Next, we concentrate on the MM-MT mixtures and associated instabilities. We also discuss MT pattern formation in terms of the active matter physics and introduce the brief classification of active matter models of the MT cytoskeleton. Finally, we justify the choice of dry kinetic model for the MT-MM mixtures investigation.

1.1 Microtubules

Microtubules can be found in all dividing eukaryotic cells, most of the differentiated cell types [1]. They are formed by the polymerisation of tubulin heterodimers [2]. Individual tubulin consists of two monomers called α- and β-subunits [3]. Within a MT tubulins arrange in linear protofilaments keeping "orientation": α-subunit of one tubulin always attaches to the β-subunit of another one.

Protofilaments in turn associate side by side to form hollow cylindrical structure [4]. MTs assembled *in vitro* can contain 10-15 protofilaments, however MTs obtained *in vivo* have mostly 13 protofilaments. The outer diameter of such "straw-like" macromolecule is about 25 nm; inner diameter is 14 nm, the length can reach tens of μm. It is the largest and the stiffest type of cytoskeletal biopolymers: persistence length of the filament may be as much as few μm (Fig. 1.1).

One of the most interesting properties of MTs is their "polarity" - anisotropy, created by the head-to-tail polymerisation of tubulin. The two ends of microtubule are distinguishable since they have different tubulin subunits pointing outside. The end of an MT corresponding to the β-subunit is called "$+$"-end; the other one is denoted as "$-$"-end. Moreover, the orientation of MT can be distinguished at each point, e.g. by the head of directed cytoskeletal motor. By analogy with the electrostatics, the orientation vector is set to point from the "$-$"-end to the "$+$"-end.

Polarity plays a crucial role in MT cytoskeleton, enabling directed transport, cell motility and chromosome segregation. It also provides a rich behaviour during the formation of large-scale patterns such as mitotic spindle apparatus.

Besides polarity, MTs also possess chiral symmetry. Since protofilaments constituting the "tube" are shifted in respect to each other, they form the left-handed pseudo-helix [5]; however, the chirality of MTs is usually neglected.

The individual filament can stochastically switch between states of assembly and disassembly. This non-equilibrium phenomenon involving the GTP molecules hydrolysis is known as "dynamic instability" [1]. Change of length can take place at both MT ends, but *in vivo* growth and shrinkage occur faster at the "$+$"-end, while the "$-$"-end is usually stabilised by the "γ"-tubulin ring.

The dynamic instability can be blocked by "+"-end cap proteins [6] or drugs such as taxol, and the length of some MTs may remain fixed for hours both *in vivo* and *in vitro*. For simplicity and better control, *in vitro* experiments often involve filament of fixed length. Moreover, data are indicating that MT stabilisation does not prevent cell mitosis [7].

This research will be restricted to the stabilised filaments. The ability of

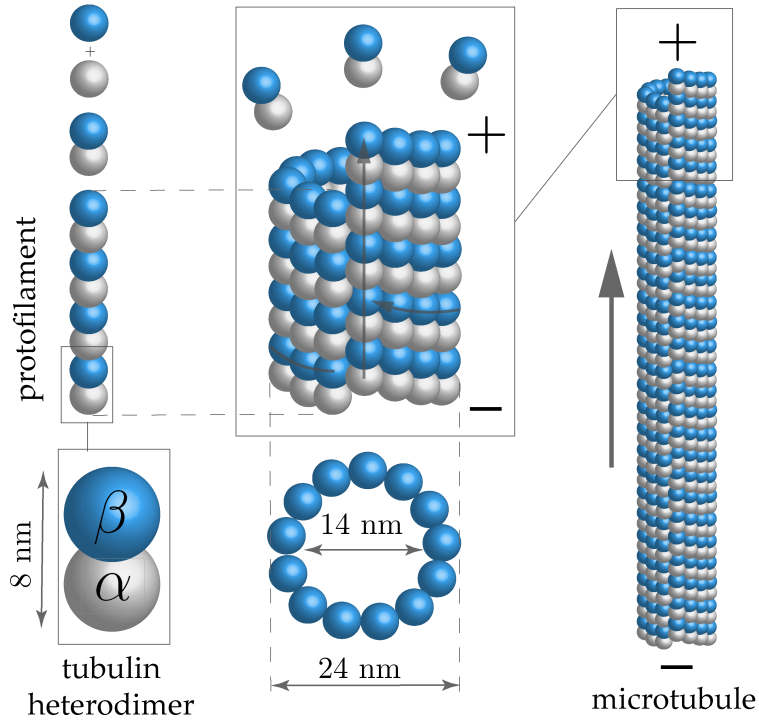

Figure 1.1: Structure of microtubule biofilament. 13 protofilaments surround a hollow centre forming a tube-like structure. The ring depicts a microtubule in cross-section

individual MT to grow consuming energy from the hydrolysis of Guanosine triphosphate, and associated with that active behaviour, will be left outside the scope. By the activity we will mean the nonequilibrium behaviour of the MT cytoskeleton caused by the motor-induced interaction between filaments. Molecular motors necessary for that type of activity are discussed in the following section.

1.2 Molecular motors

Motors can perform mechanical work by consuming energy. By analogy, protein machines able to convert chemical energy into the motion are called biological molecular motors. Unlike macroscopic motors, they operate on the microscopic scale, which makes thermally induced fluctuations significant.

The cytoskeletal motor is an example of a protein able to move along filaments using ATP hydrolysis. Different types of motors are associated with different types of cytoskeletal filaments. MT-following proteins of kinesin [8] and dynein families can walk along MT filaments, transport cargo along them, or significantly change their respective position and orientation. It is that type of proteins that will be called molecular motors in the following text.

Kinesin motors form a superfamily, in this Chapter we use standardised nomenclature [9] containing 14 subfamilies. Describing motors, we will call

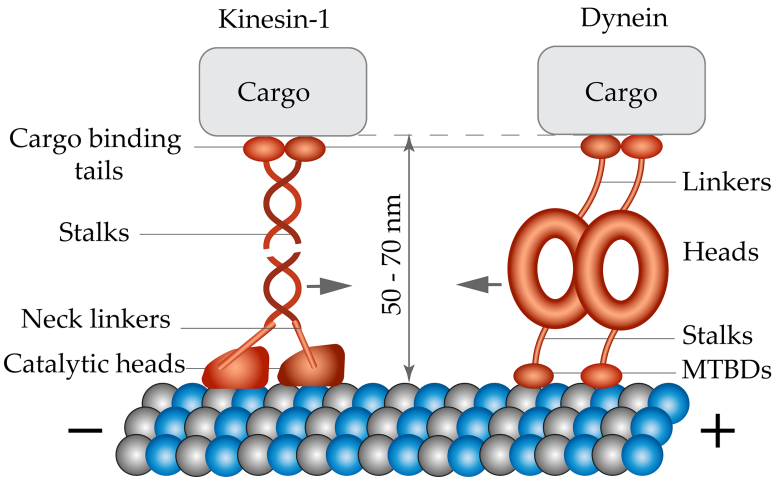

Figure 1.2: Comparison of kinesin and dynein motors structure.

them by the family name (e.g., "kinesin-1 motor" or just "kinesin-1" instead of "members of kinesin-1 subfamily").

Both kinesin and dynein molecular motors usually have the length of few tens of nm (Fig. 1.2), exert forces of several pN, their velocity depends on ATP concentration and varies from few tens to few hundreds of um per second [10–12]. Kinetics of motors binding, their processivity (parameter, describing how long individual motor can "walk" along the MT) vary among different motor types.

Motors prefer to walk along MT track in one direction. Most of the processive kinesins move toward the "+"-end while all dyneins and kinesin-14 motors, being an exception, go toward the "−"-end. In this work, we will refer to them as plus-directed and minus-directed motors, respectively.

Typical kinesin (e.g. kinesin-1) is a homodimer (Fig. 1.2) of two heavy chains, each chain, in turn, has three important parts [13, 14]:

1. catalytic motor domain (head), also referred to as the "head". Each head is characterised by the presence of two binding sites, one for ATP and one for the MT. With some exceptions, the motor domain is located at the N-terminus and is followed by neck linker,

2. a long (60–80 nm) part with alternating flexible and coiled segments called "stalk",

3. cargo-binding domain, typically situated at the C-terminus. This globular part determining the cargo type is called "tail". In different motors, this domain can bind vesicles, organelles, protein complexes, or another MT.

Dynein motors have a slightly different structure (Fig. 1.2). Catalytic Motor domains of dynein are connected with large motor heads by the "stalks". Motor heads, in turn, are linked to the cargo-binding domain.

1.2.1 Mechanical cycle of molecular motors

So how does MT-following MM move or generate a force? Existing models can be reduced to two explanations: conformational change (or so-called "lever arm") mechanism and Brownian ratchet; and both of them may take place.

Experimental data demonstrate that mechanical cycle of stepping MMs usually contains 4 phases [15]: diffusional search, binding, conformational change, and release (Fig. 1.3). Moreover, this cycle is driven by the ATP hydrolysis [11, 12].

To illustrate the mechanical cycle of MM, consider the existing model of stepping kinesin:

- initial configuration: one motor head (head 1) of a dimer is associated to the tubulin heterodimer, the unbound one (head 2) is in ADP associated state,
- phase 1: the binding of head 1 with the ATP releases free motor head (head 2) and it starts the diffusional search,
- phase 2: free motor head (head 2) binds adjacent tubulin heterodimer and releases ADP; it should complete it before head 1 finishes the hydrolysis of ATP.
- phase 3: conformational changes in linkers and occurring strains modify catalytic properties of heads, e.g. preventing ATP binding in the front head (head 2),
- phase 4: head, initially associated with MT (head 1), releases it and put front head (head 2) in an ATP-waiting state.

Experiments with optical traps [16] have demonstrated that "step" of kinesin motors equals 8nm, it corresponds to the size of tubulin heterodimer. Their velocity depends on the concentration of ATP molecules and the load. Velocity can vary from tens of nm per second to hundreds of μm per second [11].

Individual motors can exert the force of pN order. The stall force, maximal load above which motor cannot walk any more, ranges from 2 to 7 pN.

Mechanochemical properties of the dynein motors appear to be similar [12].

1.2.2 Multivalent motors and motor-induced interactions

Multivalent motors are proteins able to associate with two MTs simultaneously. Multivalent MMs are essential for the following research since they use the local input of energy and move MTs in respect to each other, driving the MT cytoskeleton out of equilibrium. The event of translocation and reorientation of two MTs by the group of MMs will be called motor-induced interaction.

Interaction with two MTs at the same time can be implemented in several ways: 1) dimeric motor stepping along one MT can use the other one as a cargo, 2) one motor being tetrameric, and therefore having two pairs of motor

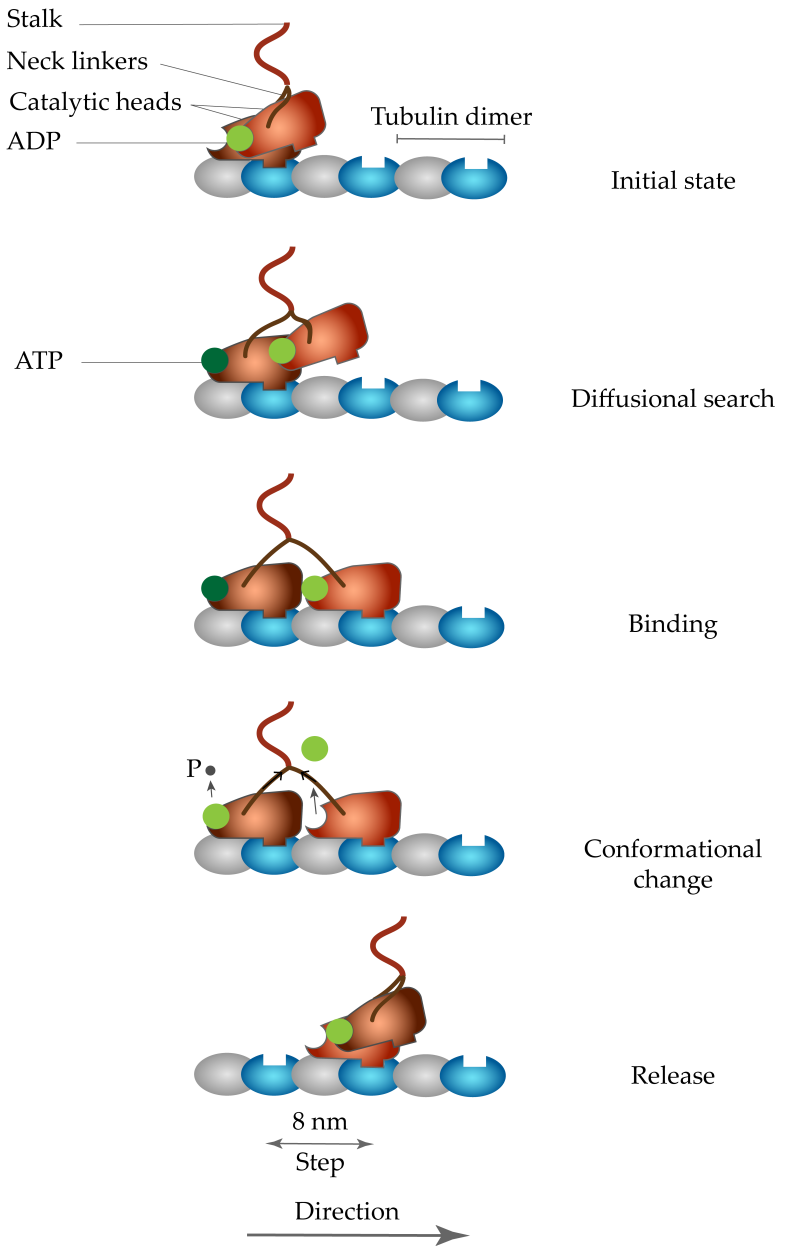

Figure 1.3: Mechanism of the kinesin movement. Phases of the mechanical cycle: initial configuration, diffusional search, binding, conformational change, release.

domains, walks along the two MT the same time. Exotic scenario, involving one dimeric motor, stepping along two MTs simultaneously [17], is left outside the scope.

To illustrate discussed mechanisms, one can consider two important multivalent kinesin families – kinesin-14 dimeric motors and kinesin-5 tetrameric motor – and discuss associated motor-induced interactions. It is currently believed that these motor types play crucial role in the self-organisation of the bipolar mitotic spindle [18, 19].

Dimeric motors kinesin-14

Kinesin-14 proteins (e.g., *Drosophila melanogaster* NCD) are dimeric multivalent motors having motor domains at C-terminus [20] and the MT-binding non-motor domains at the N-terminus (Fig. 1.4). Proteins of this family walk toward the microtubule "−"-end, as it was mentioned previously.

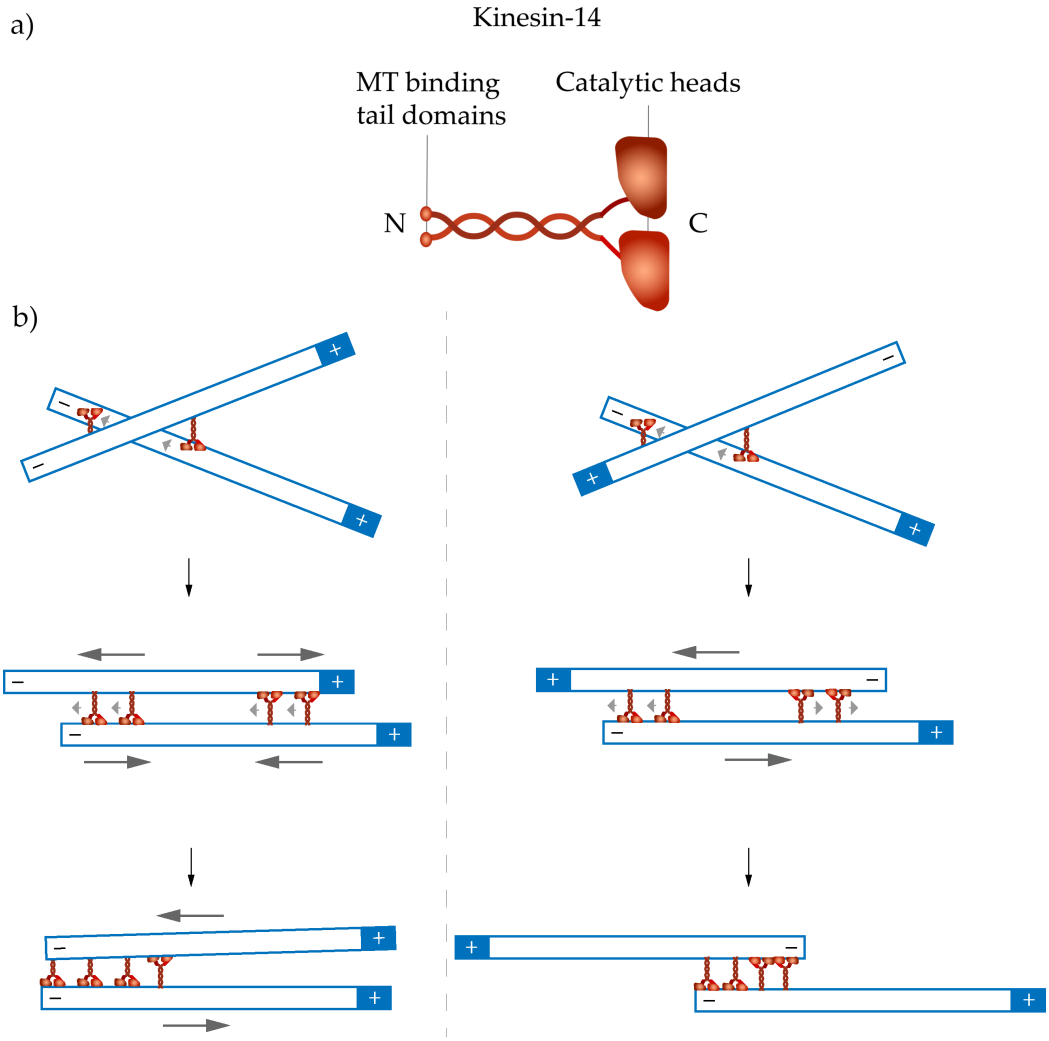

Figure 1.4: A) schematic structure of kinesin-14. Kinesin-14 is the minus-directed dimeric multivalent motor, containing motor heads at the N-terminus and microtubule-associated non-catalytic tails at the C-terminus; b) interaction between two MTs via minus directed motors of the kinesin-14 family. Motors cross-link diverging MTs and rapidly align them. When microtubules are aligned, dimeric motors start to move along the MT track keeping the opposite MT as a cargo. Dimeric motors work cooperatevely; depending on the orientation of MT rods, they either cluster two parallel MTs or push apart the anti-parallel ones, providing MT sliding.

Being multivalent motor, kinesin-14 can associate with one MT by the tail domains and move along the other one utilising the energy of ATP by the catalytic heads [21]. Kinesin-14 proteins operate in teams since the group of such motors can move continuously. Motor domains can release the microtubule,

but motor remains bound to the MT at cargo-binding sites.

Thus, two MTs can be mutually reoriented and translocated by the group of kinesin-14 proteins, in particular, they can align diverging MT rods and produce MT sorting [20].

After the alignment, MTs can obtain either parallel or anti-parallel configuration. Anti-parallel MTs slide apart with their "+"-end pointing out; populations of motors situating on both MTs walk to the '−"-end and therefore forces applied by both populations to one MT are pointing the same direction. MTs in the parallel arrangement, in principle, can be locked by the two populations of kinesin-14 motors, since they can produce a "tug-of-war"; however, broken balance leads to polar clustering, during which "−"-ends of MTs are focused by motors (the term "focusing" means that eventual positions of "−"-ends coincide). The latter phenomenon is also known as "pole focusing", but term polar clustering will be used instead to emphasise, that after such interaction MTs obtain the same orientation and almost the same position (in case of equal MT lengths).

Kinesin-14 is just one of multivalent dimeric proteins. Another example of such proteins is the plus-directed kinesin-12 motor [22].

Tetrameric motor kinesin-5

Kinesin-5 motors are plus-directed tetrameric motors consisting of two homodimers that are arranged in an antiparallel manner so that pairs of heads project from each end, forming a multivalent motor [23, 24]. Kinesin-5 are relatively slow processive motors; they can walk 100 nm without disassociation. Processivity and the presence of two pairs of motor domains enable the individual motor of kinesin-5 family to rearrange MTs. Though, they can act cooperatively as well.

These kinesins can align diverging MTs as well. Depending on the configuration, kinesin-5 tetramers lock parallel microtubules and slide apart antiparallel ones [24]. At least the latter mechanism participates in the centrosome/spindle pole separation and spindle bipolarity organisation [25].

Sliding of anti-parallel MTs occurs in the direction opposite to one generated by kinesin-14 family motors, which is consistent with the antagonistic behaviour of these kinesins during spindle formation [18, 19].

In case of parallel MTs kinesin-5 motors walk toward the "+"-ends of both MTs. Stepping of the group of motors has a stochastic nature and generates alternating back and forth total forces [26]. If filaments are of different length, it can lead to the oscillatory motion of shorter rod along the longer one. If MT rods have equal length, one can assume that entropic forces should eventually cluster parallel MTs tending to increase the overlapping length, in the manner known for the passive cross-linkers [27]. So far experimental works

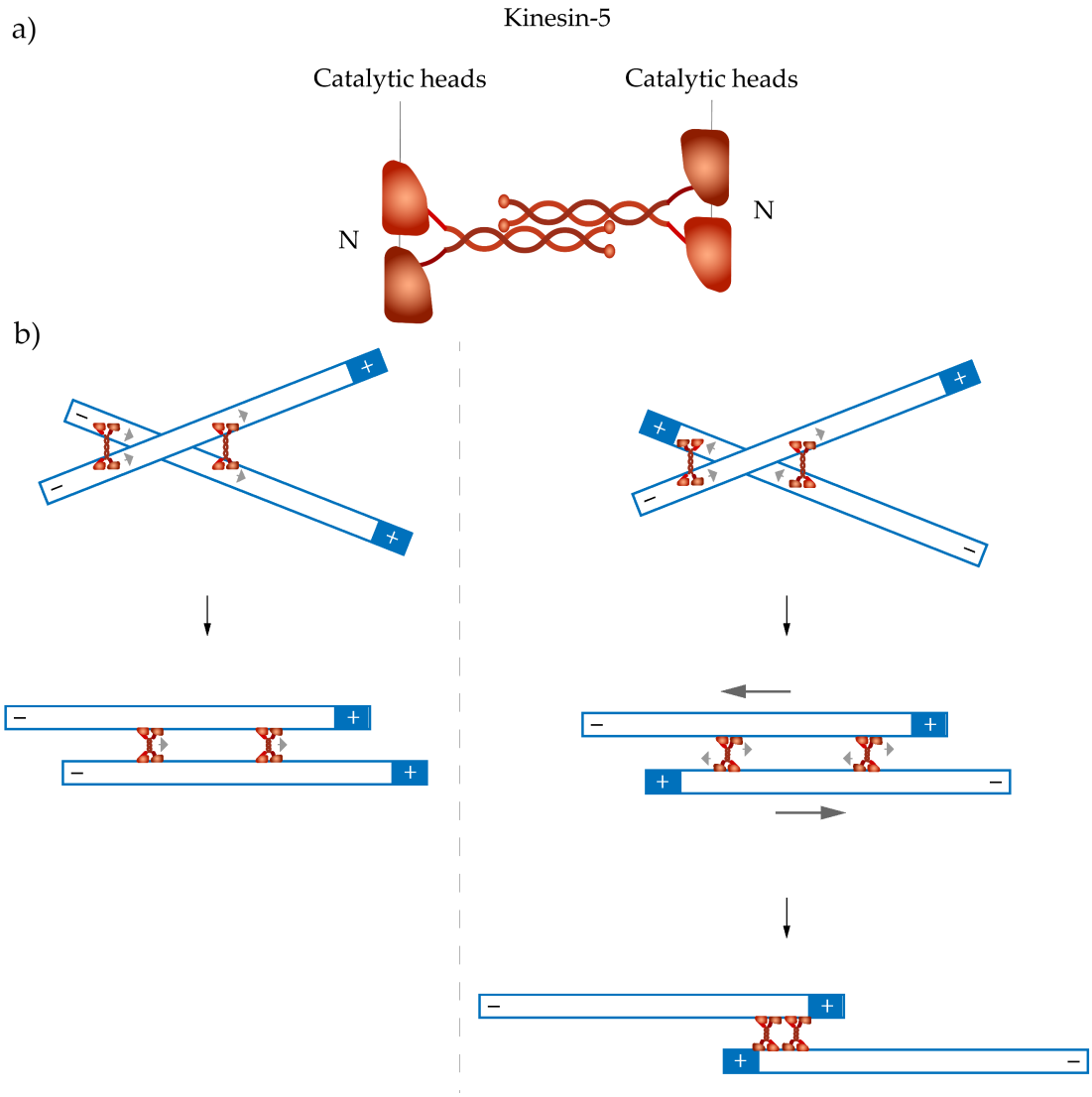

Figure 1.5: A) schematic structure of kinesin-5. Kinesin-5 is the plus-directed tetrameric multivalent motor. Because kinesin-5 motor has two catalytic heads at each side (4 all together), it can walk along two microtubules simultaneously toward their "+"-ends; b) action of the kinesin-5 family member. Plus directed motors crosslink MTs and push apart antiparallel ones.

revealed no clear evidence of directional motion of parallel MTs. However, it was demonstrated that the group of kinesin-5 motors generate brake-like resistance against relative filament sliding [26].

1.2.3 Generalisation of the motor-induced interaction

To sum up, both plus- and minus-directed molecular motors being dimeric or tetrameric proteins can align MT filaments. After the alignment arrangement of MTs can be either parallel or antiparallel. The parallel MTs are clustered, while antiparallel ones are pushed apart by motors [28]. For definiteness we consider plus-directed motors in this work. The first interaction type is referred to as *polar clustering* (or just *clustering* for brevity), while the latter one is

called *antiparallel sliding* (or just *sliding*). Two discussed basic interactions are depicted in Fig. 1.6.

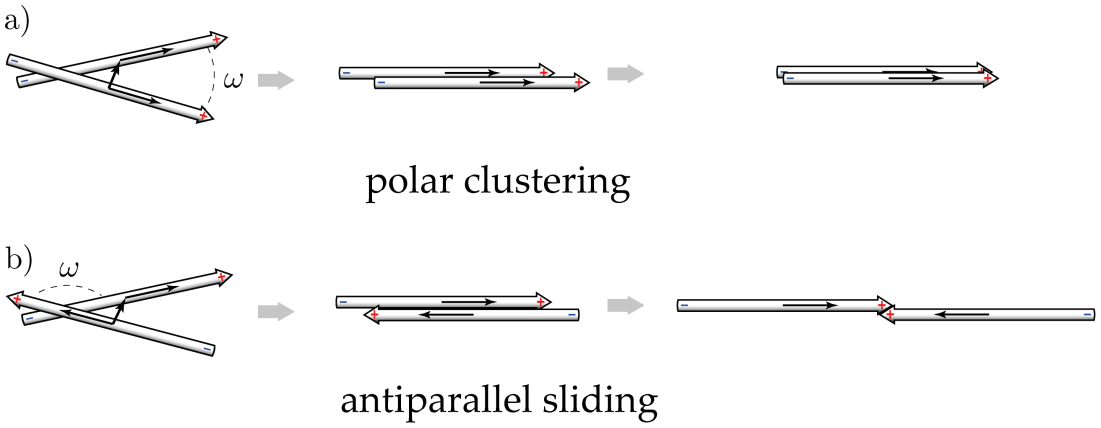

Figure 1.6: Generalised rule of the motor-induced interaction between microtubules. a) polar clustering of MTs, b) antiparallel sliding of MTs (in case of plus-directed motors).

One can assume that the type of interaction depends on the initial angle between the intersecting MTs. So polar clustering occurs when ω is smaller than some critical value ω_{cr} (Fig. 1.6), while antiparallel sliding happens when $\omega > \omega_{cr}$. Critical value ω_{cr} can vary for different motors.

For some reason, the two discussed interactions are not equivalent for some motors. For example, kinesin-12 motors "prefer" the clustering of the parallel MTs [22], while MT sliding is preferable option for the kinesin-5 motors [23, 24, 29]. However, the mechanism of such an imbalance is poorly understood. The probability of each outcome can also vary but this fact is disregarded in the current work.

Therefore different motors can be classified according to the type of interaction they prefer: we will use the term *clustering* or *sliding* motors, depending on the preferred interaction. If motors are able to provide both interactions and have no preference, we will refer to them as *sliding/clustering* motors.

In terms of the generalised motor-induced interaction rule, formulated in Fig. 1.6, small ω_{cr} is related to clustering motors, large ω_{cr} corresponds to sliding motors, for the sliding/clustering motors $\omega \approx \pi/2$.

We discuss clustering motors in Chapter 2 and sliding/clustering motors in Chapter 3 of this thesis.

1.2.4 Distribution of motors along the MTs

MMs can associate, disassociate, and move along the MT filament. With these assumptions, the motor distribution along individual microtubules can reach an equilibrium profile. Such equilibrium motor distribution was investigated experimentally [30, 31]. For plus-directed motors, it was shown that the motor

density stays low and approximately constant in the vicinity of the minus-end of the microtubules until it rises sharply and saturates at another constant value close to the plus-end. This behaviour is corroborated by 1D non-equilibrium models [30–33] that relate this distribution to the formation of traffic jams at the plus-end, or to the dependence of motor speed on their concentration.

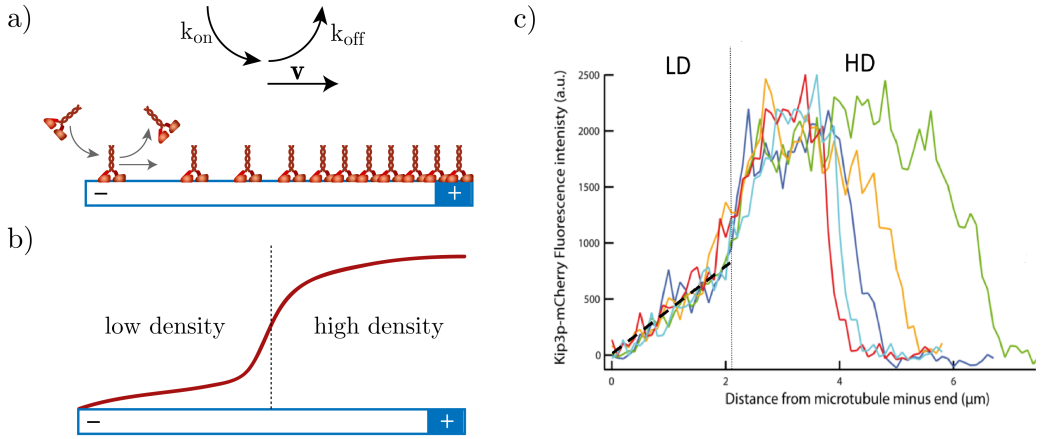

Figure 1.7: Distribution of motors along the individual MT a) cartoon depicting inhomogeneous distribution plus-directed motors along the individual MT. b) cartoon of the coarse-grained distribution, c) experimentally measured distribution of kinesin motors along the MT taken from [31], notations LD and HD denote low and high density of motors.

1.3 MT Patterns

1.3.1 *In vivo* MT patterns

In vivo microtubules can form a number of characteristic intracellular structures [34] that are associated with distinct functions.

In non-dividing cells, e.g. in fibroblasts (Fig. 1.8 a i) , microtubules are usually nucleated from a centrosome, forming a radial array or aster. All *in vivo* asters have "+"-ends growing outwards. In dividing animal cells, two centrosome-nucleated asters combine with an antiparallel overlap zone to build a mitotic spindle – apparatus crucial for cell division and responsible for the chromosome segregation (Fig. 1.8 a ii). Female meiotic spindles [35] and plant spindles [36] possess no centrosomes (Fig. 1.8 a ii-iii). In this case, molecular motors play an important role sorting microtubule ends and forming the antiparallel overlap of "+"- ends in the midzone, and two focused poles of "−"- ends on each side.

Finally, antiparallel bundles of MTs can be found in proximity of the cortex of plant cells (Fig. 1.8 a iv), where they control unidirectional cell growth. In the dendrites of neurons (Fig. 1.8 a v), antiparallel MTs organise bidirectional transport of vesicles, while in the axons parallel MT bundles provide long-distance transport [37].

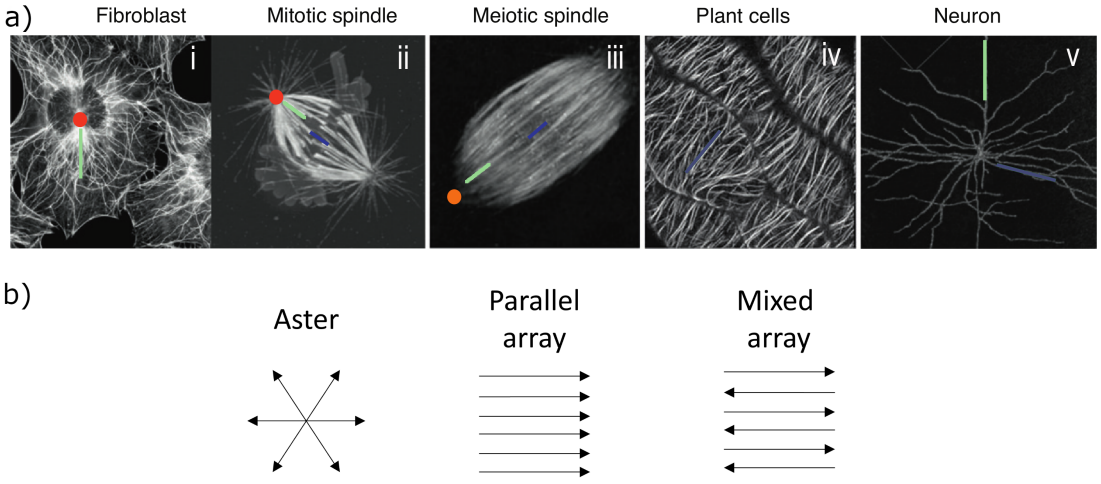

Figure 1.8: A) *In vivo* MT structures. Left to right: i) fibroblast, ii) mitotic spindle, iii) meiotic spindle, iv) plant cell, v) neuron. Red circles illustrates centrosome organised asters, orange circles are for self-organised asters, green and blue segments depict areas with parallel and antiparallel MT arrays. Picture is taken from [34]. b) classes of MT structures: aster, parallel array, and anti-parallel array (array with mixed orientation of MTs). Arrows depict polarity of the MTs.

All patterns mentioned above may be roughly divided into three types : asters, parallel arrays, and anti-parallel arrays (Fig. 1.8 b). Some *in vivo* micro-

tubular structures can contain all three pattern classes, e.g. the mitotic spindle. The details of the spindle assembly and architecture vary across species and cell types, however, some common features can be identified: i) in the centre of the spindle (midzone) MTs are bundled by motors and cross-linkers and form antiparallel overlap of "+"-ends; ii) at the pointed ends (spindle poles) microtubules "−"-ends are focused. It is known, that various motors participate in this complex pattern formation organising different spindle zones.

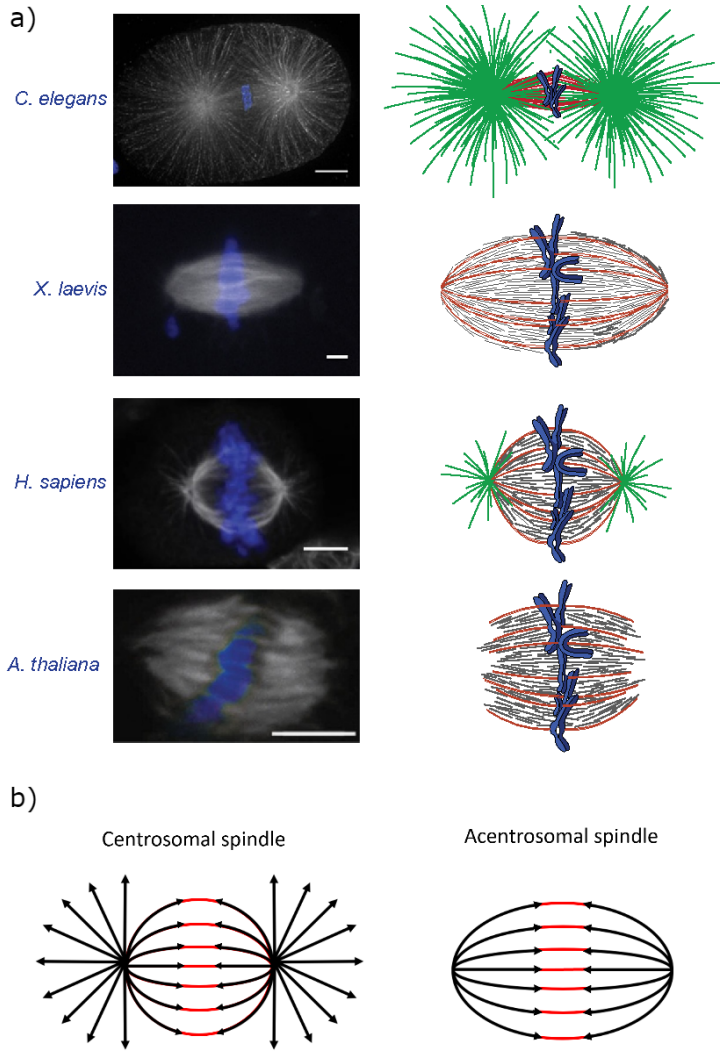

Figure 1.9: Spindle morphology. a) In the schematics, from top to bottom: *C. elegans* spindle , *X. laevis* meiotic spindle, the spindle in HeLa cells, plant spindle of *Arabidopsis thaliana*. Astral MTs are green, interpolar MTs are grey, k-fibers (MT structures connected to chromosomes) are brown. The illustration is taken from [38]. b) schematic representation of centrosomal and acentrosomal spindle. The "+"-ends of the microtubules project away from the spindle pole, while the "−"-ends are anchored at the spindle poles, which are organised by centrosomes or by MT-associated motors. On can recognise all three types of MT patterns: asters, parallel and anti-parallel arrays.

1.3.2 *In vitro* MT patterns

Self-organised formation of spindle-like structures has been reconstructed via *in vitro* experiments with cell extracts (Fig.1.10). Such cell-free assays reproduce the formation of asters growing out from artificial centrosomes; these asters can meet and organise antiparallel overlap zones [39, 40]. Objects similar to the meiotic spindle can self-assemble around the beads seeded in the *Xenopus laevis* egg extract [41, 42]. Self-organisation in such assays does not depend on any underlying cell cycle, but still the systems contain a huge number of components.

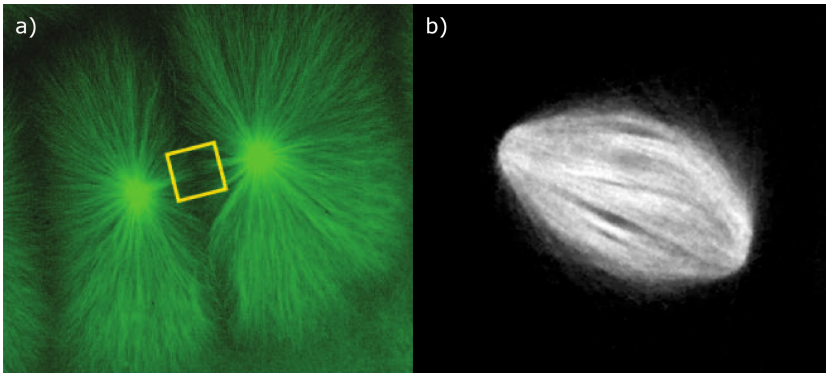

Figure 1.10: Reconstitution of the MT spatial organization in the cell-free system. a) formation of asters, b) spindle-like structure self-assembly in the *Xenopus laevis* egg extract.

However, the fundamental principles of the pattern formation in MTs can be investigated in the reconstituted system. This thesis is devoted to such systems, in particular, quasi 2-dimensional mixtures of stabilised microtubules, purified motors, and agents necessary for the activity of the motors, such as ATP.

These simplified experimental assays give us general insights into the functioning of the cytoskeleton. They recapitulate spontaneous transitions to various ordered states and formation of complex structures including asters, vortices, and spirals [28, 43, 44], or structures with anti-parallel MT arrangement [45, 46]. Note, that antiparallel arrangement of MTs is obtained in the presence of depletion agents, such as polyethylene glycol (PEG). Depletion agents (or depletants) are globular molecules playing several roles. They can facilitate the formation of the MT bundles, e.g. recently it was demonstrated that PEG yields apolar clustering of microtubules due to the entropic forces [47].

It is believed that different types of motors favour formation of distinct patterns (Fig.1.11): some motors provide the formation of network of coarsening asters [28], while microtubule-sliding motors organise MTs into anti-parallel bundles. Such extensile networks of MTs exhibit repeating cycles in which microtubular bundles self-extend, rotate, fracture and disappear in the back-

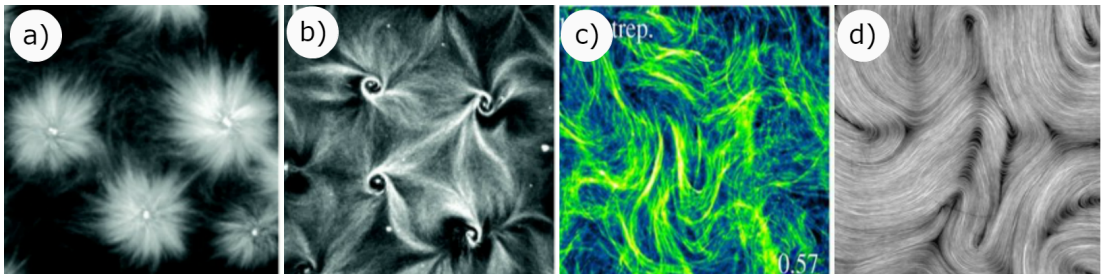

Figure 1.11: Examples of patterns observed in MT-MM mixtures: a-b) formation of asters, vortices and spirals [44]; c-d) formation of structures with mixed polarity [48, 49]. Plots a-b) correspond to the experiments with thick layer of MT-MM mixture, plot d) represents thin layer.

ground [48].

Note, that in some cases the spatial distribution of the MTs is homogeneous, while in other cases they form distinct clusters.

In the experimental systems with two motor types [28, 44] some additional structures can be observed, such as network of poles interconnected by bundles with and without antiparallel overlaps. Mixtures of MTs and MMs are also actively investigated in the assays with confined geometry (microfabricated rigid chambers [50] or lipid droplets [51, 52]) and at curved surfaces [53]. Finally, motility assay exhibit formation of various moving structures including vortices [54, 55], however, in this case, MTs are moved by the non-multivalent motors fixed on the substrate, and therefore always possess a velocity, while this work is devoted to pattern formation in non-self propelled MT biofilaments.

1.4 Active matter

A suspension of cytoskeletal filaments and molecular motors is a paradigmatic class of active matter.

Active matter is a type of matter consisting of large numbers of active participants, each of which can consume energy in order to move or to exert mechanical forces [56, 57]. In case of MT cytoskeleton or MT-MM mixtures local input of energy is provided by the MMs, which convert chemical energy stored in ATP to move MTs in respect to each other.

The study of active matter has seen a dramatic surge of interest over the last few years. Nowadays this topic covers collective behaviour of microscopic and macroscopic objects of biological and artificial nature. The former include motor driven cytoskeletal filaments [44, 45, 58], self-propelled microorganisms [59], migrating cells [60], active colloids and synthetic self-propelled particles [61]; the latter involve groups of animals [62], such as schooling fishes [63] or flocking birds [64], and so on [65].

Spontaneous transitions to the ordered state, pattern formation, activity-induced phase separation are phenomena which are intensively investigated within the framework of active matter. Theory has strived to identify scaling laws and universality classes within which to catalogue the physics of active materials [56, 66]. However, the inherent nonequilibrium nature of the active matter renders this programme much more challenging than in passive systems.

1.5 Classification of active matter models

In this Section, we provide a simplified classification of active matter systems and models used for its description. Along the way, we will determine the place of our theory within this classification.

Current active matter models can be categorised according to the breaking symmetries (or inherent order parameters), the overdamping level, compressibility, motility of the particles, level of coarse-graining and method of derivation.

1.5.1 Order parameters and interaction symmetries

An order parameter is a measure of the degree of order. Since spherical particles are outside the scope of this thesis, let us focus on ordered states associated with elongated objects. Natural order parameters for such objects are: i) a polar order parameter (polarity, orientation) which can be described by a vector of the mean orientation of particles p_i, ii) a nematic order parameter (or nematic alignment tensor) which describes the alignment of objects disregarding their orientation [56]. Usually the tensor Q_{ij} from the Landau - de Gennes theory is used to describe the nematic order.

If we associate a unit vector n_i with each elongated polar particle, vector p_i will describe average $\langle n_i \rangle$ in some physical volume (or surface element), while the nematic alignment the tensor Q_{ij} will correspond to $\langle n_i n_j - \delta_{ij} n_k n_k / 2 \rangle$.

Note, that the Q-tensor is invariant under the reflection ($\mathbf{n} \to -\mathbf{n}$). It is also traceless and symmetric: $Q_{yy} = -Q_{xx}$ and $Q_{yx} = Q_{xy}$, thus Q-tensor has only two independent components.

Elongated particles can be polar or apolar depending on whether their ends are distinguishable or not (apolar particles are head-tail symmetric). Polar order arises when polar particles are oriented along the same direction on average. If long axes of particles are roughly parallel, system has nematic order. It can arise with aligned apolar particles or with parallel polar particles pointing into opposite directions (Fig. 1.12).

Besides the symmetry of particles themselves, the type of interaction be-

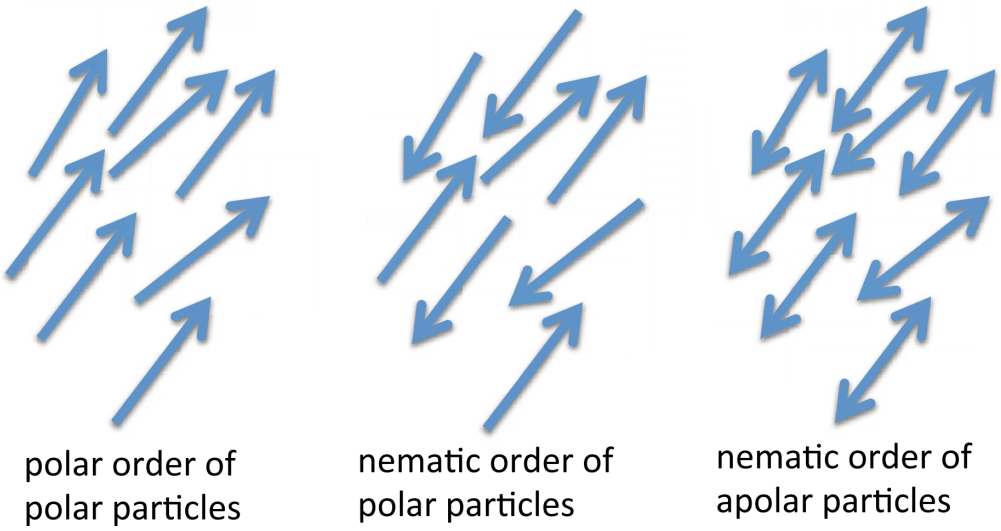

Figure 1.12: Polar particles can exhibit the polar order (left) or nematic order (centre). Apolar active particles are head-tail symmetric and can exhibit the nematic order (right). Cartoon is taken from [56]

tween active units can lead to an ordered state. For example, self-propelled (polar) agents can order in a nematic state if they undergo nematic interactions [67].

As it was discussed above, because the MT biopolymers have intrinsic anisotropy, if they interact via the directed molecular motors their polarity can be distinguished. On the other hand steric interactions or MTs are generally apolar. Usually, active matter models consider a single order parameter, either polar or nematic one; while the coexisting polar and nematic states in MT patterns imply the presence of both parameters in a model (the term "mixed symmetry" is used to describe such models [56]).

1.5.2 "Wet/dry" models and compressibility

In respect to momentum conservation, active matter models can be roughly divided into two groups: "dry" [65, 68] and "wet" [69, 70].

Active particles are usually surrounded by viscous fluid. If it can be treated as an inert medium providing friction only, we can neglect it and consider overdamped dynamics of particles separately. In such "dry" systems momentum conservation is not necessary [33].

If particle movement is able to cause significant fluid flow or if fluid affects particle movement, hydrodynamics must be included into the model. The dynamics in such "wet" models is such that and momentum is conserved. For example, fluid with particles can be treated as one material; the simplest approximation is an incompressible viscoelastic fluid [69]. This approach is intensively used for the bacterial swimmers investigation. Models with more

sophisticated rheology of the suspension of active particles are used in active gels.

However the "dry/wet" classification concerns theoretical frameworks of choice rather than systems themselves. The choice between dry and wet models should be based on particular system properties such as the fluid viscosity and particle drag coefficient, particles density and so on.

One more property defining the model is the system compressibility. As it was mentioned, microscopic active agents are usually surrounded by fluid. The system "agents plus fluid" is almost incompressible, but the concentration of agents can vary in space. Thus, the concentration of active particles (or number density ρ) can be inhomogeneous, and therefore we can treat it as compressible.

The vast majority of active biofilaments models describes such systems as momentum-conserving ("wet") incompressible "active gels" [70–72] with near-uniform filament density. In contrast, the models we develop in this thesis are both compressible and "dry" (i.e., non-momentum conserving). Compressibility is an essential step towards a more realistic description of both biological and synthetic systems, as MT density varies substantially both in the spindle and in the hierarchical active matter assembled *in vitro* [45, 46]. Additionally, within the intracellular milieu, hydrodynamic flows are typically quenched and relatively unimportant in the cell, so the dry limit is the most relevant one.

1.5.3 Self-propulsion

Some models involve self-propulsion of particles [64, 68, 73–76]. It means that particles have their own (typically constant) velocity. The most explored example of the theory with self-propulsion of particles is the Vicseck model [73]. Such models are applicable for motility assays [54, 58] but cannot be extended directly to the case of simple MT-MM mixtures, where filaments can only change position and orientation due to either thermal diffusion, motor-mediated or steric interactions.

1.5.4 Level of the coarse-graining and method of derivation

Theoretical models of the active matter can be roughly divided into three classes based on the coarse-graining level: microscopic, mesoscopic, and macroscopic approaches.

Microscopic approaches are based on direct agent-based simulations and do not usually provide any analytical description.

Mesoscopic and macroscopic models do not consider discrete particles, but instead operate with evolution equations of coarse-grained field variables, such

as order parameters or density, and differ in the way they are derived. Mesoscopic theories are built on coarse-graining of some microscopic model, while macroscopic (or hydrodynamic) ones initially consider the system at a higher level. They are mostly phenomenological and are often based on general symmetry arguments. Both classes can be referred to as mean-field theories. They allow one to obtain similar continuous equations for a set of slow variables as a final result.

We here are not concerned with microscopic investigation of the MT cytoskeleton [44, 77] and focus on the continuous models.

While the continuous description of overdamped active MT biofilaments can be obtained on symmetry grounds [78–80], it can be also derived by rigorously coarse-graining a specific underlying microscopic model [33, 81–85]. This approach is very useful as it allows us to determine the effective parameters of the continuum theory in terms of geometrical and physical quantities appearing in the microscopic model. In this thesis, we follow this approach to describe a suspension of MTs interacting via molecular motors.

Mesoscopic theories describing active MTs take into account properties of MT-motor interactions, i. e. they are based on some interaction model or interaction rules. Usually, they provide hydrodynamic equations by coarse-graining of the equation for the probability distribution function (PDF). This equation can be written in different manners: Boltzmann kinetic method usually assumes the instantaneous interactions and immediate changes in the PDF [33, 82, 84], while the Smoluchowski approach incorporates the probability fluxes (and involves so-called Doi equation) [83, 86, 87]. As a result, both approaches predict the macroscopic behaviour of the system starting from the microscopic details of the interaction between MTs and provide similar results, the discrepancies between the continuous models obtained in both frameworks are discussed in [88].

The Smoluchowski approach was used by the group of Kruse *et al* and Marchetti *et al* [83, 85–87]. In these works MMs exchange forces and torques among the pairs of MTs, therefore yielding active contributions to the rotational and translational velocities of biofilaments. Note that such models involve at least three parameters describing mutual velocities of MTs during the interaction. However, it is difficult to measure these three parameters experimentally. It is also worth to mention, that in [83, 86] it was argued that directed motion of molecular motors along the microtubules can create a flow in the surrounding fluid that would result in microtubule self-propulsion, and, hence, the position of the centre of mass of two bundles can change during an interaction event.

In the kinetic approach employed by Aranson and Tsimring [33, 82, 89], pairwise motor-mediated interactions of microtubules were treated as instan-

taneous collisions. These authors considered plus-directed clustering motors, which can align and bundle microtubules. Hydrodynamic equations for the two field variables, filament concentration and orientation, were derived by coarse-graining of the corresponding Boltzmann-type equation for the PDF. Their model successfully recapitulated such phenomena as spontaneous ordering, bundling and formation of asters and vortices. Under this model, the interaction retains the position of the centre of mass of the pair of MTs, and hence no self-propulsion is involved, which is more realistic.

1.5.5 Our model

All the described approaches should be used for a comprehensive description of the phenomena that occur in the MT cytoskeleton. Since microscopic models just reproduce the existing phenomena and usually do not provide the explanation of underlying physics, we will focus on the continuous models.

The major aim of this work is to connect the specific microscopic interaction of MTs to the large scale patterns, therefore we refuse the general hydrodynamic approaches and concentrate on the mesoscopic models, since they can be based on biologically relevant rules of interaction.

We observe that models derived using the Smoluchowski approach implicitly include self-propulsion, and therefore decide to follow the Boltzmann kinetic method.

Thus, in this thesis, we develop mesoscopic dry kinetic theory involving mixed symmetry and describing the pattern formation in reduced *in vitro* assays containing the mixture of non-self-propelling MTs and MMs.

In the first part of the thesis, we revisit the technique proposed by Aranson and Tsimring and test our theory considering polar clustering of MTs by MMs. In the second part of this thesis, we use our theory to investigate the pattern formation in the case of sliding/clustering interaction between MTs.

The biological realism of the considered collision rules can be experimentally motivated. For example, recent experimental data and agent-based simulations [28, 90] emphasise that the generalised interaction rules we introduce in Subsection 1.2.3 are crucial for the formation of nematic and polar structures in MT cytoskeleton. The work of Roostalu and co-workers [90] points out the role of anisotropy of motor distribution along the individual MT.

References

[1] A. Desai and T. J. Mitchison, "Microtubule Polymerization Dynamics," *Annu. Rev. Cell Dev. Biol.*, vol. 13, no. 1, pp. 83–117, 1997.

[2] R. C. Weisenberg, G. G. Broisy, and E. W. Taylor, "Colchicine-binding protein of

mammalian brain and its relation to microtubules," *Biochemistry*, vol. 7, no. 12, pp. 4466–4479, 1968.

[3] R. G. Burns, "Alpha-, beta-, and gama-tubulins: Sequence comparisons and structural constraints," *Cell Motil. Cytoskeleton*, vol. 20, no. 3, pp. 181–189, 1991.

[4] M. C. Ledbetter and K. R. Porter, "A" microtubule" in plant cell fine structure," *J. Cell Biol.*, vol. 19, no. 1, pp. 239–250, 1963.

[5] L. A. Amos and A. Klug, "Arrangement of subunits in flagellar microtubules," *J. Cell Sci.*, vol. 14, no. 3, pp. 523–549, 1974.

[6] A. S. Infante, M. S. Stein, Y. Zhai, G. G. Borisy, and G. G. Gundersen, "Detyrosinated (Glu) microtubules are stabilized by an ATP-sensitive plus-end cap," *J. Cell Sci.*, vol. 113, no. 22, pp. 3907–3919, 2000.

[7] A. Ganguly, H. Yang, and F. Cabral, "Paclitaxel-dependent cell lines reveal a novel drug activity," *Mol. Cancer Ther.*, vol. 9, no. 11, pp. 2914–2923, 2010.

[8] R. D. Vale, T. S. Reese, and M. P. Sheetz, "Identification of a novel force-generating protein, kinesin, involved in microtubule-based motility," *Cell*, vol. 42, no. 1, pp. 39–50, 1985.

[9] C. J. Lawrence, R. K. Dawe, K. R. Christie, *et al.*, "A standardized kinesin nomenclature," *J. Cell Biol.*, vol. 167, no. 1, pp. 19–22, 2004.

[10] K. Svoboda and S. M. Block, "Force and velocity measured for single kinesin molecules," *Cell*, vol. 77, no. 5, pp. 773–784, 1994.

[11] S. M. Block, C. L. Asbury, J. W. Shaevitz, and M. J. Lang, "Probing the kinesin reaction cycle with a 2D optical force clamp.," *Proc. Natl. Acad. Sci. U. S. A.*, vol. 100, no. 5, pp. 2351–2356, 2003.

[12] A. Gennerich, A. P. Carter, S. L. Reck-Peterson, and R. D. Vale, "Force-Induced Bidirectional Stepping of Cytoplasmic Dynein," *Cell*, vol. 131, no. 5, pp. 952–965, 2007.

[13] C. Veigel and C. F. Schmidt, "Moving into the cell: single-molecule studies of molecular motors in complex environments," *Nat. Rev. Mol. Cell Biol.*, vol. 12, no. 3, pp. 163–176, 2011.

[14] G. Woehlke and M. Schliwa, "Walking on Two Heads: the Many Talents of Kinesin," *Nat. Rev. Mol. Cell Biol.*, vol. 1, no. 1, pp. 50–58, 2000.

[15] R. A. Cross and A. McAinsh, "Prime movers: the mechanochemistry of mitotic kinesins," *Nat. Rev. Mol. Cell Biol.*, vol. 15, no. 4, pp. 257–271, 2014.

[16] K. Visscher, M. J. Schnitzer, and S. M. Block, "Single kinesin molecules studied with a molecular force clamp.," *Nature*, vol. 400, no. 6740, pp. 184–189, 1999.

[17] M. E. Tanenbaum, R. D. Vale, and R. J. McKenney, "Cytoplasmic dynein crosslinks and slides anti-parallel microtubules using its two motor domains," *Elife*, vol. 2, 2013.

[18] K. S. Burbank, T. J. Mitchison, and D. S. Fisher, "Slide-and-Cluster Models for Spindle Assembly," *Curr. Biol.*, vol. 17, no. 16, pp. 1373–1383, 2007.

[19] I. Brust-Mascher and J. M. Scholey, "Microtubule Flux and Sliding in Mitotic Spindles of Drosophila Embryos," *Mol. Biol. Cell*, vol. 13, pp. 3967–3975, 2002.

[20] G. Fink, L. Hajdo, K. J. Skowronek, *et al.*, "The mitotic kinesin-14 Ncd drives directional microtubule–microtubule sliding," *Nat. Cell Biol.*, vol. 11, no. 6, pp. 717–723, 2009.

[21] Z.-Y. She and W.-X. Yang, "Molecular mechanisms of kinesin-14 motors in spindle assembly and chromosome segregation," *J. Cell Sci.*, vol. 130, no. 13, pp. 2097–2110, 2017.

[22] H. Drechsler and A. D. McAinsh, "Kinesin-12 motors cooperate to suppress microtubule catastrophes and drive the formation of parallel microtubule bundles," *Proc. Natl. Acad. Sci.*, p. 201516370, 2016.

[23] L. C. Kapitein, E. J. Peterman, B. H. Kwok, *et al.*, "The bipolar mitotic kinesin eg5 moves on both microtubules that it crosslinks," *Nature*, vol. 435, no. 7038, p. 114, 2005.

[24] L. C. Kapitein, B. H. Kwok, J. S. Weinger, *et al.*, "Microtubule cross-linking triggers the directional motility of kinesin-5," *J. Cell Biol.*, vol. 182, no. 3, pp. 421–428, 2008.

[25] N. P. Ferenz, A. Gable, and P. Wadsworth, "Mitotic functions of kinesin-5," *Semin. Cell Dev. Biol.*, vol. 21, pp. 255–259, 2010.

[26] Y. Shimamoto, S. Forth, and T. M. Kapoor, "Measuring pushing and braking forces generated by ensembles of kinesin-5 crosslinking two microtubules," *Dev. Cell*, vol. 34, no. 6, pp. 669–681, 2015.

[27] Z. Lansky, M. Braun, A. Lüdecke, *et al.*, "Diffusible crosslinkers generate directed forces in microtubule networks," *Cell*, vol. 160, no. 6, pp. 1159–1168, 2015.

[28] C. Hentrich and T. Surrey, "Microtubule organization by the antagonistic mitotic motors kinesin-5 and kinesin-14," *J. Cell Biol.*, vol. 189, no. 3, pp. 465–480, 2010.

[29] S. M. J. L. van den Wildenberg, L. Tao, L. C. Kapitein, *et al.*, "The homotetrameric kinesin-5 KLP61F preferentially crosslinks microtubules into antiparallel orientations," *Curr. Biol.*, vol. 18, no. 23, pp. 1860–1864, 2008.

[30] K. Nishinari, Y. Okada, A. Schadschneider, and D. Chowdhury, "Intracellular transport of single-headed molecular motors KIF1A," *Phys. Rev. Lett.*, vol. 95, no. 11, p. 118101, 2005.

[31] C. Leduc, K. Padberg-Gehle, V. Varga, *et al.*, "Molecular crowding creates traffic jams of kinesin motors on microtubules," *Proc. Natl. Acad. Sci.*, vol. 109, pp. 6100–6105, 2012.

[32] A. Parmeggiani, T. Franosch, and E. Frey, "Phase Coexistence in Driven One-Dimensional Transport," *Phys. Rev. Lett.*, vol. 90, p. 086601, 2003.

[33] I. S. Aranson and L. S. Tsimring, "Theory of self-assembly of microtubules and motors," *Phys. Rev. E*, vol. 74, p. 31915, 2006.

[34] M. Dogterom and T. Surrey, "Microtubule organization in vitro," *Curr. Opin. Cell Biol.*, vol. 25, pp. 1–7, 2013.

[35] R. Heald, R. Tournebize, T. Blank, *et al.*, "Self-organization of microtubules into bipolar spindles around artificial chromosomes in Xenopus egg extracts," *Nature*, vol. 382, no. 6590, p. 420, 1996.

[36] J. C. Ambrose, W. Li, A. Marcus, H. Ma, and R. Cyr, "A minus-end–directed kinesin with plus-end tracking protein activity is involved in spindle morphogenesis," *Mol. Biol. Cell*, vol. 16, no. 4, pp. 1584–1592, 2005.

[37] R. P. Tas and L. C. Kapitein, "Exploring cytoskeletal diversity in neurons," *Science (80-.).*, vol. 361, no. 6399, pp. 231–232, 2018.

[38] K. J. Helmke, R. Heald, and J. D. Wilbur, *Interplay between spindle architecture and function*, vol. 306. Elsevier Inc., 1 ed., 2013.

[39] P. A. Nguyen, A. C. Groen, M. Loose, *et al.*, "Spatial organization of cytokinesis signaling reconstituted in a cell-free system," *Science (80-.).*, vol. 346, pp. 244–247, 2014.

[40] K. Ishihara, P. A. Nguyen, A. C. Groen, C. M. Field, and T. J. Mitchison, "Microtubule nucleation remote from centrosomes may explain how asters span large cells," *Proc. Natl. Acad. Sci.*, vol. 111, pp. 17715–17722, 2014.

[41] J. Brugués and D. Needleman, "Physical basis of spindle self-organization.," *Proc. Natl. Acad. Sci. U. S. A.*, vol. 111, pp. 18496–500, 2014.

[42] J. Brugués, V. Nuzzo, E. Mazur, and D. J. Needleman, "Nucleation and transport organize microtubules in metaphase spindles," *Cell*, vol. 149, pp. 554–564, 2012.

[43] F. J. Nédélec, T. Surrey, a. C. Maggs, and S. Leibler, "Self-organization of microtubules and motors.," *Nature*, vol. 389, no. September, pp. 305–308, 1997.

[44] T. Surrey, "Physical Properties Determining Self-Organization of Motors and Microtubules," *Science (80-.).*, vol. 292, no. 5519, pp. 1167–1171, 2001.

[45] T. Sanchez, D. Welch, D. Nicastro, and Z. Dogic, "Cilia-Like Beating of Active Microtubule Bundles," *Science (80-.).*, vol. 333, pp. 456–459, 2011.

[46] T. Sanchez, D. T. N. Chen, S. J. Decamp, M. Heymann, and Z. Dogic, "Spontaneous motion in hierarchically assembled active matter," *Nature*, vol. 491, no. 11591, pp. 1–5, 2012.

[47] F. Hilitski, A. R. Ward, L. Cajamarca, *et al.*, "Measuring cohesion between macromolecular filaments one pair at a time: Depletion-induced microtubule bundling," *Phys. Rev. Lett.*, vol. 114, no. 13, pp. 1–6, 2015.

[48] G. Henkin, S. J. DeCamp, D. T. N. Chen, T. Sanchez, and Z. Dogic, "Tunable dynamics of microtubule-based active isotropic gels," *Phil. Trans. R. Soc. A*, vol. 372, no. 2029, p. 20140142, 2014.

[49] S. J. DeCamp, G. S. Redner, A. Baskaran, M. F. Hagan, and Z. Dogic, "Orientational order of motile defects in active nematics," *Nat. Mater.*, vol. 14, pp. 1110–1115, 2015.

[50] L. Laan, N. Pavin, J. Husson, *et al.*, "Cortical dynein controls microtubule dynamics to generate pulling forces that position microtubule asters," *Cell*, vol. 148, no. 3, pp. 502–514, 2012.

[51] H. Baumann and T. Surrey, "Motor-mediated cortical versus astral microtubule organization in lipid-monolayered droplets," *J. Biol. Chem.*, vol. 289, no. 32, pp. 22524–22535, 2014.

[52] H. Baumann and T. Surrey, *Self-organization of motors and microtubules in lipid-monolayered droplets*, vol. 128. Elsevier Ltd, 2015.

[53] F. C. Keber, E. Loiseau, T. Sanchez, *et al.*, "Topology and dynamics of active nematic vesicles," *Science (80-.).*, vol. 345, no. 6201, pp. 1135–1139, 2014.

[54] Y. Sumino, K. H. Nagai, Y. Shitaka, *et al.*, "Large-scale vortex lattice emerging from collectively moving microtubules," *Nature*, vol. 483, no. 7390, p. 448, 2012.

[55] D. Inoue, B. Mahmot, A. M. R. Kabir, *et al.*, "Depletion force induced collective motion of microtubules driven by kinesin," *Nanoscale*, vol. 7, no. 43, pp. 18054–18061, 2015.

[56] M. C. Marchetti, J.-F. Joanny, S. Ramaswamy, *et al.*, "Hydrodynamics of soft active matter," *Rev. Mod. Phys.*, vol. 85, no. 3, p. 1143, 2013.

[57] S. Ramaswamy, "The Mechanics and Statistics of Active Matter," *Annu. Rev. Condens. Matter Phys.*, vol. 1, pp. 323–345, 2010.

[58] L. Huber, R. Suzuki, T. Krüger, E. Frey, and A. Bausch, "Emergence of coexisting ordered states in active matter systems," *Science*, p. eaao5434, 2018.

[59] C. Dombrowski, L. Cisneros, S. Chatkaew, R. E. Goldstein, and J. O. Kessler, "Self-concentration and large-scale coherence in bacterial dynamics," *Phys. Rev. Lett.*, vol. 93, no. 9, p. 98103, 2004.

[60] M. Poujade, E. Grasland-Mongrain, A. Hertzog, *et al.*, "Collective migration of an epithelial monolayer in response to a model wound," *Proc. Natl. Acad. Sci.*, vol. 104, no. 41, pp. 15988–15993, 2007.

[61] W. F. Paxton, K. C. Kistler, C. C. Olmeda, *et al.*, "Catalytic nanomotors: autonomous movement of striped nanorods," *J. Am. Chem. Soc*, vol. 126, no. 41, pp. 13424–13431, 2004.

[62] I. D. Couzin, C. C. Ioannou, G. Demirel, *et al.*, "Uninformed individuals promote democratic consensus in animal groups," *Science (80-.).*, vol. 334, no. 6062, pp. 1578–1580, 2011.

[63] J. Gautrais, C. Jost, M. Soria, *et al.*, "Analyzing fish movement as a persistent turning walker," *J. Math. Biol.*, vol. 58, no. 3, pp. 429–445, 2009.

[64] J. Toner and Y. Tu, "Long-range order in a two-dimensional dynamical XY model: How birds fly together," *Phys. Rev. Lett.*, vol. 75, no. 23, pp. 4326–4329, 1995.

[65] J. Toner and Y. Tu, "Flocks, herds, and schools: A quantitative theory of flocking," *Phys. Rev. E*, vol. 58, no. 4, p. 4828, 1998.

[66] D. Needleman and Z. Dogic, "Active matter at the interface between materials science and cell biology," *Nat. Rev. Matt.*, vol. 2, p. 17048, 2017.

[67] A. Baskaran and M. C. Marchetti, "Statistical mechanics and hydrodynamics of bacterial suspensions," *Proc. Natl. Acad. Sci.*, vol. 106, pp. 15567–15572, 2009.

[68] A. Peshkov, I. S. Aranson, E. Bertin, H. Chaté, and F. Ginelli, "Nonlinear field equations for aligning self-propelled rods," *Phys. Rev. Lett.*, vol. 109, no. 26, p. 268701, 2012.

[69] R. A. Simha, S. Ramaswamy, R. Aditi Simha, and S. Ramaswamy, "Hydrodynamic fluctuations and instabilities in ordered suspensions of self-propelled particles," *Phys. Rev. Lett.*, vol. 89, no. 5, p. 58101, 2002.

[70] K. Kruse, J. F. Joanny, F. Jülicher, J. Prost, and K. Sekimoto, "Generic theory of active polar gels: A paradigm for cytoskeletal dynamics," *Eur. Phys. J. E*, vol. 16, no. 1, pp. 5–16, 2005.

[71] K. Kruse, J. F. Joanny, F. Jülicher, J. Prost, and K. Sekimoto, "Asters, Vortices, and Rotating Spirals in Active Gels of Polar Filaments," *Phys. Rev. Lett.*, vol. 92, p. 078101, 2004.

[72] F. Jülicher, K. Kruse, J. Prost, and J. Joanny, "Active behavior of the Cytoskeleton," *Phys. Rep.*, vol. 449, pp. 3–28, 2007.

[73] T. Vicsek, A. Czirók, E. Ben-Jacob, I. Cohen, and O. Shochet, "Novel type of phase transition in a system of self-driven particles," *Phys. Rev. Lett.*, vol. 75, no. 6, p. 1226, 1995.

[74] J. Toner, Y. Tu, and S. Ramaswamy, "Hydrodynamics and phases of flocks," *Ann. Phys.*, vol. 318, no. 1, pp. 170–244, 2005.

[75] I. S. Aranson, A. Sokolov, J. O. Kessler, and R. E. Goldstein, "Model for dynamical coherence in thin films of self-propelled microorganisms," *Phys. Rev. E*, vol. 75, p. 40901, 2007.

[76] E. Bertin, M. Droz, and G. Grégoire, "Boltzmann and hydrodynamic description for self-propelled particles," *Phys. Rev. E*, vol. 74, pp. 1–4, 2006.

[77] R. Loughlin, R. Heald, and F. Nédélec, "A computational model predicts Xenopus meiotic spindle organization," *J. Cell Biol.*, vol. 191, pp. 1239–1249, 2010.

[78] H. Y. Lee and M. Kardar, "Macroscopic equations for pattern formation in mixtures of microtubules and molecular motors," *Phys. Rev. E*, vol. 64, no. 5, p. 056113, 2001.

[79] S. Sankararaman, G. I. Menon, and P. B. Sunil Kumar, "Self-organized pattern formation in motor-microtubule mixtures," *Phys. Rev. E*, vol. 70, p. 031905, 2004.

[80] E. Putzig, G. S. Redner, A. Baskaran, and A. Baskaran, "Instabilities, defects, and defect ordering in an overdamped active nematic," *Soft Matter*, vol. 12, no. 17, pp. 3854–3859, 2016.

[81] I. Maryshev, D. Marenduzzo, A. B. Goryachev, and A. Morozov, "Kinetic theory of pattern formation in mixtures of microtubules and molecular motors," *Phys. Rev. E*, vol. 97, p. 22412, 2018.

[82] I. S. Aranson and L. S. Tsimring, "Pattern formation of microtubules and motors: Inelastic interaction of polar rods," *Phys. Rev. E*, vol. 71, p. 050901, 2005.

[83] T. B. Liverpool and M. C. Marchetti, "Instabilities of Isotropic Solutions of Active Polar Filaments," *Phys. Rev. Lett.*, vol. 90, p. 138102, 2003.

[84] F. Ziebert and W. Zimmermann, "Nonlinear competition between asters and stripes in filament-motor systems," *Eur. Phys. J. E*, vol. 18, pp. 41–54, 2005.

[85] K. Kruse and F. Jülicher, "Actively Contracting Bundles of Polar Filaments," *Phys. Rev. Lett.*, vol. 85, pp. 1778–1781, 2000.

[86] T. B. Liverpool and M. C. Marchetti, "Bridging the microscopic and the hydrodynamic in active filament solutions," *EPL*, vol. 69, no. 5, p. 846, 2005.

[87] A. Ahmadi, M. C. Marchetti, and T. B. Liverpool, "Hydrodynamics of isotropic and liquid crystalline active polymer solutions," *Phys. Rev. E*, vol. 74, p. 061913, 2006.

[88] E. Bertin, A. Baskaran, H. Chaté, and M. C. Marchetti, "Comparison between Smoluchowski and Boltzmann approaches for self-propelled rods," *Phys. Rev. E*, vol. 92, p. 042141, 2015.

[89] F. Ziebert, I. S. Aranson, L. S. Tsimring, *et al.*, "Effects of cross-links on motor-mediated filament organization," *New J. Phys.*, vol. 9, p. 421, 2007.

[90] J. Roostalu, J. Rickman, C. Thomas, F. Nédélec, and T. Surrey, "Determinants of polar versus nematic organization in networks of dynamic microtubules and mitotic motors," *Cell*, vol. 175, no. 3, pp. 796–808, 2018.

Chapter 2

Polar clustering of microtubules

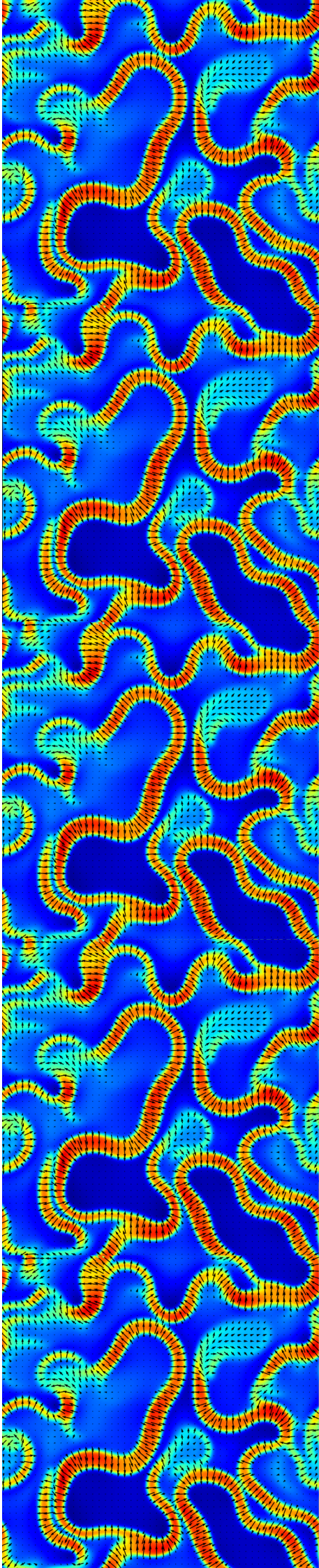

Abstract

In this chapter we formulate a theoretical approach, based on a Boltzmann-like kinetic equation, to describe pattern formation in two-dimensional mixtures of microtubular filaments and molecular motors. Following the previous work by Aranson and Tsimring [Phys. Rev. E **74**, 031915 (2006)] we model the motor-induced reorientation of microtubules as collision rules, and devise a semi-analytical method to calculate the corresponding interaction integrals. This procedure yields an infinite hierarchy of kinetic equations that we terminate by employing a well-established closure strategy, developed in the pattern-formation community and based on a power-counting argument. We thus arrive at a closed set of coupled equations for slowly varying local density and orientation of the microtubules, and study its behaviour by performing a linear stability analysis and direct numerical solutions. By comparing our method with the work of Aranson and Tsimring, we assess the validity of the assumptions required to derive their and our theories. We demonstrate that our approximation-free evaluation of the interaction integrals and our choice of a systematic closure strategy result in a rather different dynamical behaviour than was previously reported. Based on our theory, we discuss the ensuing phase diagram and the patterns observed.

2.1 Kinetic theory

The setup of our problem follows that of [1]. We consider a two-dimensional collection of microtubules, which we treat as slender rigid rods of length L, and the plus-directed clustering molecular motors.

Since microtubules are polar objects, we describe their local orientation by a vector $\mathbf{n}$ that points from the "$-$"- to the "$+$"-end of a microtubule. We introduce a Cartesian coordinate system (x, y), and parametrise the orientation vector by a single angle – i.e., $\mathbf{n} = (\cos\phi, \sin\phi)$.

Following [1] pairwise motor-mediated interactions of microtubules are treated as instantaneous collisions. Collision rule specific for clustering motors is depicted on Fig. 2.1: we assume that after a re-orientation event both MTs align along the bisector of the original angle between them, while their centre of mass does not move in the process.

We note that a motor simultaneously attached to both MTs applies a pair of equal and opposite forces to the system – i.e., it behaves as a force-dipole. Since the total force applied to the centre of mass is zero, its position is conserved. This assumption is in contrast with the work reported in [2–5].

To describe spatial and orientational inhomogeneities in the system, we introduce the probability distribution function $P(\mathbf{r}, \phi, t)$, defined in the usual way: $P(\mathbf{r}, \phi, t)d\mathbf{r}d\phi$ gives the number of microtubules in a small volume of the phase space $d\mathbf{r}d\phi$ which are at position $\mathbf{r}$ and possess an orientation given by ϕ at time t.

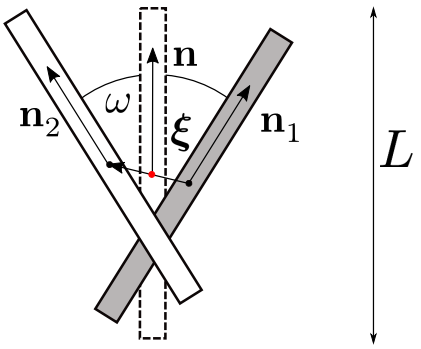

Figure 2.1: Collision rule employed in Eq. (2.3). Two colliding microbutules are re-oriented by the action of the molecular motors to assume a common orientation along the bisector of the original angle between them. Their centre of mass does not move in the process.

The Boltzmann-like kinetic equation

Following [1], the time-evolution of the probability distribution function is assumed to be governed by a Boltzmann-like kinetic equation:

$$\partial_t P(\mathbf{r},\phi) = D_r \partial_\phi^2 P(\mathbf{r},\phi) + \nabla_i D_{ij} \nabla_j P(\mathbf{r},\phi) + I_{int}(\mathbf{r},\phi). \tag{2.1}$$

The first two terms in Eq. (2.1) describe thermal rotational and translational diffusion of individual microtubules, while the last term is interaction integral representing motor-mediated interactions between microtubules. $\nabla_i = \partial/\partial x_i$, x_i are the Cartesian components of $\mathbf{r}$, and we use the Einstein summation convention; from now on we suppress the explicit time-dependence of P for brevity.

Interaction integral corresponding to the polar clustering rule has the following form:

$$\begin{aligned} I_{int}(\mathbf{r},\phi) = \int d\boldsymbol{\xi} \int_{-\pi}^{\pi} d\omega \Bigg[& W\left(\mathbf{r} - \frac{\boldsymbol{\xi}}{2}, \phi - \frac{\omega}{2}; \mathbf{r} + \frac{\boldsymbol{\xi}}{2}, \phi + \frac{\omega}{2}\right) \\ & \times P\left(\mathbf{r} - \frac{\boldsymbol{\xi}}{2}, \phi - \frac{\omega}{2}\right) P\left(\mathbf{r} + \frac{\boldsymbol{\xi}}{2}, \phi + \frac{\omega}{2}\right) \\ & - W(\mathbf{r},\phi;\mathbf{r}-\boldsymbol{\xi},\phi-\omega) P(\mathbf{r},\phi)\, P(\mathbf{r}-\boldsymbol{\xi},\phi-\omega) \Bigg], \end{aligned} \tag{2.2}$$

where $\boldsymbol{\xi}$ is a separation vector (the distance between centres of mass of two MTs) and ω is angle between MTs before the interaction (derivation of this expression can be found in Appendix A).

The first integral in Eq. (2.1) is a gain (source) term, which accounts for events where two microtubules (or microtubule bundles) with different positions and orientations are re-oriented by the motors to assume position and orientation $(\mathbf{r},\phi)$. The specific form of this term encodes our assumptions about the interaction rule, in this Chapter we assume that motors induce polar clustering; the details of such interactions are summarised in Fig. 2.1.

The second integral in Eq. (2.2) is a loss (sink) term, describing the process by which a bundle with the position and orientation $(\mathbf{r},\phi)$ leaves that configuration due to an interaction event with another bundle. The rate of both motor-induced processes is given by the function W discussed below.

Finally, it is important to underscore that the pair-wise nature of the interaction terms in Eq. (2.2) is *not* related to a dilute-limit assumption, as is often the case in Boltzmann-like kinetic theories, but rather stems from the fact that a multivalent molecular motor can only simultaneously attach to two microtubules [6, 7]. However, three-rod interactions are considered in Section 2.3 during the derivation of terms representing the excluded volume effect.

Thus, the eventual form of Kinetic Boltzmann-like equation reads:

$$\begin{aligned}\partial_t P(\mathbf{r},\phi) &= D_r\partial_\phi^2 P(\mathbf{r},\phi) + \nabla_i D_{ij}\nabla_j P(\mathbf{r},\phi)\\ &+ \int d\boldsymbol{\xi}\int_{-\pi}^{\pi} d\omega\Bigg[W\left(\mathbf{r}-\frac{\boldsymbol{\xi}}{2},\phi-\frac{\omega}{2};\mathbf{r}+\frac{\boldsymbol{\xi}}{2},\phi+\frac{\omega}{2}\right)\\ &\quad\times P\left(\mathbf{r}-\frac{\boldsymbol{\xi}}{2},\phi-\frac{\omega}{2}\right)P\left(\mathbf{r}+\frac{\boldsymbol{\xi}}{2},\phi+\frac{\omega}{2}\right)\\ &- W(\mathbf{r},\phi;\mathbf{r}-\boldsymbol{\xi},\phi-\omega)P\left(\mathbf{r},\phi\right)P\left(\mathbf{r}-\boldsymbol{\xi},\phi-\omega\right)\Bigg].\end{aligned} \tag{2.3}$$

It is worth to mention that later the additional term, describing excluded volume effect, will be introduced.

Long-wavelength expansion

To proceed, we observe that without loss of generality the probability distribution function can be expanded in Fourier harmonics

$$P\left(\mathbf{r},\phi\right) = \sum_{n=-\infty}^{\infty} P_n(\mathbf{r})e^{in\phi}, \tag{2.4}$$

where $P^*_{-n}(\mathbf{r}) = P_n(\mathbf{r})$, since P is real, and '$*$' denotes complex conjugation. Next, we note that motor-mediated interactions between microtubules are short-ranged, and the integrand in Eq. (2.3) is non-zero only when $|\boldsymbol{\xi}| \lesssim L$, independent of the particular form of the interaction strength W. Since we are interested in patterns that evolve slowly on scales comparable to L, we perform a gradient expansion of P and keep terms up to fourth order. Projecting the resulting equation on the s-th Fourier harmonic yields the following equation,

$$\begin{aligned}\partial_t P_s(\mathbf{r}) &= -s^2 D_r P_s(\mathbf{r}) + \overline{\nabla_i D_{ij}\nabla_j P(\mathbf{r},\phi)}^{\,s}\\ &+ \sum_{n,m=-\infty}^{\infty}\Bigg[\overline{I^{(0)}_{nm}}^{\,s} P_n P_m + \frac{1}{2}\overline{I^{(1)}_{i,nm}}^{\,s} A_{i,nm} + \frac{1}{8}\overline{I^{(2)}_{ij,nm}}^{\,s} A_{ij,nm} + \frac{1}{48}\overline{I^{(3)}_{ijk,nm}}^{\,s} A_{ijk,nm}\\ &\quad + \frac{1}{384}\overline{I^{(4)}_{ijkl,nm}}^{\,s} A_{ijkl,nm} + \cdots\Bigg]\\ &- \sum_{n,m=-\infty}^{\infty} P_n\Bigg[\overline{J^{(0)}_{nm}}^{\,s} P_m - \overline{J^{(1)}_{i,nm}}^{\,s}\nabla_i P_m + \frac{1}{2}\overline{J^{(2)}_{ij,nm}}^{\,s}\nabla_i\nabla_j P_m - \frac{1}{6}\overline{J^{(3)}_{ijk,nm}}^{\,s}\nabla_i\nabla_j\nabla_k P_m\\ &\quad + \frac{1}{24}\overline{J^{(4)}_{ijkl,nm}}^{\,s}\nabla_i\nabla_j\nabla_k\nabla_l P_m + \cdots\Bigg],\end{aligned} \tag{2.5}$$

where

$$\overline{(\dots)}^{s} = \frac{1}{2\pi}\int_0^{2\pi} e^{-is\phi}\,(\dots)\,, \tag{2.6}$$

and

$$A_{i,nm} = P_n\nabla_i P_m - P_m\nabla_i P_n,$$

$$\begin{aligned} A_{ij,nm} = {} & P_n\nabla_i\nabla_j P_m - 2\,(\nabla_i P_n)\,(\nabla_j P_m) \\ & + P_m\nabla_i\nabla_j P_n, \end{aligned}$$

$$\begin{aligned} A_{ijk,nm} = {} & P_n\nabla_i\nabla_j\nabla_k P_m - 3\,(\nabla_i P_n)\,(\nabla_j\nabla_k P_m) \\ & + 3\,(\nabla_i\nabla_j P_n)\,(\nabla_k P_m) - P_m\nabla_i\nabla_j\nabla_k P_n, \end{aligned}$$

$$\begin{aligned} A_{ijkl,nm} = {} & P_n\nabla_i\nabla_j\nabla_k\nabla_l P_m - 4\,(\nabla_i P_n)\,(\nabla_j\nabla_k\nabla_l P_m) \\ & + 6\,(\nabla_i\nabla_j P_n)\,(\nabla_k\nabla_l P_m) - 4\,(\nabla_i\nabla_j\nabla_k P_n)\,(\nabla_l P_m) \\ & + P_m\nabla_i\nabla_j\nabla_k\nabla_l P_n. \end{aligned}$$

In Eq. (2.5) all P_n's and P_m's are functions of $\mathbf{r}$ and t. The interaction integrals are given by

$$\begin{aligned} I^{(0)}_{nm} &= e^{i(n+m)\phi}\int d\boldsymbol{\xi}\int_{-\pi}^{\pi} d\omega\, W_1 e^{i(m-n)\frac{\omega}{2}}, \\ I^{(1)}_{i,nm} &= e^{i(n+m)\phi}\int d\boldsymbol{\xi}\int_{-\pi}^{\pi} d\omega\, W_1 e^{i(m-n)\frac{\omega}{2}}\xi_i, \\ I^{(2)}_{ij,nm} &= e^{i(n+m)\phi}\int d\boldsymbol{\xi}\int_{-\pi}^{\pi} d\omega\, W_1 e^{i(m-n)\frac{\omega}{2}}\xi_i\xi_j, \\ I^{(3)}_{ijk,nm} &= e^{i(n+m)\phi}\int d\boldsymbol{\xi}\int_{-\pi}^{\pi} d\omega\, W_1 e^{i(m-n)\frac{\omega}{2}}\xi_i\xi_j\xi_k, \\ I^{(4)}_{ijkl,nm} &= e^{i(n+m)\phi}\int d\boldsymbol{\xi}\int_{-\pi}^{\pi} d\omega\, W_1 e^{i(m-n)\frac{\omega}{2}}\xi_i\xi_j\xi_k\xi_l, \end{aligned} \tag{2.7}$$

and

$$
\begin{aligned}
J^{(0)}_{nm} &= e^{i(n+m)\phi} \int d\boldsymbol{\xi} \int_{-\pi}^{\pi} d\omega \, W_2 e^{-im\omega}, \\
J^{(1)}_{i,nm} &= e^{i(n+m)\phi} \int d\boldsymbol{\xi} \int_{-\pi}^{\pi} d\omega \, W_2 e^{-im\omega} \xi_i, \\
J^{(2)}_{ij,nm} &= e^{i(n+m)\phi} \int d\boldsymbol{\xi} \int_{-\pi}^{\pi} d\omega \, W_2 e^{-im\omega} \xi_i \xi_j, \\
J^{(3)}_{ijk,nm} &= e^{i(n+m)\phi} \int d\boldsymbol{\xi} \int_{-\pi}^{\pi} d\omega \, W_2 e^{-im\omega} \xi_i \xi_j \xi_k, \\
J^{(4)}_{ijkl,nm} &= e^{i(n+m)\phi} \int d\boldsymbol{\xi} \int_{-\pi}^{\pi} d\omega \, W_2 e^{-im\omega} \xi_i \xi_j \xi_k \xi_l,
\end{aligned}
\tag{2.8}
$$

where ξ_i are the Cartesian components of $\boldsymbol{\xi}$, and we introduced

$$
\begin{aligned}
W_1 &\equiv W\left(\mathbf{r} - \frac{\boldsymbol{\xi}}{2}, \phi - \frac{\omega}{2}; \mathbf{r} + \frac{\boldsymbol{\xi}}{2}, \phi + \frac{\omega}{2}\right), \\
W_2 &\equiv W(\mathbf{r}, \phi; \mathbf{r} - \boldsymbol{\xi}, \phi - \omega).
\end{aligned}
$$

Eq. (2.5) comprises an infinite hierarchy of equations for the Fourier harmonics $P_n(\mathbf{r}, t)$. Its practical application relies on a strategy to reduce the number of relevant fields to just a few harmonics, and on the ability to calculate the interaction integrals for a particular function W. Our approach to both these issues is discussed below in Sections 2.5.1 and 2.5.2, and in Section 2.1, respectively.

Diffusion terms

The diffusion coefficients in Eq. (2.3) are approximated by their values for a single rod of length L and diameter d moving in an infinite, three-dimensional fluid with viscosity η [8]

$$
D_r = 12 \frac{k_B T}{\pi \eta L^3} \ln(L/d), \tag{2.9}
$$

and

$$
D_{ij} = D_{\parallel} n_i(\phi) n_j(\phi) + D_{\perp} \left[\delta_{ij} - n_i(\phi) n_j(\phi)\right], \tag{2.10}
$$

where D_r is coefficient of rotational diffusion, while D_{ij} describes translational diffusion. In the above we use notations:

$$
\begin{aligned}
D_{\perp} &= \frac{k_B T}{4\pi \eta L} \ln(L/d), \\
D_{\parallel} &= 2 D_{\perp}.
\end{aligned}
$$

Here, T is the temperature of the solution, and k_B is the Boltzmann constant. Note that D_r is four times larger than the value given by Doi and Edwards [8] due to the difference in our choice of the angular variable (i.e. ϕ rather than $\mathbf{n}$). Using Eq. (2.10) in Eq. (2.5), and projecting onto the s-th Fourier harmonics, leads to the following contributions to the equations of motion

$$\begin{aligned}\partial_t P_s(\mathbf{r}) &= -s^2 D_r P_s(\mathbf{r}) + \frac{D_\parallel + D_\perp}{2}\nabla^2 P_s(\mathbf{r}) \\ &+ \frac{D_\parallel - D_\perp}{4}\left(\nabla_x^2 - 2i\nabla_x\nabla_y - \nabla_y^2\right) P_{s-2}(\mathbf{r}) \\ &+ \frac{D_\parallel - D_\perp}{4}\left(\nabla_x^2 + 2i\nabla_x\nabla_y - \nabla_y^2\right) P_{s+2}(\mathbf{r}) + \cdots ,\end{aligned} \tag{2.11}$$

where '$\cdots$' denotes contributions from the interaction integrals discussed below.

Formally, Eqs. (2.9) and (2.10) limit the scope of Eq. (2.5) to rather dilute suspensions far away from liquid-solid boundaries, while both assumptions are routinely violated in experiments [9–12]. As we will see below, the kinetic theory equations that we are going to derive will only depend on the ratios $D_\parallel/D_r$ and $D_\perp/D_r$ that are less sensitive to the local density of other microtubules and proximity of a boundary. We note, however, that a proper study of this effect is outside the scope of this work.

Interaction kernel

Within our kinetic theory, molecular details of motor-microtubules interactions are encoded at a coarse-grained level in the interaction function W. Its physical interpretation is given by Eq. (2.3), which identifies $W(\mathbf{r}_1, \phi_1; \mathbf{r}_2, \phi_2)$ as a rate at which two microtubular rods at $(\mathbf{r}_1, \phi_1)$ and $(\mathbf{r}_2, \phi_2)$ are displaced and re-oriented by molecular motors. These changes in the rods positions and orientations occur when a molecular motor is attached to both MTs and moves along them. Therefore, a motor-induced re-orientation event can only take place when the shortest distance between the MTs is not larger than the size of the motors. Since the latter is significantly smaller than the length of individual microtubules, or the typical size of the patterns formed by the suspension, see e.g. [6, 9], we consider motors to be point-like. Under this assumption, W is non-zero only when the MTs intersect in their original configuration.

The experimental system we model is a thin quasi-2D layer of MT-MM mixture. In such systems one of the MTs leaves the xy-plane of the suspension and deviates slightly into the third dimension. Such deviations are small compared either to L or the typical pattern size, hence we will treat such MTs as intersecting in 2D.

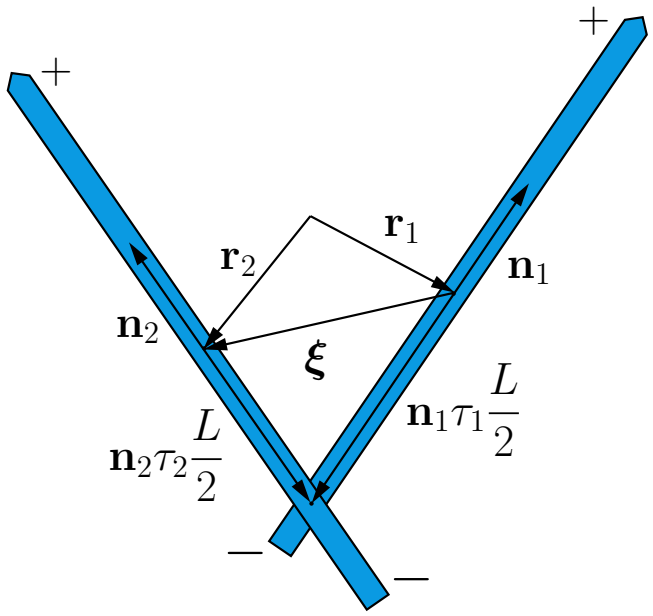

Figure 2.2: Intersection of two MT rods in 2D.

The intersection condition can be written as

$$\mathbf{r}_1 + \mathbf{n}_1\frac{L}{2}\tau_1 = \mathbf{r}_2 + \mathbf{n}_2\frac{L}{2}\tau_2, \tag{2.12}$$

where the left- and right-hand side of this equation is the position of the intersection point written with respect to the centre of mass (middle point) of either the first or the second MT, i.e. $\mathbf{r}_1$ or $\mathbf{r}_2$. The microtubule orientation is given by $\mathbf{n}_i = (\cos\phi_i, \sin\phi_i)$, $i = 1, 2$. Here we have introduced the dimensionless contour lenghts $\tau_{1,2}$ that parametrise the position along each microtubule: $\tau = -1$ corresponds to the "$-$"-end, and $\tau = 1$ to the "$+$"-end of the microtubule. By taking the cross product of Eq. (2.12) with either $\mathbf{n}_1$ or $\mathbf{n}_2$, the contour-length parameters can be found to be

$$\tau_1 = \frac{2}{L}\frac{\big((\mathbf{r}_2 - \mathbf{r}_1)\times\mathbf{n}_2\big)\cdot\mathbf{e}_z}{(\mathbf{n}_1\times\mathbf{n}_2)\cdot\mathbf{e}_z}, \tag{2.13}$$

$$\tau_2 = \frac{2}{L}\frac{\big((\mathbf{r}_2 - \mathbf{r}_1)\times\mathbf{n}_1\big)\cdot\mathbf{e}_z}{(\mathbf{n}_1\times\mathbf{n}_2)\cdot\mathbf{e}_z}, \tag{2.14}$$

where $\mathbf{e}_z$ is a unit vector perpendicular to the xy-plane. Since $|\tau_{1,2}|$ should be smaller than unity, the intersection condition can equivalently be written as $\Theta(1 - |\tau_1|)\,\Theta(1 - |\tau_2|) \neq 0$, where Θ is the Heaviside step function.

Having established the condition for MT rods intersection, we turn to modelling their re-orientation rate. Following Aranson and Tsimring [1], we take this rate to be proportional to the local motor density at the intersection point. In the following we assume that the motors are abundant in the solution, and their dynamics of association/dissociation with the microtubules are much

faster than the typical pattern-formation time. This was the case in several *in-vitro* experiments (see [13], for example).

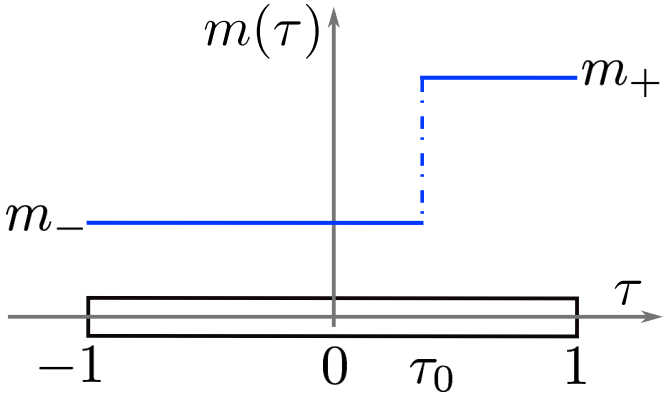

Figure 2.3: Model anisotropic distribution of the molecular motors along a microtubular filament.

With these assumptions, the motor distribution along individual microtubules instantaneously reaches its equilibrium profile (as it is discussed in the previous Chapter). For plus-directed motor density stays low and approximately constant in the proximity of the "$-$"-end of the microtubule, and rises sharply and saturates at another constant value close to the "$+$"-end. The equilibrium motor distribution $m(\tau)$, which gives the motor density at the contour length position τ, can therefore be approximated by

$$m(\tau) = m_- + (m_+ - m_-)\Theta(\tau - \tau_0), \tag{2.15}$$

where m_- and m_+ are the motor densities at the minus- and plus-ends, correspondingly, and τ_0 sets the position of the transition between those values; see Fig.2.3 for details.

The re-orientation rate can finally be written as

$$W\left(\mathbf{r}_1, \phi_1; \mathbf{r}_2, \phi_2\right) = G \underbrace{\Theta\big(1 - |\tau_1|\big)\Theta\big(1 - |\tau_2|\big)}_{\text{probability of intersection}} \underbrace{\left\{1 + \Xi\left[\Theta(\tau_1 - \tau_0) + \Theta(\tau_2 - \tau_0)\right]\right\}}_{\text{dependence on the local MM density}}. \tag{2.16}$$

where $\Xi = (m_+ - m_-)/(2m_-)$, and $\tau_{1,2}$ are given by Eqs. (2.13) and (2.14). The constant G is proportional to the motor properties, such as its processivity along the microtubules [6, 14], and varies with the motor type. However, as we will demonstrate below, G can be removed from the model by a rescaling of the dynamical fields. While its value would be important to map the parameter values used in the equations of motion back to dimensional units, it plays no role in determining the phase diagram of our model. Indeed, the interaction function W depends on two dimensionless parameters, τ_0 and Ξ, where the latter quantifies the mismatch between the motor densities at the two ends of a

microtubule. While it would be tempting to ignore this complexity and set $\Xi = 0$ for simplicity, previous work suggests this to be a crucial ingredient of the theory. As was shown by Aranson and Tsimring [1] for their model, there is no interesting pattern formation taking place in the absence of the motor density mismatch, and only a trivial instability is present in that case (see below). A similar conclusion was reached by Marchetti, Liverpool and co-workers [2–5], where the analogous parameter was the motor speed anisotropy along a microtubule. We, therefore, consider $\Xi > 0$ below.

Experimental data show that $(m_+ - m_-)/m_-$ (mismatch between the low motor density and high motor density) rarely exceeds 3 (look e.g. Fig. 2.3c). In our model we restrict its maximal value to 2, which corresponds to $\Xi_{max} = 1$. Thus, we vary parameter Ξ in the following range $0 < \Xi < 1$.

Parameter τ_0 does not play any crucial role in the model; the results presented below correspond to $\tau_0 = 0$ either $\tau_0 = 0.5$.

2.2 Approximations in the Aranson-Tsimring theory

In this section we review the approximations used by Aranson and Tsimring in [1] to evaluate the integrals in Eqs. (2.7) and (2.8), and to terminate the infinite hierarchy of coupled equations in Eq. (2.5). Here, we sketch their argument in some detail as it will be important in the further discussion.

The first step involves replacing the exact interaction kernel W in Eq. (2.16) with an effective simplified kernel, which is given by

$$W_{AT}\left(\mathbf{r}_1, \phi_1; \mathbf{r}_2, \phi_2\right) = \frac{\tilde{G}}{b^2\pi} \exp\left(-\frac{\left(\mathbf{r}_1 - \mathbf{r}_2\right)^2}{b^2}\right) \times \left[1 - \frac{\beta}{L}\left(\mathbf{r}_1 - \mathbf{r}_2\right) \cdot \left(\mathbf{n}_1 - \mathbf{n}_2\right)\right], \tag{2.17}$$

where $b \sim L$ is a lengthscale, and $\tilde{G}$ is a motor-related constant, similar to G in Eq. (2.16). This expression replaces the complicated spatial and angular dependence of Eq. (2.16) with a Gaussian cut-off that, essentially, allows any interactions as long as the bundle centres of mass are separated by a typical distance set by b; the term in the brackets can be seen as the first terms of the Fourier expansion of the true angular dependence in Eq. (2.16). The parameter β is a measure of how anisotropic the motor distribution is along individual microtubules, and is analogous to Ξ in Eq. (2.16). The obvious benefit of this approximation is that the integrals in Eqs. (2.7) and (2.8) can now be evaluated analytically. In [1] it is claimed that while not exact, Eq. (2.17) retains the main features of Eq. (2.16). We demonstrate in the next Sections that together with

the choice of the parameter b made in [1], the approximation in Eq. (2.17) leads to a different phase diagram with respect to that obtained when the original kernel Eq. (2.16) is retained.

The second approximation developed in [1] concerns the way to terminate the infinite hierarchy in Eq. (2.5). To illustrate this strategy, we neglect spatial variations of the probability distribution and keep only its angular dependence. This approximation implies that the dominant mechanism of the instability in this system should be the appearance of orientational order, while the density fluctuations are assumed to be subdominant. The validity of this approximation will be re-assessed after the same methodology is applied to the full system of equations with both the spatial and angular dependencies included. Using Eq. (2.17) in Eq. (2.5), and setting β and the spatial gradients to zero, we obtain

$$\begin{aligned}\partial_t P_s = &-s^2 D_r P_s - 2\pi\tilde{G} P_0 P_s \\ &+ \tilde{G} \sum_{m=-\infty}^{\infty} \frac{4\sin\frac{\pi}{2}(2m-s)}{2m-s} P_{s-m} P_m. \end{aligned} \tag{2.18}$$

Keeping only the first three Fourier harmonics in the expansion, this system of equations reads

$$\partial_t P_0 = 0, \tag{2.19}$$

$$\partial_t P_1 = -D_r P_1 + \tilde{G}\,(8-2\pi)\, P_0 P_1 - \frac{8}{3}\tilde{G} P_1^* P_2, \tag{2.20}$$

$$\partial_t P_2 = -4D_r P_2 + 2\pi\tilde{G}\left(P_1^2 - P_0 P_2\right), \tag{2.21}$$

where the first equation is the direct consequence of the total probability conservation. The isotropic solution of these equations is given by $P_1 = P_2 = 0$, while the evolution of small perturbations around this state, δp_1 and δp_2, is governed by the following equations,

$$\partial_t \delta p_1 = \lambda_1 \delta p_1, \qquad \partial_t \delta p_2 = \lambda_2 \delta p_2, \tag{2.22}$$

where $\lambda_1 = -D_r + \tilde{G}\,(8-2\pi)\, P_0$ and $\lambda_2 = -4D_r - 2\pi\tilde{G} P_0$; here, P_0 is a constant. The isotropic solution becomes unstable with respect to perturbations δp_1 when λ_1 becomes positive, while perturbations in the second mode, δp_2, are decaying since λ_2 is always negative. Therefore, close to the instability threshold the dynamics of the second mode P_2 is enslaved to the dynamics of the linearly unstable field P_1 [15], and P_2 can only acquire a non-zero value due to the non-linear forcing by the P_1^2 term in Eq. (2.21). Thus, P_2 quickly relaxes

to the value set by the r.h.s. of Eq. (2.21)

$$P_2 = \frac{2\pi\tilde{G}}{4D_r + 2\pi\tilde{G}P_0} P_1^2. \tag{2.23}$$

As can be shown from Eq. (2.18), the same holds for all higher modes P_m with $m > 1$, where $P_m \sim O\left(P_1^m\right)$. Since close to the instability threshold the saturated value of P_1 is small, all higher harmonics are significantly smaller, and can be neglected. Therefore, the authors of Ref. [1] restricted the infinite hierarchy Eq. (2.5) to contain only the first three modes, P_0, P_1 and P_2, where the latter does not possess its own dynamics but is assumed to be well-approximated by the adiabatically-adjusted value given in Eq. (2.23), even in the presence of spatial variations and non-zero β.

These approximations allow for Eq. (2.5) to be converted into a system of partial differential equations for the hydrodynamic (i.e., slowly varying) fields $\rho(\mathbf{r})$ and $\mathbf{p}(\mathbf{r})$ defined by the moments of $P(\mathbf{r}, \phi)$ as follows,

$$\rho(\mathbf{r}) = \int_0^{2\pi} d\phi P(\mathbf{r}, \phi) = 2\pi P_0(\mathbf{r}), \tag{2.24}$$

$$\begin{aligned}\mathbf{p}(\mathbf{r}) &= \frac{1}{2\pi}\int_0^{2\pi} d\phi\, \mathbf{n}(\phi) P(\mathbf{r}, \phi) \\ &= \left(\frac{P_{-1}(\mathbf{r}) + P_1(\mathbf{r})}{2}, \frac{P_{-1}(\mathbf{r}) - P_1(\mathbf{r})}{2i}\right).\end{aligned} \tag{2.25}$$

Here, $\rho(\mathbf{r})$ is the local density of microtubules, and $\mathbf{p}(\mathbf{r})$ is proportional to their local orientation; note that $\mathbf{p}$ is not a unit vector.

Using Eqs. (2.24) and (2.25) we can connect the field variables and corresponding Fourier harmonics:

$$\partial_t \rho(\mathbf{r}) = 2\pi \partial_t P_0(\mathbf{r}), \tag{2.26}$$

$$\partial_t p_x(\mathbf{r}) = \frac{\partial_t P_{-1}(\mathbf{r}) + \partial_t P_1(\mathbf{r})}{2}, \tag{2.27}$$

$$\partial_t p_y(\mathbf{r}) = \frac{\partial_t P_{-1}(\mathbf{r}) - \partial_t P_1(\mathbf{r})}{2i}. \tag{2.28}$$

The evolution equation for the s-th Fourier harmonic $\partial_t P_s = ...$ is defined by Eq. (2.5).

To render equations dimensionless, time, space and the slow fields ρ and $\mathbf{p}$ are scaled by D_r^{-1}, L and $\tilde{G}L^2/D_r$, respectively. The final dimensionless equa-

tions used in [1] read

$$\partial_t\rho = \nabla^2\left[\frac{\rho}{32} - \frac{B^2\rho^2}{16}\right] - \frac{\pi B^2 H}{16}\Big[3\nabla\cdot\left(\mathbf{p}\nabla^2\rho - \rho\nabla^2\mathbf{p}\right) + 2\partial_i\left(\partial_j\rho\partial_j p_i - \partial_i\rho\partial_j p_j\right)\Big] - \frac{7\rho_0 B^4}{256}\nabla^4\rho, \tag{2.29}$$

$$\partial_t\mathbf{p} = \frac{5}{192}\nabla^2\mathbf{p} + \frac{1}{96}\nabla(\nabla\cdot\mathbf{p}) + (\rho/\tilde{\rho}_{cr} - 1)\,\mathbf{p} - \tilde{A}_0|\mathbf{p}|^2\mathbf{p} - H\Big[\frac{\nabla\rho^2}{16\pi} - \Big(\pi - \frac{8}{3}\Big)\mathbf{p}(\nabla\cdot\mathbf{p}) - \frac{8}{3}(\mathbf{p}\cdot\nabla)\mathbf{p}\Big] + \frac{B^2\rho_0}{4\pi}\nabla^2\mathbf{p}, \tag{2.30}$$

where ρ_0 is the conserved average density, $B = b/L$, $H = \beta B^2$, and $\tilde{\rho}_{cr} = \pi/(4-\pi)$; the constant $\tilde{A}_0 = 16\pi/(3(\rho_0+4))$ and the corresponding term in Eq. (2.30) arise from the dimensionless version of Eq. (2.23).

In addition to the approximations developed above, Eqs. (2.29) and (2.30) entail some additional assumptions. First, the only non-linear terms (i.e. terms proportional to H) kept in these equations correspond to the lowest order non-zero terms in the gradient expansion (cubic and linear in gradients in the equations for ρ and $\mathbf{p}$, respectively). This is done to ensure that both equations are coupled to each other. Additionally, Eq. (2.30) contains a series of terms quadratic in the gradient that are linearised around ρ_0, giving rise to the last term in that equation. This linearisation is justified if there are only small density variations close to the instability threshold. Finally, to ensure the absence of short-wavelength-instability, the fourth-order terms in the gradient expansion are again linearised around ρ_0 to yield the biharmonic term in Eq. (2.29).

The analysis presented in the Aranson-Tsimring theory suggests that Eqs. (2.29) and (2.30) exhibit two linear instabilities: an isotropic-polar transition at $\rho_0 = \tilde{\rho}_c$, where the system acquires a global orientation $\mathbf{p}(\mathbf{r}) = \text{const}$, while $\rho(\mathbf{r}) = \rho_0$, and the bundling transition at $\rho_0 = \tilde{\rho}_b \equiv 1/(4B^2)$ with $\mathbf{p}(\mathbf{r}) = 0$, where the linearised diffusion-like term in Eq. (2.29) becomes negative indicating the tendency of the system to accumulate disordered microtubular bundles in localised clusters; both instabilities are long-wavelength and set in at the scale of the system size. By setting B such that $\tilde{\rho}_c < \tilde{\rho}_b$, Aranson and Tsimring could show numerically that for $\tilde{\rho}_c < \rho_0 < \tilde{\rho}_b$ Eqs. (2.29) and (2.30) exhibit a disordered quasi steady-state array of vortex and aster-like structures, dominated by vortices, at low H, and by asters, at larger H. For $\rho_0 > \tilde{\rho}_b$, there is a competition between vortices, asters, and disordered high-density clusters at high values of H.

Below we systematically examine the assumptions leading to Eqs. (2.29) and (2.30). First, we devise a semi-analytical strategy to evaluate the integrals in Eq. (2.5) with the exact interaction kernel Eq. (2.16) instead of the effective approximation Eq. (2.17). We will demonstrate that, as a result, the bundling

transition sets in at lower density than the instability towards a globally ordered state, substantially changing the phase diagram. This can already be seen from comparing Eq. (2.17) with Eq. (2.16): since L is the only lengthscale that appears in the true interaction kernel, the parameter b of the approximate kernel should only differ from L by a factor of order unity, which implies $\tilde{\rho}_b \approx 1/4 < \rho_c$. Next we note that the terms that appear in Eqs. (2.29) and (2.30) were selected on the basis of approximations whose validity is difficult to control *a priori*: as a result, close to the instability threshold the final equations combine terms which effectively are of different orders (in terms of the degree of smallness). We show how to systematically keep terms of the same order and that this requires modification of the closure given by Eq. (2.23). Finally, we observe that in the absence of anisotropy in the interaction kernel, i.e. $H = 0$, Eq. (2.29) exhibits pathological behaviour for $\rho_0 > \tilde{\rho}_b$, since there are no non-linear terms that can cut-off exponential growth of the linearly-unstable modes. The same problem persists at small values of H, while at large H the non-linear coupling to the orientation field limits the instability growth, as shown in [1]. To cure this problem, which is more severe when $\tilde{\rho}_b < \tilde{\rho}_{cr}$, here we explicitly account for excluded volume interactions between the microtubular bundles that stabilise the dynamics even in the absence of the orientation field.

2.3 Excluded Volume Interactions

In this Section, we incorporate the excluded volume interactions between microtubular bundles into the dynamic equation for the density.

Excluded volume interactions can be introduced directly in the Boltzmann-like equation [16], but this is more cumbersome.

Another approach is to start from the Smoluchowski equation, similarly to the work by Ahmadi *et al.* [4] and Baskaran and Marchetti [17], and then incorporate obtained terms into the dynamical equations that we derived from the Boltzmann-like Eq. (2.3). This method is provided in [18]. Formally, the two approaches are expected to be equivalent, but note their detailed comparison by Bertin *et al.* [16].

The interaction potential U between microtubular rods calculated in [18] reads:

$$\frac{U_{sc}(\mathbf{r},\phi)}{k_B T} = \frac{2}{\pi} L^2 \rho(\mathbf{r}) + \frac{1}{4\pi} L^4 \rho(\mathbf{r})^2. \tag{2.31}$$

The two terms in this expression are coming from the second and third irreducible integrals [19] that correspond to two-rod and three-rod interactions, respectively. As was shown by Ahmadi *et al.* [4], the first term leads to a contri-

bution to the density equation proportional to $\nabla^2\rho^2$. When added to Eq. (2.29), for example, this contribution can limit the growth of the density fluctuations only for certain values of the parameter B, the three-rod term leads to a contribution proportional to $\nabla^2\rho^3$ and provides a stabilisation mechanism for any density and any values of the parameters.

The first term in the equation above was discussed by Ahmadi *et al.* [4], and the three-dimensional version of the second term was discussed by Straley [20].

Diffusion of a rod in an external potential is described by the Smoluchowski equation [4, 8]

$$\frac{\partial P(\mathbf{r},\phi)}{\partial t} = \nabla_i D_{ij}\left(\nabla_j P(\mathbf{r},\phi) + P(\mathbf{r},\phi)\nabla_j \frac{U}{k_B T}\right), \tag{2.32}$$

where D_{ij} is given by Eq. (2.10). Using U_{sc} for the external potential (see Eq. (2.31)), projecting onto the zeroth Fourier mode (the procedure of projection is defined by Eq. (2.6)), and selecting only the terms containing the density, we arrive at the following contribution of the excluded volume effects to the dynamical equation for the density

$$\partial_t \rho = \frac{D_\parallel + D_\perp}{2\pi}\nabla^2\left(L^2\rho(\mathbf{r})^2 + \frac{1}{6}L^4\rho(\mathbf{r})^3\right) + \dots. \tag{2.33}$$

While the ρ^3 term provides stabilisation against the otherwise unbounded growth of the bundling instability, resolving the competition between the ρ^2 and ρ^3 terms numerically requires fine temporal resolutions, as at large timesteps the quadratic term can still lead to a finite-time blow-up due to an insufficient time for the qubic term to curb that growth. We, therefore, introduce a further approximation that allows us to avoid working with small timesteps by re-summing the virial expansion in Eq. (2.33) as

$$L^2\rho(\mathbf{r})^2 + \frac{1}{6}L^4\rho(\mathbf{r})^3 + \dots \approx L^2\rho(\mathbf{r})^2 e^{\frac{1}{6}L^2\rho(\mathbf{r})}, \tag{2.34}$$

where we added an infinite number of higher-order terms that mimic the effect of the higher order virial coefficients; their influence is small for sufficiently small densities, and their main function is to safe-guard against very fast growth of local density fluctuations in our numerical solutions presented below. Finally, the contribution of the excluded volume interactions to the density equation is written as

$$\partial_t \rho = \frac{D_\parallel + D_\perp}{2\pi}\nabla^2 L^2\rho(\mathbf{r})^2 e^{\frac{1}{6}L^2\rho(\mathbf{r})} + \dots, \tag{2.35}$$

where $\dots$ denote the diffusion terms from Eq.2.11, and the terms originating

from the interaction integrals are discussed next.

2.4 Evaluation of interaction integrals

In this Section we proceed by evaluating the interaction integrals from Eqs. (2.7) and (2.8) with the exact kernel Eq. (2.16). As an example, we calculate the value of $I^{(1)}_{j,nm}$ which contains the same technical features shared by all other interaction integrals, whose values are given in Appendix A.

By introducing new variables $\chi = \psi - \phi$ and $\boldsymbol{\zeta} = \boldsymbol{\xi}/L$, the integral $I^{(1)}_{j,nm}$ can be written as

$$\begin{aligned}\overline{I^{(1)}_{j,nm}}^{s} =& GL^3 \frac{1}{2\pi}\int_0^{2\pi} d\phi\, e^{i(n+m)\phi} e^{-is\phi} \int_0^{2\pi} d\chi \\ &\times \int_0^{\infty} d\zeta\, \zeta^2 \int_{-\pi}^{\pi} d\omega W_1 e^{i(m-n)\frac{\omega}{2}} \begin{pmatrix}\cos(\chi+\phi)\\ \sin(\chi+\phi)\end{pmatrix}_j ,\end{aligned} \tag{2.36}$$

where

$$\begin{aligned}W_1 =& \Theta\left(|\sin\omega| - 2\zeta\left|\sin\left(\chi-\frac{\omega}{2}\right)\right|\right)\Theta\left(|\sin\omega| - 2\zeta\left|\sin\left(\chi+\frac{\omega}{2}\right)\right|\right) \\ &\times\left\{1+\Xi\left[\Theta\left(-2\zeta\frac{\sin\left(\chi+\frac{\omega}{2}\right)}{\sin\omega}-\tau_0\right)+\Theta\left(-2\zeta\frac{\sin\left(\chi-\frac{\omega}{2}\right)}{\sin\omega}-\tau_0\right)\right]\right\}.\end{aligned} \tag{2.37}$$

Projection onto the s-th Fourier harmonics yields

$$\begin{aligned}&\frac{1}{2\pi}\int_0^{2\pi} e^{-is\phi} e^{i(n+m)\phi}\begin{pmatrix}\cos(\chi+\phi)\\ \sin(\chi+\phi)\end{pmatrix}_j d\phi = \\ &\begin{pmatrix}\left(e^{i\chi}\delta_{n,s-m-1} + e^{-i\chi}\delta_{n,s-m+1}\right)/2 \\ \left(e^{i\chi}\delta_{n,s-m-1} - e^{-i\chi}\delta_{n,s-m+1}\right)/(2i)\end{pmatrix}_j ,\end{aligned} \tag{2.38}$$

and the spatial components of $I^{(1)}_{j,nm}$ can be expressed as

$$\begin{aligned}\overline{I^{(1)}_{x,nm}}^{s} &= L^3 G \frac{B^{(1)}_{s,m}\delta_{n,s-m-1} + B^{(2)}_{s,m}\delta_{n,s-m+1}}{2}, \\ \overline{I^{(1)}_{y,nm}}^{s} &= L^3 G \frac{B^{(1)}_{s,m}\delta_{n,s-m-1} - B^{(2)}_{s,m}\delta_{n,s-m+1}}{2i},\end{aligned} \tag{2.39}$$

where

$$\begin{aligned}B^{(1)}_{s,m} =& G^{-1}\int_0^{2\pi} d\chi \int_0^{\infty} d\zeta\zeta^2 \int_{-\pi}^{\pi} d\omega W_1 e^{i(2m-s+1)\frac{\omega}{2}} e^{i\chi}, \\ B^{(2)}_{s,m} =& G^{-1}\int_0^{2\pi} d\chi \int_0^{\infty} d\zeta\zeta^2 \int_{-\pi}^{\pi} d\omega W_1 e^{i(2m-s-1)\frac{\omega}{2}} e^{-i\chi},\end{aligned}$$

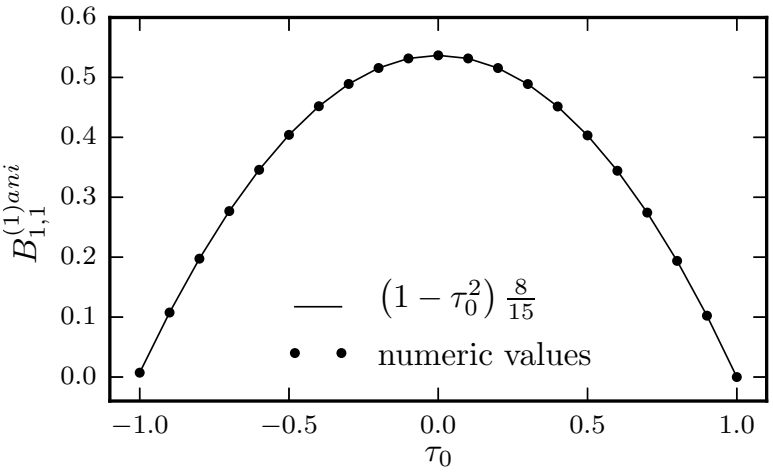

Figure 2.4: $B_{1,1}^{(1)ani}$ as a function of τ_0.

are functions of Ξ and τ_0. The structure of Eq. (2.37) suggests that each of these integrals can be split into two contributions

$$B_{m,s}^{(k)}(\Xi,\tau_0) = B_{m,s}^{(k)iso} + \Xi\, B_{m,s}^{(k)ani}(\tau_0), \tag{2.40}$$

where $B_{m,s}^{(k)iso}$ is a number associated with the isotropic Ξ-independent part of the kernel Eq. (2.16) (superindex iso means $isotropic$), while $B_{m,s}^{(k)ani}$ is a function of τ_0 (superindex $aniso$ means $anisotropic$). We evaluate these contributions numerically, as explained below.

We illustrate our method by calculating $B_{1,1}^{(1)}$. In this case, numerical integration on a grid with $\Delta\zeta = \Delta\omega = \Delta\chi = 0.01$ gives $B_{1,1}^{(1)iso} = 0$. We note, however, that in general the isotropic contributions to this and other integrals are not necessarily zero for all values of the indices. To evaluate the anisotropic part $B_{1,1}^{(1)ani}(\tau_0)$, we perform a similar numerical integration for a range of τ_0 from the interval $[-1,1]$, and plot the resulting values in Fig.2.4 (solid circles). We observe that these values are well-approximated by

$$B_{1,1}^{(1)ani}(\tau_0) = 0.5333\left(1-\tau_0^2\right) \approx \frac{8}{15}\left(1-\tau_0^2\right), \tag{2.41}$$

as can be seen from Fig.2.4 (solid line). We therefore obtain

$$B_{1,1}^{(1)}(\Xi,\tau_0) = 0.5333\Xi\left(1-\tau_0^2\right) \approx \frac{8}{15}\Xi\left(1-\tau_0^2\right). \tag{2.42}$$

All other integrals I's and J's, Eqs. (2.7) and (2.8), are evaluated in the same way. For all these integrals, the anisotropic contributions are simple polynomials in τ_0 that are readily guessed, while their prefactors and the isotropic contributions are well approximated by ratios of simple integers.

2.5 Hydrodynamic equations

We now have all the ingredients to formulate our version of the equations of motion for the hydrodynamic fields. As mentioned above, our approach differs from the work of [1] in several important ways, and we will show that this significantly changes the phase diagram of the system. In order to be able to attribute the changes observed to a particular aspect of our theory, we use the following approach. First, we use our values of the interaction integrals calculated with the exact kernel in Eq. (2.5) combined with a closure strategy employed in [1], see Eq. (2.23). Then we repeat the same derivation but with a different closure devised to keep only the terms that are relevant in the vicinity of the instability onset. In both cases we add the excluded volume terms to the equation for the density to be able to resolve the dynamics in the presence of a bundling instability, as discussed in Section 2.3.

2.5.1 Aranson-Tsimring Closure

Here, we repeat the derivation from Section 2.2 with our values of the interaction integrals. The equations are rendered dimensionless by scaling time, space and the Fourier harmonics of P by D_r^{-1}, L and GL^2/D_r, respectively. In Eq. (2.5), we keep only the first Fourier harmonics, P_0, $P_{\pm1}$, and $P_{\pm2}$, but drop any gradient of $P_{\pm2}$. For the second Fourier harmonics, Eq. (2.5) is an algebraic equation that is solved by $P_{\pm2} = A_0 P_{\pm1}^2$, similar to the closure Eq. (2.23), while for the density and orientation, Eqs. (2.24) and (2.25), we obtain

$$\begin{aligned}\partial_t\rho = \nabla^2\left[\frac{\rho}{32} - \frac{(1+a_3)\rho^2}{48\pi}\right] + \frac{1}{32\pi}\alpha\nabla^2\left(\rho^2 e^{\frac{\alpha\rho}{6}}\right) - \frac{91}{69120\pi}(1+a_5)\,\rho_0\nabla^4\rho \\ - \frac{1}{240}a_4\left[3\nabla\cdot\left(\mathbf{p}\nabla^2\rho - \rho\nabla^2\mathbf{p}\right) + 2\partial_i\left(\partial_j\rho\partial_j p_i - \partial_i\rho\partial_j p_j\right)\right], \quad (2.43)\end{aligned}$$

$$\begin{aligned}\partial_t\mathbf{p} = -\mathbf{p} + \frac{5}{192}\nabla^2\mathbf{p} + \frac{1}{96}\nabla(\nabla\cdot\mathbf{p}) + (1+a_1)\left(\frac{2}{3\pi}\rho\mathbf{p} - \frac{28}{15}A_0|\mathbf{p}|^2\mathbf{p}\right) \\ - a_2\left[\frac{\nabla\rho^2}{32\pi^2} - \frac{1}{20}\mathbf{p}(\nabla\cdot\mathbf{p}) - \frac{9}{20}(\mathbf{p}\cdot\nabla)\mathbf{p} + \frac{1}{24}\nabla(\mathbf{p}\cdot\mathbf{p})\right] \\ + (1+a_3)\,\frac{\rho_0}{40\pi}\left(\nabla^2\mathbf{p} + \frac{2}{9}\nabla(\nabla\cdot\mathbf{p})\right). \quad (2.44)\end{aligned}$$

Here,

$$A_0 = \frac{3\pi}{3\pi\,(1+a_1)^{-1} + \rho_0}, \quad (2.45)$$

and

$$
\begin{aligned}
a_1 &= \Xi\left(1-\tau_0\right), \\
a_2 &= \Xi(1-\tau_0^2), \\
a_3 &= \Xi\left(1-\tau_0\left(1+\tau_0^2\right)/2\right), \\
a_4 &= \Xi\left(1-\tau_0^2\left(1+\tau_0^2\right)/2\right), \\
a_5 &= \Xi\left(1-\tau_0\left(1+\tau_0^2\right)^2/2\right).
\end{aligned}
\tag{2.46}
$$

In Eq. (2.43), the term proportional to α is the dimensionless version of the excluded volume contribution from Eq. (2.35), where $\alpha = D_r/G$. This quantity can be understood as a ratio of two timescales, t_m/t_r, where $t_m \sim G^{-1}$ is a typical time over which a MT changes its orientation due to the activity of molecular motors, while $t_r \sim D_r^{-1}$ is a typical re-orientation time due to rotational diffusion. In the absence of motor activity, α becomes very large, and the excluded volume term prevents formation of any significant density fluctuations. In the motor-activity-dominated regime, α is small, and this regime is the focus of the rest of this work.

We also note that apart from the $\nabla(\mathbf{p}\cdot\mathbf{p})$ term and the excluded volume contribution, Eqs. (2.43) and (2.44) have the same tensorial structure as the equations in the Aranson-Tsimring theory, Eqs. (2.29) and (2.30). Perhaps surprisingly, though, the differences in their dependence on the parameters of the kernel, and different numerical prefactors are sufficient to produce a rather different phase diagram, as we discuss in Section 2.6.

2.5.2 Self-consistent closure and Q-tensor

The inherent problem of the previous closure is that it combines terms that are of various orders (equivalently, degrees of smallness) close to the instability threshold. Dropping spatial gradient in the equation for the second Fourier harmonics of P implies that, to obtain a coupled system, the density equation should contain third-order spatial gradients, whilst only first-order terms are sufficient in the orientation equation. To address this inconsistency, we employ a systematic procedure of deriving hydrodynamic equations that was originally developed for Ginzburg-Landau-like amplitude equations in pattern formation [15] and was recently applied in the context of self-propelled rods [21, 22] and microtubule-motor mixtures [23].

Similar to Eq. (2.30), Eq. (2.44) suggests that a uniformly polarised state becomes stable above some ρ_{cr}, given by the time- and spatially-independent version of Eq. (2.44). If we introduce $\epsilon^2 = \rho_0 - \rho_{cr}$, balancing the terms in Eq. (2.44) implies that $|\mathbf{p}| \sim \epsilon$, $\nabla \sim \epsilon$, $\partial_t \sim \epsilon^2$, and the deviation of the density $\rho(\mathbf{r},t)$ from its average value ρ_0 scales as $\delta\rho(\mathbf{r},t) \equiv \rho(\mathbf{r},t) - \rho_0 \sim \epsilon^2$. Using these

scalings we can see that the coupling terms, i.e. the terms proportional to a_4, in Eq. (2.43) contain a term proportional to $\rho_0\nabla^2(\nabla\cdot\mathbf{p})\sim\epsilon^4$, while the rest of the coupling terms are $\sim\epsilon^6$. Moreover, this scaling implies that ignoring spatial gradients of P_2 or spatial gradients in the equation for P_2 is not justified as, for example, the term $\nabla_i p_j$ is of the same order as $p_i p_j$, used in the algebraic closure above. Therefore, here we re-derive the equation for P_2 keeping all the terms that are $\sim\epsilon^2$.

To simplify the notation, we introduce the Q-tensor that is proportional to the second Fourier harmonics of $P(\mathbf{r},t)$,

$$Q_{ij}(\mathbf{r})=\frac{1}{\pi}\int_0^{2\pi}\left(n_i n_j-\frac{1}{2}\delta_{ij}\right)P(\mathbf{r},\phi)d\phi. \tag{2.47}$$

where $\mathbf{n}=(n_i,n_j)=(\cos\phi,\sin\phi)$. The two independent components of the Q-tensor can be explicitly written as follows,

$$Q_{xx}(\mathbf{r})=\frac{P_2(\mathbf{r})+P_{-2}(\mathbf{r})}{2},\qquad Q_{xy}(\mathbf{r})=\frac{P_{-2}(\mathbf{r})-P_2(\mathbf{r})}{2i}. \tag{2.48}$$

As it was mentioned in the previous Chapter, $Q_{yy}=-Q_{xx}$ and $Q_{yx}=Q_{xy}$ as the Q-tensor is traceless and symmetric. Keeping the terms proportional to ϵ^2 in Eq. (2.5) for the second harmonics, we obtain

$$\begin{aligned}Q_{ij}=\frac{1}{1+\frac{1}{3\pi}\rho_0(1+a_1)}\Bigg[&(1+a_1)\Big\{2p_ip_j-(\mathbf{p}\cdot\mathbf{p})\delta_{ij}\Big\}\\&+a_2\frac{\rho_0}{48\pi}\Big\{\partial_i p_j+\partial_j p_i-\delta_{ij}(\nabla\cdot\mathbf{p})\Big\}\Bigg],\end{aligned} \tag{2.49}$$

which, in the absence of spatial gradients, is the same as the closure used above. Similarly, keeping the leading terms in ϵ, which are proportional to ϵ^3 and ϵ^4 for the first and the zeroth harmonics, respectively, we arrive at the following dynamical equations

$$\begin{aligned}\partial_t\rho=&\nabla^2\left[\frac{\rho}{32}-\frac{(1+a_3)\rho^2}{48\pi}\right]+\frac{1}{32\pi}\alpha\nabla^2\left(\rho^2e^{\frac{\alpha\rho}{6}}\right)-\frac{91}{69120\pi}(1+a_5)\rho_0\nabla^4\rho\\&+\left[\frac{\pi}{48}-\frac{1}{36}(1+a_3)\rho_0\right]\partial_i\partial_j Q_{ij}+\frac{1}{80}a_4\rho_0\nabla^2(\nabla\cdot\mathbf{p}),\end{aligned} \tag{2.50}$$

$$\begin{aligned}\partial_t p_i=&-p_i+\frac{5}{192}\nabla^2p_i+\frac{1}{96}\nabla_i(\nabla\cdot\mathbf{p})+(1+a_1)\left(\frac{2}{3\pi}\rho\,p_i-\frac{28}{15}Q_{ij}p_j\right)\\&-a_2\left[\frac{1}{16\pi^2}\rho_0\partial_i\rho-\frac{1}{20}p_i(\nabla\cdot\mathbf{p})-\frac{9}{20}(\mathbf{p}\cdot\nabla)p_i+\frac{1}{24}\nabla_i(\mathbf{p}\cdot\mathbf{p})+\frac{1}{240}\rho_0\partial_kQ_{ik}\right]\\&+\frac{(1+a_3)\rho_0}{8}\left[\frac{1}{5\pi}\nabla^2p_i+\frac{2}{45\pi}\nabla_i(\nabla\cdot\mathbf{p})\right].\end{aligned} \tag{2.51}$$

In Eq. (2.50) we kept several terms that are inconsistent with this approximation scheme. While being of higher order than the rest of the equation, they represent the lowest order terms responsible for a particular effect. Thus, we keep the term that causes the bundling instability and the excluded volume term that saturates it, and we follow Aranson and Tsimring [1] in keeping the bilaplacian term that selects the lengthscale of the bundling instability. This system of equations is the central result of this Chapter.

2.6 Results

In this Section we present analysis of the dynamical behaviour exhibited by the models derived above. For convenience, we will be referring to Eqs. (2.43) and (2.44) as the Aranson-Tsimring-closure (ATC) model, and to Eqs. (2.50) and (2.51) – as the Q-tensor-closure (QC) model. First, we perform a linear stability analysis of the homogeneous and isotropic base state for both models and determine the regions of the parameter space where non-trivial behaviour can be expected. Then we perform direct numerical solutions of the ATC and QC models in these parts of the parameter space and discuss the resulting patterns.

2.6.1 Linear stability analysis

We start by observing that both models support exact solutions in the form of a homogeneous state with $\rho(\mathbf{r},t)=\rho_0$ and $\mathbf{p}(\mathbf{r},t)=\mathbf{P}$, as was already mentioned above. In both cases, the evolution equation for $\mathbf{P}$ is given by

$$\partial_t P_i = \left[-1+(1+a_1)\left(\frac{2}{3\pi}\rho-\frac{28}{15}A_0P^2\right)\right]P_i, \tag{2.52}$$

where $P=|\mathbf{P}|$. Trivially, $\mathbf{P}=0$ is always a solution to this equation for any density. For densities larger than

$$\rho_{cr}=\frac{3\pi}{2(1+a_1)}, \tag{2.53}$$

the isotropic solution loses its stability, as Eq. (2.52) suggests, and another solution sets in with

$$P=\frac{1}{1+a_1}\sqrt{\frac{15}{28}}\sqrt{\left(\frac{\rho_0}{\rho_{cr}}-1\right)\left(\frac{\rho_0}{2\rho_{cr}}+1\right)}, \tag{2.54}$$

and a random orientation selected through a spontaneous symmetry breaking. We refer to this solution as the *globally-ordered* state.

The homogeneous and isotropic state with $\rho(\mathbf{r},t)=\rho_0$ and $\mathbf{p}(\mathbf{r},t)=0$ is

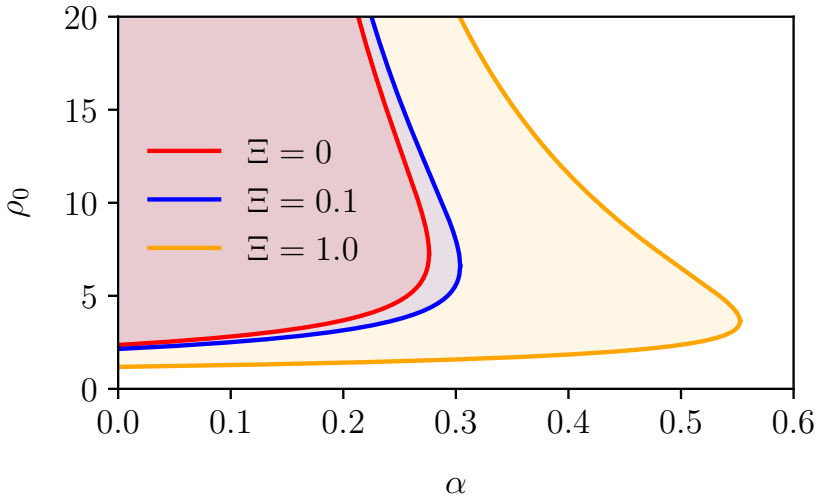

Figure 2.5: Regions of existence of the bundling instability for $\tau_0 = 0$ and various values of Ξ. The solid lines are solutions to Eq. (2.56), while the shaded regions indicate where the homogeneous and isotropic state is unstable with respect to density fluctuations (the bundling instability). The solid lines can therefore be seen as spinodal lines, and the shaded areas as regions of phase separation.

also unstable with respect to density fluctuations, as was already mentioned above; there, it was referred to as a *bundling* instability. Assuming small spatial variations of the density profile $\rho(\mathbf{r}, t) = \rho_0 + \delta\rho(t)e^{i(k_x x + k_y y)}$ and the absence of orientation fluctuations, the linear dynamics of the density perturbations are given by $\partial_t \delta\rho = \lambda_b(k)\delta\rho$, where

$$\lambda_b(k) = \left[-\frac{1}{32} + \frac{(1+a_3)\rho_0}{24\pi} - \frac{\alpha\rho_0}{192\pi}e^{\frac{\alpha\rho_0}{6}}\left(12 + \alpha\rho_0\right)\right]k^2 - \frac{91}{69120\pi}\left(1 + a_5\right)\rho_0 k^4, \tag{2.55}$$

and $k^2 = k_x^2 + k_y^2$. For a selected wavevector, density perturbations grow when $\lambda_b(k)$ becomes positive, which can only happen when the coefficient of k^2 is positive, since the prefactor of k^4 is negative for realistic values of τ_0. Therefore this instability sets in at a critical density ρ_b, given by

$$-\frac{1}{32} + \frac{(1+a_3)\rho_b}{24\pi} - \frac{\alpha\rho_b}{192\pi}e^{\frac{\alpha\rho_b}{6}}\left(12 + \alpha\rho_b\right) = 0, \tag{2.56}$$

which in the absence of the excluded volume, $\alpha = 0$, becomes $\rho_b = 3\pi/(4(1 + a_3))$, similar to the expression obtained in [1].

In Fig.2.5, we plot the solutions of Eq. (2.56) as a function of the excluded volume strength α for fixed values of the asymmetry parameter Ξ. For any value of Ξ, there exist two regions of this parameter space. For large values of α there is no bundling instability as strong excluded volume effects preclude

growth of any density variations. Instead, for smaller values of α there is a band of density values (the shaded regions in Fig.2.5), where the bundling instability exists. The upper boundary of this band goes to infinity when α approaches zero.

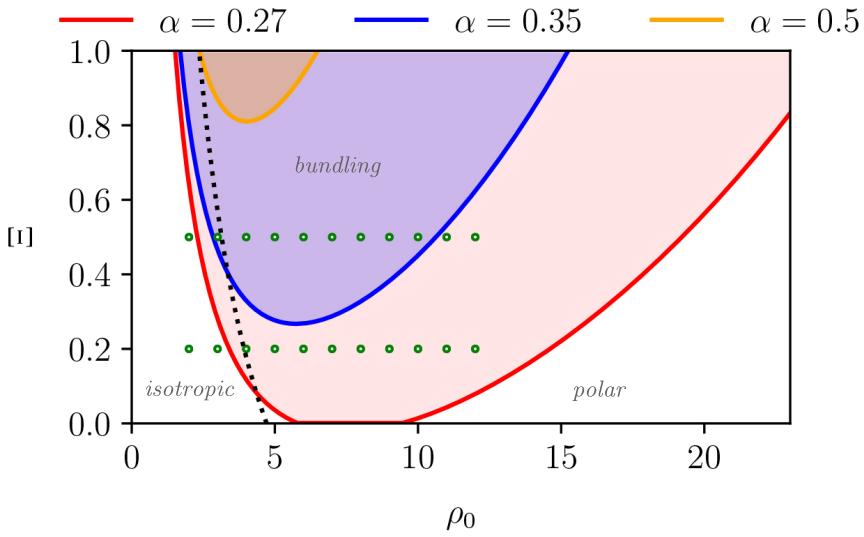

Figure 2.6: The data from Fig.2.5 replotted as Ξ vs. ρ_0 graph for $\tau_0 = 0$ and various values of α. The dotted black line is the onset of global order, given by Eq. (2.53). Green circles indicate point for which we perform direct numerical solutions with the ATC and QC models: $\tau_0 = 0$, $\alpha = 0.35$, $\Xi = 0.2$ and $\Xi = 0.5$ with $\rho_0 = 2, 3, \ldots, 12$.

Since α sets the strength of the excluded volume interactions we fix its value, and treat Ξ and ρ_0 as the control parameters. In Fig.2.6, we plot the instability boundaries found above in terms of these control parameters. The dotted black line in Fig.2.6 is the critical density ρ_{cr}, given by Eq. (2.53), while the solid lines, given by Eq. (2.56), enclose the region of the bundling instability (shaded regions in Fig.2.6). As α increases, the bundling instability is pushed towards larger values of Ξ, but is always present. We, therefore, select a representative case of $\alpha = 0.35$ (blue line and the blue shaded region in Fig.2.6), and perform direct numerical solutions of the ATC and QC models for a range of densities and fixed motor asymmetry parameter $\Xi = 0.2$ and $\Xi = 0.5$. The former case exhibits only the instability towards a globally ordered state, while the latter case has both types of instability. The densities we use in our simulations are denoted by green circles in Fig.2.6.

Finally, we note that a full linear stability analysis (see below) shows that the transition to global order and the bundling instability are the only instabilities of the homogeneous and isotropic state for both models.

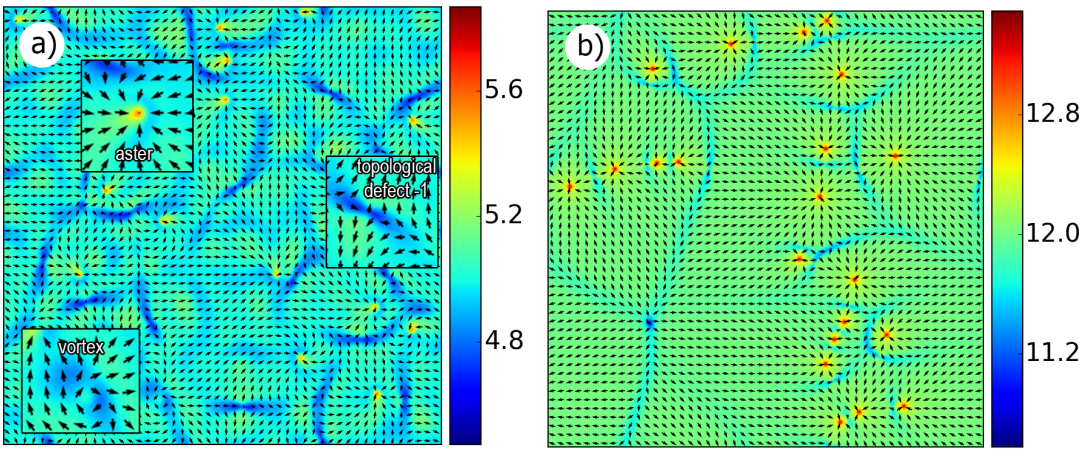

Figure 2.7: Instantaneous snapshots from the direct numerical solutions of the ATC model with $\tau_0 = 0$, $\alpha = 0.35$, and $\Xi = 0.2$: a) $\rho_0 = 5$, b) $\rho_0 = 12$. MT density is represented by colour map.

2.6.2 Direct numerical solutions

To explore the nonlinear behaviour of the ATC and QC models, we perform direct numerical solutions of Eqs. (2.43) and (2.44), and of Eqs. (2.50) and (2.51) in the parts of the parameter space identified above.

To solve PDE equations, we used our own FDM (Finite difference method) solver written in C language. We use a 2-dimensional grid of points, discretise spatial derivatives by second-order finite-differences, and employ a second-order predictor-corrector method for time integration [25]. For a finite difference approximations to derivatives at grid points we use five-point stencils [24]. Our computations are performed on square domains 150×150 with periodic boundary conditions. The domain has a topology of torus, which means that bottom border of the grid corresponds to the upper border, while the left border corresponds to the right one. We use spatial resolution $\Delta h = 0.5$, where the unit length is chosen to be the microtubular length (see Section 2.5 for details of our dimensional units); the time step is set to $\Delta t = 0.005$. Unless explicitly stated, we set $\alpha = 0.35$ and $\tau_0 = 0$, as discussed above. Initial conditions correspond to the constant density ρ_0 with the white noise (the amplitude of noise equals 0.05) and we set the initial orientation equal to 0 ($\mathbf{p} = 0$). The range of execution time of individual computation varies from 1 hour to 24 hours.

Below we present our results in composite images showing simultaneously the local density profile $\rho(\mathbf{r})$ (colour) and the orientation vector field $p(\mathbf{r})$ (arrows), normalised by its magnitude in the globally-ordered state, Eq. (2.54). To visualise our results we use the free matplotlib Python library.

We start by examining the behaviour of the ATC model for $\Xi = 0.2$ where, according to Fig.2.6 one should expect a transition to global polar order for

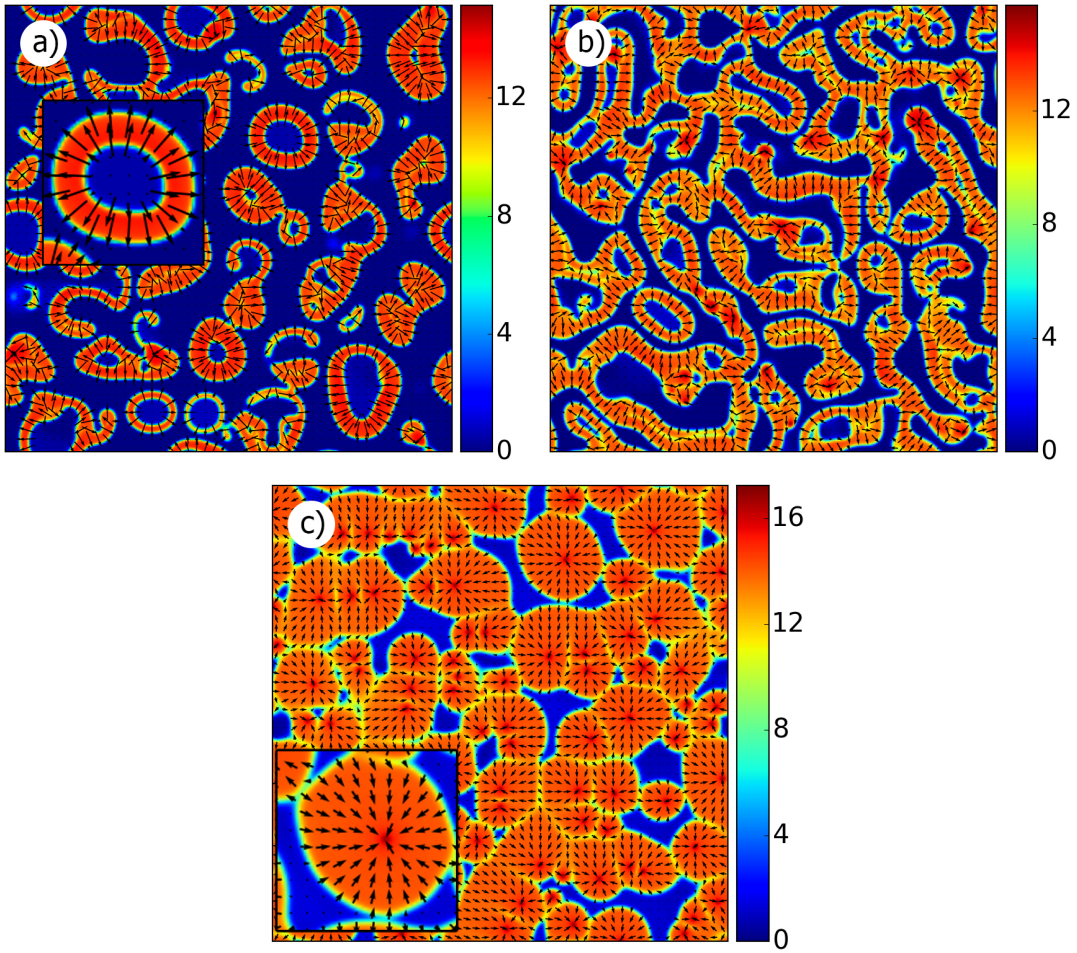

Figure 2.8: Same as Fig.2.7 but with $\Xi = 0.5$ a) $\rho_0 = 5$, b) $\rho_0 = 7$, c) $\rho_0 = 12$. MT density is represented by colour map.

sufficiently high densities. For $\rho_0 = 2$ and 3, there exists no instability of the homogeneous and isotropic state, and any random initial condition in our simulations quickly returns to that state. For densities above the global-instability threshold (black dotted line in Fig.2.6), we observe rapid formation of a globally oriented state with a large number of defects, as can be seen from Fig.2.7 a for $\rho_0 = 5$. These defects consist of vortices, inward-pointing asters that correspond to an increase of the local density, and spatially-distributed defects of the opposite topological charge that correspond to the minima of the local density. After sufficiently long simulation times, these defects annihilate leaving behind a uniform, globally polarised state. The same behaviour persists at higher densities, the only difference being that there are now sharper density gradients around topological defects. We also observe that the typical time for all defects to annihilate grows quickly with ρ_0. In Fig.2.7 b, for instance, we show the final snapshot of a long run for $\rho_0 = 12$, which continued to coarsen over the course of the whole simulation.

At $\Xi = 0.5$ the behaviour of the ATC model changes considerably. According to Fig.2.6, as the density is increased, the bundling instability is the first

one to set in. For larger densities, the bundling instability co-exists with the globally polarised state, while at yet large densities, one should again expect uniform polar order throughout the system. This scenario is supported by our direct numerical solutions. Below the bundling instability threshold, the system always returns to the homogeneous and isotropic state. At higher densities, we observe the following dynamical structures. For $\rho_0 = 5$ and $\rho_0 = 7$, (Figs.2.8 a and 2.8 b, respectively), the bundling instability competes with the emergence of global order, and the ensuing high-density clusters tend to elongate to keep local orientation aligned. Such elongated clusters often end up in yet-higher-density regions with inward-pointing asters. Even after a long time, the system does not settle into a steady-state; instead its dynamics comprise slow re-arrangements of the high-density clusters, mostly along the direction set by the local orientation, punctuated by fast re-orientation waves that align locally the orientation vector with the density gradient. A similar behaviour is observed in simulations with $\rho_0 = 3$, which is within a narrow range of densities that are below the global instability threshold, but above the bundling instability one. In this case the system first develops clusters of high density dispersed in a low-density background until the local density inside the clusters exceeds the global instability threshold, after which the dynamics resemble its higher-density counterpart discussed above. At yet higher density, above the bundling instability region ($\rho_0 = 12$, see Fig.2.8 c), the system does not exhibit global order as predicted by the linear stability analysis (Fig.2.6). Instead it forms high-density clusters, which tend to merge into large-scale structures at very long times, see Fig.2.8 c. Each cluster contains orientation field in the form of inward-pointing asters. Perhaps, this state may be viewed as an example of microphase separation, as clusters do not coarsen indefinitely but appear to reach a self-limiting size. However, we do not know whether it survives at yet longer simulation times or in larger systems.

Now we compare these observations against the results of our direct numerical solutions of the QC model. Since the linear stability properties of the homogeneous and isotropic state are the same for both models, one might expect the QC model to exhibit a dynamical behaviour similar to the ATC one. Surprisingly, the two models are instead substantially different. As for the ATC model, the cases of $\rho_0 = 2$, with $\Xi = 0.2$ and 0.5, and of $\rho_0 = 3$, with $\Xi = 0.2$, yield no instabilities, and the system returns to the homogeneous and isotropic state. Above the global instability threshold, the QC model exhibits the same type of dynamics for both $\Xi = 0.2$ and $\Xi = 0.5$ (see Fig.2.9 and Fig.2.10, respectively). Although visually these structures appear to be similar to the ATC patterns at $\Xi = 0.5$ (see Figs.2.8 a and 2.8 b, for instance), their dynamical signatures are very different. While the high-density clusters of the ATC model exhibit slow, largely coarsening-type dynamics with the orientation quickly

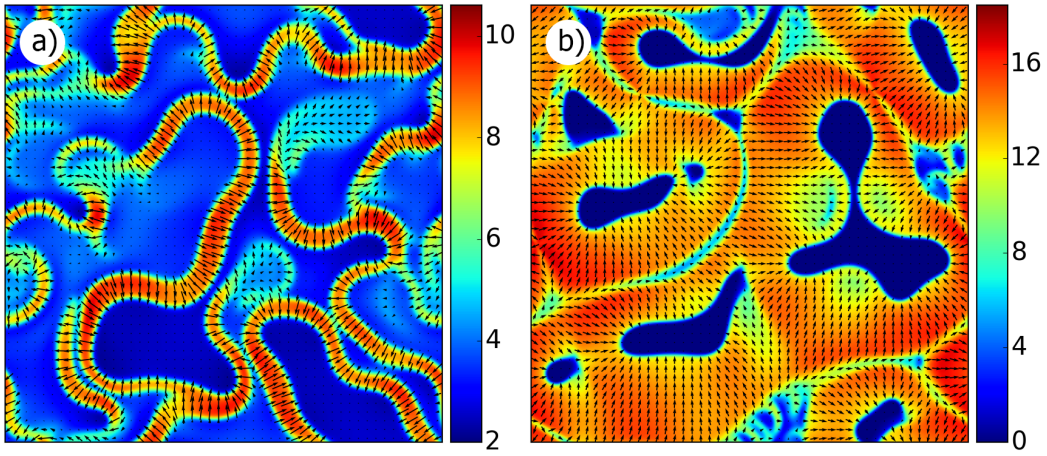

Figure 2.9: Instantaneous snapshots from the direct numerical solutions of the QC model with $\tau_0 = 0$, $\alpha = 0.35$, and $\Xi = 0.2$: a) $\rho_0 = 5$, b) $\rho_0 = 11$. MT density is represented by colour map.

adjusting to slowly evolving local density gradients, here the density and orientation evolve on comparable timescales, never settle down, and appear to be chaotic for any value of Ξ and ρ_0 in Figs.2.9 and 2.10. Even in the regions of approximately homogeneous local density, the orientation field exhibits significant time dependence, suggesting that the globally polarised state is linearly unstable for these parameters.

To validate this statement, we performed a linear stability analysis of the globally polarised state for the ATC and QC models, see Appendix A. First, this analysis confirms that the homogeneous and isotropic state, $P = 0$, of both models does not have any other instability than the bundling and global-order instabilities, discussed above. Next, we observe that while the globally polarised state is always linearly stable for the ATC model, for the QC model there is a range of parameters where it becomes unstable with respect to coupled orientation and density fluctuations. In Fig.2.11 we plot the results of both types of linear stability analysis of the QC model. There, the black dotted line and the blue dashed line (both taken from Fig.2.6) correspond to the instability boundary of the globally-oriented state and the region of the bundling instability, respectively. The solid brown line marks the boundary above which the globally ordered state is linearly unstable. Additionally, within that region there are two possible instability modes. The first one is characterised by a modulation in the density and orientation *along* the direction of the global order (magenta shaded region) and provided by several effects including the effective conractile flux of MTs; the second has modulations *both perpendicular and parallel* to that direction (brown shaded region). We, therefore, speculate that when there is global order (i.e., above or to the right of the dotted black line in Fig.2.11), the QC model exhibits three types of behaviour that cannot co-exist: (i) the tendency to create global orientation with a uniform density

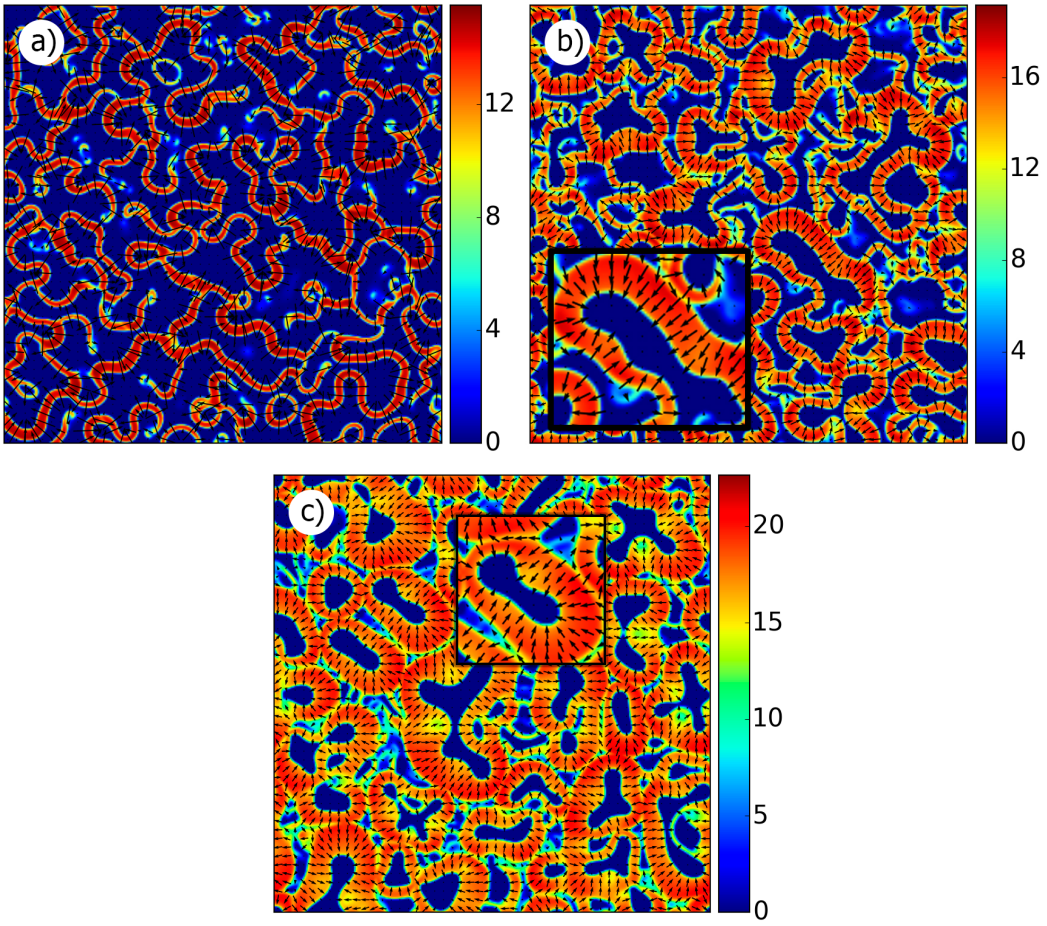

Figure 2.10: Same as Fig.2.9 but with $\Xi = 0.5$, a) $\rho_0 = 4$, b) $\rho_0 = 8$, c) $\rho_0 = 12$. MT density is represented by colour map.

profile, (ii) the bundling instability, and (iii) the instability of the global order. The interaction between these three instabilities is what leads to irregular dynamics, as we see in Figs.2.9 and 2.10.

As we can see from Fig.2.11, for $\rho_0 > 3$, all our simulations (green circles) belong to the unstable region of the parameter space. We therefore performed additional simulations (not shown) of the QC model for $\Xi = 0.2$ with $\rho_0 = 20$ and $\Xi = 0.5$ with $\rho_0 = 25$, that both lie outside the unstable region (brown line), and confirmed the absence of chaotic-like behaviour at long times. Instead, both systems settled into a globally polarised state interlaid with topological defects, similarly to the case of the ATC model.

The non-trivial dynamics presented above relies on the simultaneous existence of at least two types of instability for the same values of Ξ and ρ_0. Fig.2.5 suggests that for moderate values of Ξ, the bundling instability only exists for small values of α. To study the dynamics of both models outside of this regime, we set $\alpha = 0.6$ and considered $\Xi = 0.2$ and $\Xi = 0.5$, as before. The linear stability analysis of the globally polarised state suggests that both the ATC and QC models are linearly stable in that regime, and the only instability thresh-

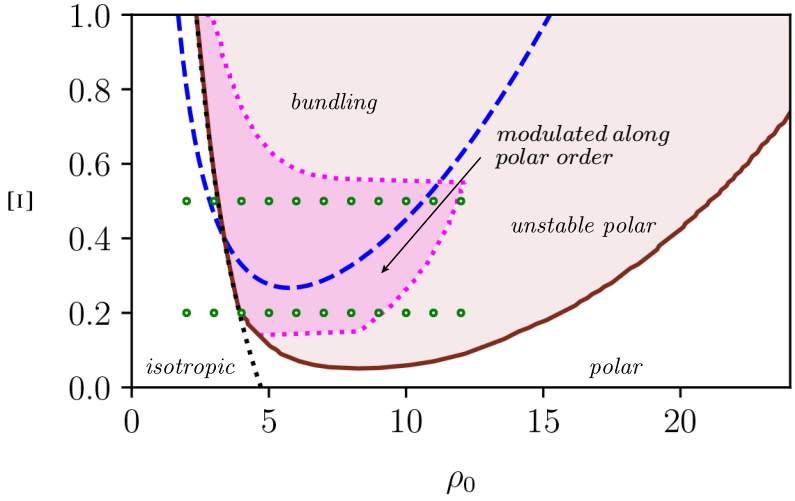

Figure 2.11: Linear stability diagram of the QC model for $\tau_0 = 0$ and $\alpha = 0.35$. As in Fig.2.6, the dotted black line is the onset of global order, given by Eq. (2.53), and the dashed blue line delineates the region of the parameter space where the homogeneous and isotropic state exhibits the bundling instability (the same as the solid blue line in Fig.2.6). The brown solid line indicates the region where a homogeneous, globally-ordered state becomes linearly unstable. Inside this line we also specify the instability mode: magenta-shaded region corresponds to the density and orientation fluctuations modulated along the direction of the global order, while the brown-shaded region corresponds to modulations both perpendicular and parallel to that direction.

old is given by Eq. (2.53). Our simulations confirm that both models exhibit rather simple dynamics, similar to the case of the ATC model with $\Xi = 0.2$ and $\alpha = 0.35$: below ρ_{cr}, the system returns to the homogeneous and isotropic state, while above ρ_{cr}, it goes through a series of long-lived topological defects before, eventually, settling into the homogeneous and isotropic state. At the highest density considered, $\rho_0 = 12$, the system gets trapped into a state with an apparently stable (or long-lived metastable) arrangement of topological defects (see Fig.2.12). The main difference between the two models, however, is that the inward-pointing asters of the ATC model correspond to local density enhancement, while similar topological defects in the QC model lead to local density minima.

The two situations presented above, $\alpha = 0.35$ and $\alpha = 0.6$, seem to comprehensively cover the behaviour of the ATC and QC models, and we have not observed any other dynamical structures besides the patterns presented above. As mentioned at the beginning of this Section, we restricted our simulations to a realistic, albeit arbitrary, case of $\tau_0 = 0$. Another value of τ_0 would lead to a quantitative effect on the instability boundaries, while the qualitative behaviour is still the same. This is only the case for $1 + a_5 > 0$, as Eq. (2.55) suggests, which is always true for $\Xi < 1$. When $1 + a_5 < 0$, the bilaplacian terms in

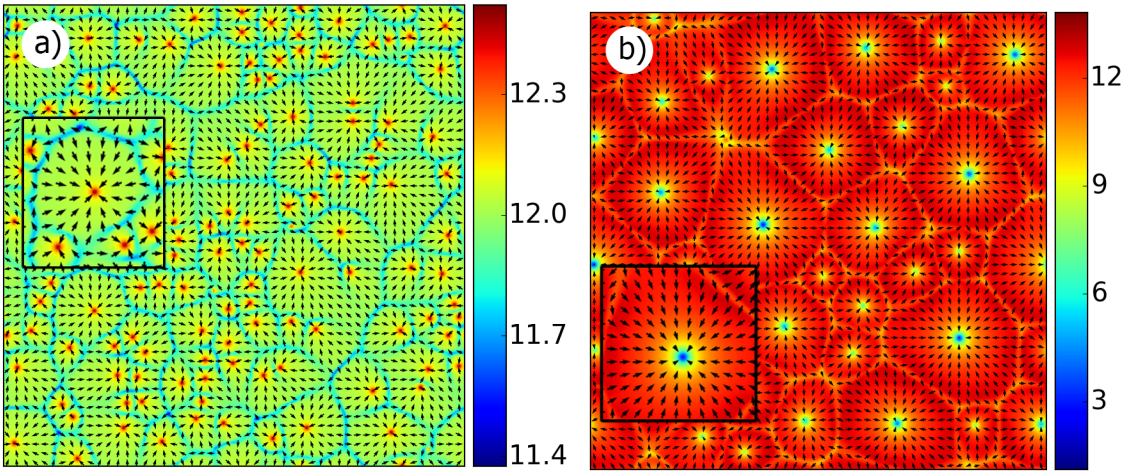

Figure 2.12: Comparison between the long-time dynamics of the ATC (a) and QC (b) models with $\tau_0 = 0$, $\alpha = 0.6$, $\Xi = 0.5$ and $\rho_0 = 12$. MT density is represented by colour map.

Eqs. (2.43) and (2.50) do not result in the lengthscale selection for the bundling instability, and a yet higher-order gradient has to be added to the equations in that case.

2.7 Discussion

The main goal of this Chapter was to revisit the kinetic theory of microtubule-motor mixtures originally derived in [1], as well as its coarse-graining into a set of dynamical equations for (slowly-varying) density and orientation fields, Eqs. (2.29) and (2.30). We also studied (by linear stability analysis and direct numerical solutions) the resulting equations, and analysed the corresponding pattern formation dynamics.

In particular, we considered the validity of the effective interaction kernel, Eq. (2.17), used in [1]. To address this issue, we developed a semi-analytical method that allowed us to calculate the interaction integrals, Eqs. (2.7) and (2.8), exactly. We also studied the closure relationship, Eq. (2.23), used in [1], and compared it to a closure method routinely used in Ginzburg-Landau-type theories of pattern formation [15, 21–23]. We derived two dynamical systems of equations, which we respectively called ATC model and QC model, that utilise our approximation-free values of the interaction integrals, but use various closure relations. While the ATC model uses the same closure as [1], the QC model uses the self-consistent closure derived in Section 2.5.2. Together with the original equations of Aranson and Tsimring, Eqs. (2.29) and (2.30) (which we refer to as the original Aranson-Tsimring model), these models allowed us to assess the importance of each of the assumptions mentioned above.

We used a linear stability analysis and direct numerical solutions to compare these three models. For the parameters of the effective kernel chosen by Aranson and Tsimring [1], the model predicts three types of behaviour: (i) the homogeneous and isotropic state for low densities, (ii) the globally-polarised state with various topological defects for intermediate densities, and (iii) the bundling instability leading to the formation of high-density clusters at high densities. Our analysis with the exact kernel demonstrated that under similar assumptions the order of the phases is different, with the bundling instability often setting in *before* the globally-polarised state. Therefore, in order to fully resolve the dynamics at late times, the equations of motion should have a physical mechanism that limits the otherwise unchecked growth of the bundling instability. The original Aranson-Tsimring model simply relies on the non-linear coupling terms (i.e., terms proportional to H) in Eq. (2.29) to cut the growth of density fluctuations – however this is a viable route only for sufficiently large values of H. To cure this problem we introduced steric repulsion between the microtubular rods: this has to be calculated up to the third virial coefficient or higher in order to provide a stabilisation mechanism that works for any density. This procedure allowed us to resolve the dynamics of our models in the region of the parameter space where the bundling and global instabilities co-exist. Our main conclusion here is that the usage of the exact kernel significantly alters the positions of the instability boundaries and, unless the exclusion volume parameter α is rather large, the bundling instability co-exists with the global order, leading to patterns absent from the original Aranson-Tsimring model [1]. When the bundling instability is absent, the ATC model exhibits the transition to a globally-polarised state, mediated by a variety of topological defects, similar to the original Aranson-Tsimring model [1].

Additionally, by comparing the ATC and QC models, we concluded that the self-consistent closure employed in the latter model, changes the stability properties of the globally-polarised state in the region of the parameter space where it co-exists with the bundling instability, leading to seemingly chaotic patterns. Also, the topological defects observed for this model in the absence of the bundling instability are of rather different nature than the corresponding defects in the ATC or original Aranson-Tsimring models.

We, therefore, conclude that out of the three sets of equations we compared, the QC model more faithfully reproduces the long-wavelength dynamics of Eq. (2.5) with Eq. (2.16). When either the effective kernel Eq. (2.17) or a closure similar to Eq. (2.23) is employed, the resulting phase diagram differs significantly from the phase diagram of the QC model. This suggests that it might be of interest to analyse how the results in previous studies on microtubule-motor mixtures such as [26] may be affected by the use of the QC equations of motion.

We would like to point out that there is another additional remarkable difference between the QC and the other two models: in the absence of anisotropy of interaction i.e., for $\Xi = 0$ – the density and the orientation equations of the Aranson-Tsimring and the ATC models decouple from each other, while this is not the case in the QC model, which still exhibits dynamical, seemingly chaotic patterns, similar to the $\Xi \neq 0$ case (not shown).

Since QC model is self-consistent and provides coupling between equations for density and polar order even in the absence of anisotropy, we assume that this closure better approximates the exact solution of the Boltzmann-like equation Eq. (2.3). However, to check this statement one should solve it exactly. Unfortunately, the high dimensionality of the phase space makes this problem extremely difficult from both the theoretical and computational points of view.

Additionally, there is a need to understand the role that potential microtubular self-propulsion, discussed by Liverpool, Marchetti and co-workers [2–5], might play in the dynamics of microtubules-molecular motor mixtures. We plan to address some of these questions in our future work.

Finally, we note that as the main goal of this study was to hone the techniques required to derive consistent hydrodynamic equations, we adopted a simple set of collision rules, formulated in Fig.2.1, that are the basis for Eq. (2.3), and the expression for the interaction kernel, Eq. (2.16). Detailed studies of the interactions between microtubular rods suggest that considered interaction rule does not cover all kinesin motors; that is why we consider more sophisticated rule in the next Chapter.

References

[1] I. S. Aranson and L. S. Tsimring, "Theory of self-assembly of microtubules and motors," *Phys. Rev. E*, vol. 74, p. 31915, 2006.

[2] T. B. Liverpool and M. C. Marchetti, "Instabilities of Isotropic Solutions of Active Polar Filaments," *Phys. Rev. Lett.*, vol. 90, p. 138102, 2003.

[3] T. B. Liverpool and M. C. Marchetti, "Bridging the microscopic and the hydrodynamic in active filament solutions," *EPL*, vol. 69, no. 5, p. 846, 2005.

[4] A. Ahmadi, M. C. Marchetti, and T. B. Liverpool, "Hydrodynamics of isotropic and liquid crystalline active polymer solutions," *Phys. Rev. E*, vol. 74, p. 061913, 2006.

[5] M. C. Marchetti, J.-F. Joanny, S. Ramaswamy, *et al.*, "Hydrodynamics of soft active matter," *Rev. Mod. Phys.*, vol. 85, no. 3, p. 1143, 2013.

[6] J. Howard, *Mechanics of Motor Proteins and the Cytoskeleton*. Sinauer Associates, Publishers, 2001.

[7] T. Guérin, J. Prost, P. Martin, and J.-F. Joanny, "Coordination and collective properties of molecular motors: theory," *Curr. Opin. Cell Biol.*, vol. 22, pp. 14–20, 2010.

[8] M. Doi and S. F. Edwards, *Theory Polym. Dyn.* Oxford University Press, 1986.

[9] T. Sanchez, D. T. N. Chen, S. J. Decamp, M. Heymann, and Z. Dogic, "Spontaneous motion in hierarchically assembled active matter," *Nature*, vol. 491, no. 11591, pp. 1–5, 2012.

[10] F. C. Keber, E. Loiseau, T. Sanchez, *et al.*, "Topology and dynamics of active nematic vesicles," *Science (80-.).*, vol. 345, no. 6201, pp. 1135–1139, 2014.

[11] S. J. DeCamp, G. S. Redner, A. Baskaran, M. F. Hagan, and Z. Dogic, "Orientational order of motile defects in active nematics," *Nat. Mater.*, vol. 14, pp. 1110–1115, 2015.

[12] D. Needleman and Z. Dogic, "Active matter at the interface between materials science and cell biology," *Nat. Rev. Matt.*, vol. 2, p. 17048, 2017.

[13] T. Surrey, "Physical Properties Determining Self-Organization of Motors and Microtubules," *Science (80-.).*, vol. 292, no. 5519, pp. 1167–1171, 2001.

[14] R. A. Cross and A. McAinsh, "Prime movers: the mechanochemistry of mitotic kinesins," *Nat. Rev. Mol. Cell Biol.*, vol. 15, no. 4, pp. 257–271, 2014.

[15] M. C. Cross and P. C. Hohenberg, "Pattern-Formation Outside of Equilibrium," *Rev. Mod. Phys.*, vol. 65, pp. 851–1112, 1993.

[16] E. Bertin, A. Baskaran, H. Chaté, and M. C. Marchetti, "Comparison between Smoluchowski and Boltzmann approaches for self-propelled rods," *Phys. Rev. E*, vol. 92, p. 042141, 2015.

[17] A. Baskaran and M. C. Marchetti, "Nonequilibrium statistical mechanics of self-propelled hard rods," *J. Stat. Mech.*, vol. 2010, p. P04019, 2010.

[18] I. Maryshev, D. Marenduzzo, A. B. Goryachev, and A. Morozov, "Kinetic theory of pattern formation in mixtures of microtubules and molecular motors," *Phys. Rev. E*, vol. 97, p. 22412, 2018.

[19] J. E. Mayer and M. G. Mayer, *Stat. Mech.* John Wiley & Sons, Inc., 1947.

[20] J. P. Straley, "Third virial coefficient for the gas of long rods," *Mol. Cryst. Liq. Cryst.*, vol. 24, p. 7, 1973.

[21] A. Peshkov, I. S. Aranson, E. Bertin, H. Chaté, and F. Ginelli, "Nonlinear field equations for aligning self-propelled rods," *Phys. Rev. Lett.*, vol. 109, no. 26, p. 268701, 2012.

[22] A. Peshkov, E. Bertin, F. Ginelli, and H. Chaté, "Boltzmann-Ginzburg-Landau approach for continuous descriptions of generic Vicsek-like models," *Eur. Phys. J. Spec. Top.*, vol. 223, pp. 1315–1344, 2014.

[23] F. Ziebert and W. Zimmermann, "Nonlinear competition between asters and stripes in filament-motor systems," *Eur. Phys. J. E*, vol. 18, pp. 41–54, 2005.

[24] M. Abramowitz and I. A. Stegun, *Handbook of Mathematical Functions with Formulas, Graphs, and Mathematical Tables*. New York: Dover, 1964.

[25] W. H. Press, S. A. Teukolsky, W. T. Vetterling, and B. P. Flannery, *Numerical Recipes 3rd Edition: The Art of Scientific Computing*. New York, NY, USA: Cambridge University Press, 3 ed., 2007.

[26] F. Ziebert, I. S. Aranson, L. S. Tsimring, *et al.*, "Effects of cross-links on motor-mediated filament organization," *New J. Phys.*, vol. 9, p. 421, 2007.

Chapter 3

Sliding and clustering of microtubules

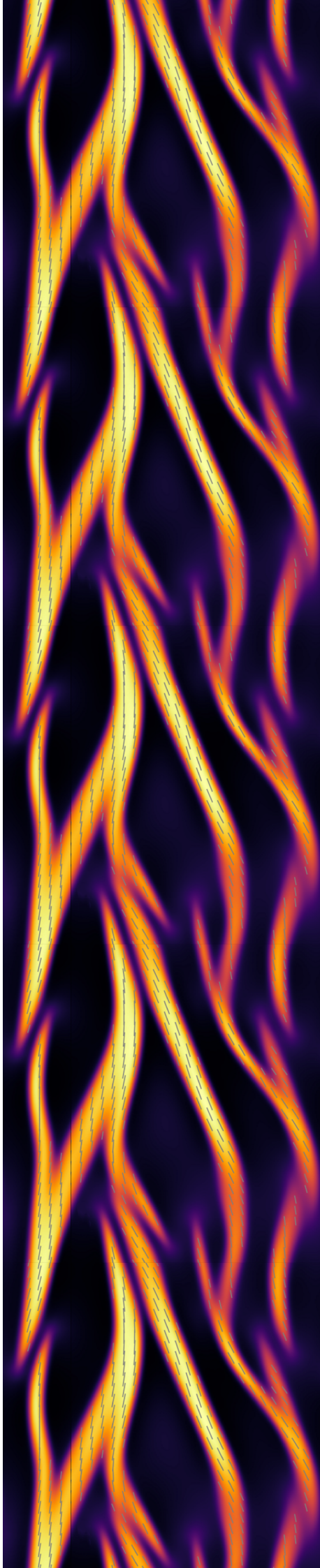

Abstract

In this Chapter we study the dynamics and phase behaviour of a dry suspension of microtubules and plus-directed sliding/clustering molecular motors. We obtain a set of continuum equations by rigorously coarse-graining a microscopic model where motor-induced interactions lead to parallel or antiparallel ordering. Through numerical solutions, we show that this model generically creates either stable stripes, or a never-settling pattern where stripes periodically form, rotate and then split up. We derive a minimal model which displays the same instability as the full model, and clarifies the underlying physical mechanism. The necessary ingredients are an extensile flux arising from microtubule sliding and an interfacial torque favouring ordering along density gradients.

3.1 Kinetic model of sliding and clustering MTs

As it was described in the introduction, the kinesin motors can provide both clustering of parallel MT filaments and sliding of antiparallel ones. In this Chapter, we use the kinetic model defined in Chapter 2 and study the dynamics of pattern formation in two-dimensional solutions of microtubules and plus-directed sliding/clustering molecular motors inducing both interaction types, whereas the previous Chapter was solely focused on the case of clustering.

MT-MM mixtures are relevant to both biological and synthetic instances of active matter. On the one hand, they incorporate the essential ingredients of the mitotic spindle [1–3], on the other hand, they closely mirror the so-called "hierarchical active matter", which can be self-assembled in the lab from MTs and MMs [4–6]. Sliding of antiparallel MTs plays important role in both mentioned cases.

Specifically, in this Chapter we consider the following sliding/clustering interaction rule: if the initial relative angle between rods exceeds $\pi/2$ then MTs first align in an anti-parallel way and then slide apart; otherwise, MTs cluster to acquire the same position and orientation (Fig. 3.1 a).

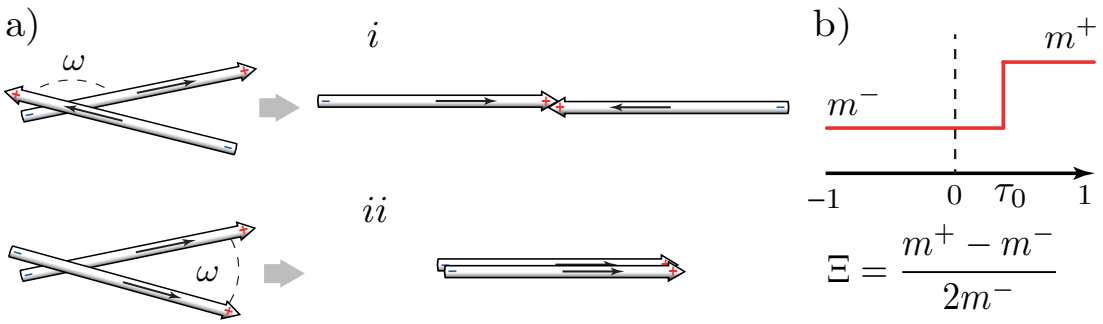

Figure 3.1: (a) Collision rule including MT sliding (*i*) and MT clustering (*ii*), according to the incidence angle. (b) Steady-state motor distribution considered in the anisotropic case (with inhomogeneous MT coverage by plus-directed motors).

Again within our model, MTs are covered by a steady-state static distribution of motors. Motor coverage may either be homogeneous or inhomogeneous [7, 8], and is parametrised by two geometrical quantities: $\Xi = \frac{m^+ - m^-}{2m^-}$, and τ_0 (Fig. 3.1 b) introduced previously. In what follows, we work in two-dimensional Cartesian coordinates.

Assuming that motor-induced rearrangements of MTs are fast with respect to diffusion, we treat them as instantaneous collisions and start our model from the following Boltzmann-like kinetic equation.

3.2 Kinetic Equation

The probability distribution function, $P(\mathbf{r}, \phi, t)$, for a MT to be at a position $\mathbf{r}$ with an orientation $\mathbf{n} = (\cos\phi, \sin\phi)$, given by the angle ϕ, at the time t obeys the following Boltzmann-like kinetic equation (for the sake of brevity we omit the time dependence in the following notations):

$$\partial_t P(\mathbf{r}, \phi) = D_r \partial_\phi^2 P(\mathbf{r}, \phi) + \nabla_i D_{ij} \nabla_j P(\mathbf{r}, \phi) + I_{int}(\mathbf{r}, \phi). \tag{3.1}$$

The first two terms on the r.h.s. of Eq. (3.1) represent contributions from diffusion, where D_r is the rotational diffusion coefficient and D_{ij} are components of the translational diffusion tensor [9, 10]. The last term is the interaction integral that encodes our collision rules between MTs, and includes clustering and sliding, see Figure 3.1 a. Note, that this time we do not consider excluded volume contribution.

3.2.1 Interaction Integral

Interaction integral corresponding to the collision rules depicted in Fig. 3.1 has the following form:

$$\begin{aligned}
\int d\boldsymbol{\xi} \Bigg[& \int_{-\frac{\pi}{2}}^{\frac{\pi}{2}} d\omega W\left(\mathbf{r}_1, \phi_2; \mathbf{r}_2, \phi_2\right) P\left(\mathbf{r}_1, \phi_1\right) P\left(\mathbf{r}_2, \phi_2\right) \\
& + \int_{\pi/2}^{3\pi/2} d\omega W\left(\mathbf{r}_1 + \frac{\eta L \mathbf{n}}{2}, \phi_1 + \frac{\pi}{2}; \mathbf{r}_2 + \frac{\eta L \mathbf{n}}{2}, \phi_2 + \frac{\pi}{2}\right) \\
& \times P\left(\mathbf{r}_1 + \frac{\eta L \mathbf{n}}{2}, \phi_1 + \frac{\pi}{2}\right) P\left(\mathbf{r}_2 + \frac{\eta L \mathbf{n}}{2}, \phi_2 + \frac{\pi}{2}\right) \Bigg] \\
- \int d\boldsymbol{\xi} & \int_{-\pi}^{\pi} d\omega W(\mathbf{r}, \phi; \mathbf{r} - \boldsymbol{\xi}, \phi - \omega) P\left(\mathbf{r}, \phi\right) P\left(\mathbf{r} - \boldsymbol{\xi}, \phi - \omega\right).
\end{aligned} \tag{3.2}$$

In the above we use notations for positions $\mathbf{r}_1 = \mathbf{r} - \frac{\boldsymbol{\xi}}{2}$and $\mathbf{r}_2 = \mathbf{r} + \frac{\boldsymbol{\xi}}{2}$, and orientations $\phi_1 = \phi - \frac{\omega}{2}$, and $\phi_2 = \phi + \frac{\omega}{2}$. Here $\boldsymbol{\xi}$ is a separation vector between MTs, ω is angle between MTs before the interaction, and parameter η determines the final relative displacement of MTs after sliding – henceforth we consider $\eta = 1$, corresponding to the full separation.

The first integral in Eq. 3.2 is a gain (or source) term, which in turn consist of two parts. First part describes polar clustering, the only distinction from the analogous term in Eq. 2.2 is the limits of integration. The second one encodes active separation of MTs.

The second integral in Eq. 3.2 is a loss (sink) term, describing the process by which a MT with the position $\mathbf{r}$ and orientation ϕ leaves that point of phase

space due to a motor-induced interaction with another MT. We denote the rate of the motor-induced processes as W.

3.2.2 Interaction kernel

The interaction functions W determine the rates at which two microtubules at $(\mathbf{r}_1, \phi_1)$ and $(\mathbf{r}_2, \phi_2)$ are displaced and reoriented by molecular motors. We use exact form of the interaction rate function introduced in the previous Chapter:

$$W(\mathbf{r}_1, \phi_1; \mathbf{r}_2, \phi_2) = G \underbrace{\Theta\big(1 - |\tau_1|\big)\Theta\big(1 - |\tau_2|\big)}_{\text{probability of intersection}} \underbrace{\big\{1 + \Xi\big[\Theta(\tau_1 - \tau_0) + \Theta(\tau_2 - \tau_0)\big]\big\}}_{\text{dependence on the local MM density}}. \tag{3.3}$$

The constant G is proportional to the motor properties, and will be eventually removed from the model by rescaling. The product of the Heaviside functions gives the geometric probability of two MT intersecting in 2D: since we assume MMs to be rods of negligible thickness, $\tau_{1,2}$ are the positions of the intersection point along the two MTs. We parametrise these position such that $\tau = 0$ at the MT centre and $\tau = \pm 1$ corresponds to the "+"/"−"-ends, respectively. The derivation of Eq. (3.3) is provided in the previous Chapter.

Eq. (3.3) can be written in terms of ξ, ψ, ϕ, and ω as

$$\begin{aligned} W(\mathbf{r}_1, \phi_1; \mathbf{r}_2, \phi_2) = G\,\Theta\left(|\sin\omega| - \frac{2\xi}{L}|\phi_1 - \psi|\right)\Theta\left(|\sin\omega| - \frac{2\xi}{L}|\phi_2 - \psi|\right) \\ \times\left\{1 + \Xi\left[\Theta\left(\frac{2\xi}{L}\frac{\sin(\phi_1 - \psi)}{\sin\omega} - \tau_0\right) + \Theta\left(\frac{2\xi}{L}\frac{\sin(\phi_2 - \psi)}{\sin\omega} - \tau_0\right)\right]\right\}, \end{aligned} \tag{3.4}$$

where $\boldsymbol{\xi} = \xi(\cos\psi, \sin\psi) = \mathbf{r}_2 - \mathbf{r}_1$ is the separation vector between MT centres, and $\omega = \phi_2 - \phi_1$ is the angle between their orientations; L is the MT length.

For the sake of brevity, we introduce the following notations, which are used in the next section and in the Appendix B:

$$\begin{aligned} W_1 &\equiv W\left(\mathbf{r} - \frac{\boldsymbol{\xi}}{2}, \phi - \frac{\omega}{2}; \mathbf{r} + \frac{\boldsymbol{\xi}}{2}, \phi + \frac{\omega}{2}\right), \\ \hat{W}_1 &\equiv W\left(\mathbf{r} - \frac{\boldsymbol{\xi}}{2} + \frac{\eta L\mathbf{n}}{2}, \phi - \frac{\omega}{2} + \frac{\pi}{2}; \mathbf{r} + \frac{\boldsymbol{\xi}}{2} + \frac{\eta L\mathbf{n}}{2}, \phi + \frac{\omega}{2} + \frac{\pi}{2}\right), \\ W_2 &\equiv W(\mathbf{r}, \phi; \mathbf{r} - \boldsymbol{\xi}, \phi - \omega). \end{aligned} \tag{3.5}$$

3.3 Long-wavelength expansion

Following the kinetic model introduced previously we expand P in Fourier harmonics. We also perform a gradient expansion, however this time we keep

terms up to second order.

Projecting the resulting equation on the s-th Fourier harmonic yields the following equation:

$$\begin{aligned}
\partial_t P_s(\mathbf{r}) &= -s^2 D_r P_s(\mathbf{r}) + \overline{\nabla_i D_{ij} \nabla_j P(\mathbf{r},\phi)}^s \\
&+ \sum_{n,m=-\infty}^{\infty} \left[\overline{I^{(0)}_{nm}}^s P_n P_m + \frac{1}{2} \overline{I^{(1)}_{i,nm}}^s A_{i,nm} + \frac{1}{8} \overline{I^{(2)}_{ij,nm}}^s A_{ij,nm} + \cdots \right] \\
&+ \sum_{n,m=-\infty}^{\infty} \left[\overline{\tilde{I}^{(0)}_{nm}}^s P_n P_m + \frac{1}{2} \overline{\tilde{I}^{(1)}_{i,nm}}^s A_{i,nm} + \frac{1}{2} \eta L \overline{K^{(1)}_{i,nm}}^s B_{i,nm} + \frac{1}{8} \overline{\tilde{I}^{(2)}_{ij,nm}}^s A_{ij,nm} \right. \\
&\qquad \left. + \frac{1}{8} \eta^2 L^2 \overline{K^{(2)}_{ij,nm}}^s B_{ij,nm} + \frac{1}{4} \eta L \overline{F^{(2)}_{ij,nm}}^s C_{ij,nm} + \cdots \right] \\
&- \sum_{n,m=-\infty}^{\infty} P_n \left[\overline{J^{(0)}_{nm}}^s P_m - \overline{J^{(1)}_{i,nm}}^s \nabla_i P_m + \frac{1}{2} \overline{J^{(2)}_{ij,nm}}^s \nabla_i \nabla_j P_m + \cdots \right],
\end{aligned} \tag{3.6}$$

where overline denotes the projection onto the s-th Fourier mode

$$\overline{(\dots)}^s = \frac{1}{2\pi} \int_0^{2\pi} e^{-is\phi} (\dots), \tag{3.7}$$

and we introduce the following notation for expressions containing Fourier harmonics P_n's and P_m's and corresponding space derivatives:

$$\begin{aligned}
A_{i,nm} &= P_n \nabla_i P_m - P_m \nabla_i P_n, \\
A_{ij,nm} &= P_n \nabla_i \nabla_j P_m - 2 (\nabla_i P_n) (\nabla_j P_m) + P_m \nabla_i \nabla_j P_n, \\
B_{i,nm} &= P_n \nabla_i P_m + P_m \nabla_i P_n, \\
B_{ij,nm} &= P_n \nabla_i \nabla_j P_m + 2 (\nabla_i P_n) (\nabla_j P_m) + P_m \nabla_i \nabla_j P_n, \\
C_{ij,nm} &= P_n \nabla_i \nabla_j P_m - P_m \nabla_i \nabla_j P_n + (\nabla_i P_n) (\nabla_j P_m) - (\nabla_i P_m) (\nabla_j P_n).
\end{aligned} \tag{3.8}$$

In Eqs. 3.8 all Fourier harmonics P_n's and P_m's are functions of $\mathbf{r}$ and t.

The interaction integrals used in the long wave expansions Eq. 3.6 are given by

$$\begin{aligned}
I^{(0)}_{nm} &= e^{i(n+m)\phi} \int d\boldsymbol{\xi} \int_{-\pi/2}^{\pi/2} d\omega \, W_1 e^{i(m-n)\frac{\omega}{2}}, \\
I^{(1)}_{i,nm} &= e^{i(n+m)\phi} \int d\boldsymbol{\xi} \int_{-\pi/2}^{\pi/2} d\omega \, W_1 e^{i(m-n)\frac{\omega}{2}} \xi_i, \\
I^{(2)}_{ij,nm} &= e^{i(n+m)\phi} \int d\boldsymbol{\xi} \int_{-\pi/2}^{\pi/2} d\omega \, W_1 e^{i(m-n)\frac{\omega}{2}} \xi_i \xi_j.
\end{aligned} \tag{3.9}$$

$$\tilde{I}^{(0)}_{nm} = e^{i(n+m)\phi} \int d\boldsymbol{\xi} \int_{\pi/2}^{3\pi/2} d\omega\, \tilde{W}_1 e^{i(m-n)\frac{\omega}{2}} e^{i(m+n)\frac{\pi}{2}},$$
$$\tilde{I}^{(1)}_{i,nm} = e^{i(n+m)\phi} \int d\boldsymbol{\xi} \int_{\pi/2}^{3\pi/2} d\omega\, \tilde{W}_1 e^{i(m-n)\frac{\omega}{2}} e^{i(m+n)\frac{\pi}{2}} \xi_i,$$
$$\tilde{I}^{(2)}_{ij,nm} = e^{i(n+m)\phi} \int d\boldsymbol{\xi} \int_{\pi/2}^{3\pi/2} d\omega\, \tilde{W}_1 e^{i(m-n)\frac{\omega}{2}} e^{i(m+n)\frac{\pi}{2}} \xi_i \xi_j. \tag{3.10}$$

$$K^{(1)}_{i,nm} = e^{i(n+m)\phi} \int d\boldsymbol{\xi} \int_{\pi/2}^{3\pi/2} d\omega\, \tilde{W}_1 e^{i(m-n)\frac{\omega}{2}} e^{i(m+n)\frac{\pi}{2}} n_i,$$
$$K^{(2)}_{ij,nm} = e^{i(n+m)\phi} \int d\boldsymbol{\xi} \int_{\pi/2}^{3\pi/2} d\omega\, \tilde{W}_1 e^{i(m-n)\frac{\omega}{2}} e^{i(m+n)\frac{\pi}{2}} n_i n_j,$$
$$F^{(2)}_{ij,nm} = e^{i(n+m)\phi} \int d\boldsymbol{\xi} \int_{\pi/2}^{3\pi/2} d\omega\, \tilde{W}_1 e^{i(m-n)\frac{\omega}{2}} e^{i(m+n)\frac{\pi}{2}} n_i \xi_j. \tag{3.11}$$

$$J^{(0)}_{nm} = e^{i(n+m)\phi} \int d\boldsymbol{\xi} \int_{-\pi}^{\pi} d\omega\, W_2 e^{-im\omega},$$
$$J^{(1)}_{i,nm} = e^{i(n+m)\phi} \int d\boldsymbol{\xi} \int_{-\pi}^{\pi} d\omega\, W_2 e^{-im\omega} \xi_i,$$
$$J^{(2)}_{ij,nm} = e^{i(n+m)\phi} \int d\boldsymbol{\xi} \int_{-\pi}^{\pi} d\omega\, W_2 e^{-im\omega} \xi_i \xi_j. \tag{3.12}$$

Where ξ_i and n_i are the Cartesian components of the vectors $\boldsymbol{\xi}$ and $\mathbf{n}$.

3.4 Evaluation of interaction integrals

Consider contribution to the s-th Fourier mode from the motor-induced interactions. It can be represented as a sum of six members, each of which collects terms of the same order of ξ and n:

$$T^{(1)}_{nm} + T^{(2)}_{i,nm} + T^{(3)}_{ij,nm} + T^{(4)}_{i,nm} + T^{(5)}_{ij,nm} + T^{(6)}_{ij,nm}. \tag{3.13}$$

Particularly:

$$\begin{aligned} T^{(1)}_{nm} &\propto \xi^0 n^0 \\ T^{(2)}_{i,nm} &\propto \xi^1 n^0 \\ T^{(3)}_{ij,nm} &\propto \xi^2 n^0 \\ T^{(4)}_{i,nm} &\propto \xi^0 n^1 \\ T^{(5)}_{ij,nm} &\propto \xi^0 n^2 \\ T^{(6)}_{ij,nm} &\propto \xi^1 n^1. \end{aligned} \tag{3.14}$$

Below we provide an exact expressions corresponding to each term:

$$
\begin{aligned}
T^{(1)}_{nm} &= \sum_{n,m=-\infty}^{\infty} \left[\overline{I^{(0)}_{nm}}^{s} P_n P_m + \overline{\tilde{I}^{(0)}_{nm}}^{s} P_n P_m - \overline{J^{(0)}_{nm}}^{s} P_m \right], \\
T^{(2)}_{i,nm} &= \sum_{n,m=-\infty}^{\infty} \left[\frac{1}{2} \overline{I^{(1)}_{i,nm}}^{s} A_{i,nm} + \frac{1}{2} \overline{\tilde{I}^{(1)}_{i,nm}}^{s} A_{i,nm} + \overline{J^{(1)}_{i,nm}}^{s} P_n \nabla_i P_m \right], \\
T^{(3)}_{ij,nm} &= \sum_{n,m=-\infty}^{\infty} \left[\frac{1}{8} \overline{I^{(2)}_{ij,nm}}^{s} A_{ij,nm} + \frac{1}{8} \overline{\tilde{I}^{(2)}_{ij,nm}}^{s} A_{ij,nm} - \frac{1}{2} \overline{J^{(2)}_{ij,nm}}^{s} P_n \nabla_i \nabla_j P_m \right], \\
T^{(4)}_{i,nm} &= \sum_{n,m=-\infty}^{\infty} \left[\frac{1}{2} \eta L \overline{K^{(1)}_{i,nm}}^{s} B_{i,nm} \right], \\
T^{(5)}_{ij,nm} &= \sum_{n,m=-\infty}^{\infty} \left[\frac{1}{8} \eta^2 L^2 \overline{K^{(2)}_{ij,nm}}^{s} B_{ij,nm} \right], \\
T^{(6)}_{ij,nm} &= \sum_{n,m=-\infty}^{\infty} \left[\frac{1}{4} \eta L \overline{F^{(2)}_{ij,nm}}^{s} C_{ij,nm} \right].
\end{aligned} \tag{3.15}
$$

Evaluation of these integrals is performed using the semi-numeric technique presented in the Section 2.4 of the previous Chapter. Details of calculations and corresponding tables are provided in Appendix B.

3.5 Results

3.5.1 Full Model

Hydrodynamic equations

We proceed by applying a rigorous coarse-graining procedure developed in the previous Chapter to Eq. (3.6) to derive a system of mean-field equations for the following fields: (i) the density of filaments ρ, (ii) their mean orientation p_i, and (iii) a tensorial field Q_{ij} quantifying the nematic (apolar) ordering of MTs.

These variables are defined as the first three moments of probability distrubution function $P(\mathbf{r}, \phi)$:

$$
\begin{aligned}
\rho(\mathbf{r}) &= \int_0^{2\pi} P(\mathbf{r}, \phi) d\phi, \\
p_i(\mathbf{r}) &= \frac{1}{2\pi} \int_0^{2\pi} n_i \, P(\mathbf{r}, \phi) d\phi, \\
Q_{ij}(\mathbf{r}) &= \frac{1}{\pi} \int_0^{2\pi} \left(n_i n_j - \frac{1}{2} \delta_{ij} \right) P(\mathbf{r}, \phi) d\phi,
\end{aligned} \tag{3.16}
$$

again $\mathbf{n} = n_i = (\cos\phi, \sin\phi)$. As it was mentioned, the hydrodynamic variables

can be expressed in terms of the Fourier harmonics:

$$\begin{aligned}
\rho(\mathbf{r}) =& 2\pi P_0(\mathbf{r}),\\
p_x(\mathbf{r}) =& \frac{P_{-1}(\mathbf{r}) + P_1(\mathbf{r})}{2},\\
p_y(\mathbf{r}) =& \frac{P_{-1}(\mathbf{r}) - P_1(\mathbf{r})}{2i},\\
Q_{xx}(\mathbf{r}) =& \frac{P_2(\mathbf{r}) + P_{-2}(\mathbf{r})}{2},\\
Q_{xy}(\mathbf{r}) =& \frac{P_{-2}(\mathbf{r}) - P_2(\mathbf{r})}{2i}.
\end{aligned} \tag{3.17}$$

So in Eq. (3.6), we keep the first Fourier harmonics, P_0, $P_{\pm1}$, and $P_{\pm2}$; we also keep harmonics $P_{\pm3}$ and $P_{\pm4}$ but drop any gradient of them. For the 3d and 4th Fourier harmonics, Eq. (3.6) is an algebraic equation that is solved by $P_3 = A_3 P_1 P_2$ and $P_4 = A_4 P_2^2$. Note, that following the logic described in [11, 12] we also keep the 4th power of gradients for the Fourier harmonic P_0; it eventually provides the biharmonic operator in the density equation.

To make equations dimensionless we rescale time, space and the Fourier harmonics of P by D_r^{-1}, L and GL^2/D_r, respectively.

The final set of equations, which we refer to as the "full model" in this Chapter, is provided below. These equations can be written in a more compact form in terms of complex fields and the Wirtinger derivatives $\underline{\nabla} = \partial_x + i\partial_y$ and $\underline{\nabla}^* = \partial_x - i\partial_y$, where * denotes complex conjugation. However, we find the resulting equations more difficult to read and prefer to keep the standard notation ($\partial_i = \partial/\partial_{x_i}$), the indices refer to the two-dimensional Cartesian components and the Einstein summation convention is employed; we use standard symbol for the laplacian $\nabla^2 = \partial_k\partial_k$, and we introduce the following operator $\mathcal{D}_{ij} = \partial_i\partial_j - \frac{\delta_{ij}}{2}\partial_k\partial_k$.

$$\begin{aligned}
\partial_t\rho =& \frac{1}{32}\nabla^2\rho + \frac{\pi}{48}\partial_i\partial_j Q_{ij}\\
&+ (1+a_3)\,\frac{\pi}{4}\left[-\frac{1}{12\pi^2}\nabla^2\rho^2 + \frac{1}{9}\nabla^2 Q_{ij}Q_{ij} - \frac{1}{9\pi}\partial_i\partial_j(\rho Q_{ij})\right]\\
&+ (1+a_1)\,\frac{\eta^2\pi}{4}\left[\frac{1}{4\pi^2}\nabla^2\rho^2 - \frac{1}{3}\nabla^2 Q_{ij}Q_{ij} + \frac{1}{2\pi}\partial_i\partial_j(\rho Q_{ij}) - 2\partial_i\partial_j\left(p_i p_j\right)\right]\\
&- \frac{91}{69120\pi}\rho_0\nabla^4\rho,
\end{aligned} \tag{3.18}$$

$$
\begin{aligned}
\partial_t p_i = &-p_i + \frac{5}{192}\nabla^2 p_i + \frac{1}{96}\partial_i(\partial_k p_k) + (1+a_1)\left[-\frac{3}{11\pi}\rho p_i + \frac{29}{19}Q_{ij}p_j - \frac{7}{18}A_3 Q_{kl}Q_{kl}p_i\right] \\
&+ a_2\frac{1}{8}\Bigg[-\frac{1}{4\pi^2}\partial_i\rho^2 + \left(3p_i(\partial_k p_k) + (p_k\partial_k)p_i - \frac{1}{3}\partial_i(p_k p_k)\right) \\
&\qquad - \left(\frac{1}{12\pi}\partial_j(\rho Q_{ij}) + \frac{1}{2\pi}Q_{ij}\partial_j\rho\right) + \frac{113}{180}\partial_i(Q_{kl}Q_{kl}) - \frac{53}{45}Q_{ij}\partial_k Q_{jk}\Bigg] \\
&+ (1+a_3)\frac{1}{720}\Bigg[-\frac{31}{\pi}p_i\nabla^2\rho - \frac{6}{\pi}p_k\partial_k\partial_i\rho + \frac{19}{\pi}\left(\rho\nabla^2 p_i - \frac{1}{2}\nabla^2(\rho p_i)\right) \\
&\qquad - \frac{7}{\pi}\left((\partial_i\rho)(\partial_k p_k) - \rho\partial_i(\partial_k p_k) + \partial_i(p_k\partial_k\rho)\right) - 61 p_i\partial_k\partial_l Q_{kl} \\
&\qquad + 49(p_k\partial_k)(\partial_j Q_{ij}) + 31 p_k\partial_i\partial_l Q_{kl} + 10 Q_{kl}\partial_i\partial_k p_l + 28 Q_{il}\partial_l(\partial_k p_k) \\
&\qquad - 19 Q_{ik}\nabla^2 p_k - 14\partial_k\partial_l(Q_{kl}p_i) + 9\partial_i\partial_k(Q_{kl}p_l) - \frac{9}{2}\nabla^2(Q_{ij}p_j)\Bigg] \\
&+ (1+a_1)\frac{\eta}{2}\left[\frac{1}{4\pi^2}\nabla\rho^2 + \frac{1}{2\pi}\partial_j(\rho Q_{ij}) - \frac{1}{3}\partial_i Q_{kl}Q_{kl} - 2\partial_j(p_i p_j)\right] \\
&+ a_2\frac{\eta}{44}\Bigg[\frac{9}{8\pi}\left(2(p_k\partial_k)\partial_i\rho - 2\rho\partial_i(\partial_k p_k) - \rho\nabla^2 p_i + p_i\nabla^2\rho\right) + 2p_i\partial_k\partial_l Q_{kl} \\
&- 2Q_{kl}\partial_k\partial_l p_i + \frac{5}{2}((p_k\partial_k)(\partial_j Q_{ij}) - Q_{il}\partial_l(\partial_k p_k)) + \frac{3}{2}(Q_{kl}\partial_i\partial_k p_l - p_k\partial_i\partial_l Q_{kl})\Bigg],
\end{aligned}
\tag{3.19}
$$

$$
\begin{aligned}
\partial_t Q_{ij} = &-4Q_{ij} + \frac{1}{32}\nabla^2 Q_{ij} + \frac{1}{192\pi}\mathcal{D}_{ij}\rho + (1+a_1)\left[\frac{2}{3\pi}\rho Q_{ij} - A_4\frac{6}{5}(Q_{kl}Q_{kl})Q_{ij}\right] \\
&+ a_2\Bigg[-\frac{1}{16\pi}\left(\partial_i(\rho p_j) + \partial_j(\rho p_i) - \delta_{ij}\partial_k(\rho p_k)\right) - \frac{\rho}{24\pi}\left(\partial_i p_j + \partial_j p_i - \delta_{ij}(\partial_k p_k)\right) \\
&\qquad + \frac{1}{4}Q_{ij}(\partial_k p_k) + \frac{5}{12}(p_k\partial_k)Q_{ij}\Bigg] \\
&+ (1+a_3)\frac{1}{8}\Bigg[-\frac{1}{36\pi^2}\left(3\left[(\partial_i\rho)(\partial_j\rho) - \frac{\delta_{ij}}{2}(\partial_k\rho)^2\right] + \rho\mathcal{D}_{ij}\rho\right) + \frac{5}{9\pi}\rho\nabla^2 Q_{ij} \\
&\qquad - \frac{1}{3\pi}Q_{ij}\nabla^2\rho - \frac{1}{6\pi}\nabla^2(\rho Q_{ij}) - \frac{11}{45}Q_{ij}\partial_k\partial_l Q_{kl} - \frac{1}{6}\partial_k\partial_l(Q_{ij}Q_{kl}) \\
&\qquad + \frac{7}{15}Q_{kl}\partial_k\partial_l Q_{ij} + \frac{1}{12}\mathcal{D}_{ij}(Q_{kl}Q_{kl}) - \frac{1}{5}Q_{kl}\mathcal{D}_{ij}Q_{kl}\Bigg] \\
&+ (1+a_1)\frac{\eta^2}{8}\Bigg[\frac{1}{4\pi^2}\mathcal{D}_{ij}\rho^2 - \partial_i\partial_j(p_k p_k) - 2\nabla^2(p_i p_j) \\
&\qquad - \frac{5}{6}\mathcal{D}_{ij}(Q_{kl}Q_{kl}) + \partial_k\partial_l(Q_{kl}Q_{ij}) + \frac{1}{2\pi}\nabla^2(\rho Q_{ij})\Bigg].
\end{aligned}
\tag{3.20}
$$

Coefficients A_3 and A_4 are coming from the adiabatic elimination of higher Fourier modes of $P(\mathbf{r},\phi)$, Their expressions are given by:

$$
A_4 = 3\left(\frac{1}{1+a_1} + \frac{\rho_0}{5\pi}\right)^{-1}, \qquad A_3 = \left(\frac{15}{8}\frac{1}{1+a_1} + \frac{19\rho_0}{48\pi}\right)^{-1}. \tag{3.21}
$$

We also use the following anisotropy functions that depend on Ξ and τ_0 and vanish if $\Xi = 0$ or $\tau_0 = \pm 1$:

$$\begin{aligned} a_1 =& \Xi\left(1-\tau_0\right), \\ a_2 =& \Xi\left(1-\tau_0^2\right), \\ a_3 =& \Xi\left(1-\tau_0\left(1+\tau_0^2\right)/2\right). \end{aligned} \tag{3.22}$$

Linear stability analysis

We perform a linear stability analysis of the full model, Eqs. (3.18), (3.19) and (3.20). Firstly, we assume that the base state has a uniform density ρ_0 and there is no nematic or polar order. We introduce infinitesimal perturbations to the ρ field:

$$\begin{aligned} \rho(\mathbf{r},t) &= \rho_0 + \delta\rho e^{i\mathbf{k}\cdot\mathbf{r}} e^{\hat{\sigma}t}, \\ Q_{xx}(\mathbf{r},t) &= Q_{xy}(\mathbf{r},t) = 0, \end{aligned} \tag{3.23}$$

where k_x and k_y set the lengthscale of the perturbation, and $\hat{\sigma}$ is a temporal eigenvalue. A linear stability analysis shows that the uniform isotropic state is linearly unstable towards the emergence of a globally-ordered nematic state, when the initial density of MTs ρ_0 exceeds critical value (predicted phase diagram is provided in Figs. 3.2 and 3.3d):

$$\rho_0 > \rho_{cr} = \frac{6\pi}{(1+\Xi(1-\tau_0))} = \frac{6\pi}{(1+a_1)}. \tag{3.24}$$

Investigating the dispersion curve corresponding to this instability we observe that it has a long wavelength ($k = 0$).

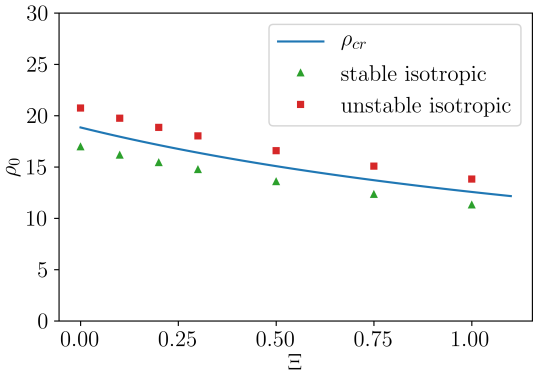

Figure 3.2: Liner stability of the full model. Stability of the homogeneous isotropic state, green triangles and red squares represent stable and unstable solutions obtained in the numerical solutions.

Additionally, stability analysis of the homogeneous nematic state ($Q_{xx}(\mathbf{r},t) = Q_0$, $Q_{xy}(\mathbf{r},t) = 0$) demonstrates that this state is itself unstable; however, it be-

comes stable again at very high density. This analysis contains cumbersome equations and is not provided in the text.

Numerical solutions

To study the dynamics predicted by the full model Eq. (3.18), we solve equations numerically and discuss representative results below. We discretise spatial derivatives by second-order finite-differences and use a second-order predictor-corrector method integrating over time. Our computations are performed on square domains 150×150 or 50×50 with periodic boundary conditions. Spatial resolution $\Delta h = 0.5$, the unit length is chosen to be the microtubular length the timestep is set to $t = 0.005$. Unless explicitly stated, simulations are initialised from an isotropic uniform MT suspension with an overall density ρ_0 and a small amount of noise.

We present our simulation results in composite images showing simultaneously the local density profile $\rho(\mathbf{r})$ (colour), orientation vector field $p_i(\mathbf{r})$ (black arrows), and tensorial nematic order Q_{ij} (grey segments). When we depict Q_{ij}, we plot the largest eigenvector normalised by the corresponding eigenvalue.

In accordance with the linear stability analysis, our simulations demonstrate that above the critical MT density ρ_{cr} uniform isotropic state becomes unstable with respect to small perturbation, and we observe the emergence of regions with a nematic state.

The latter instability leads to co-existence between high-density, nematically-ordered elongated domains and a low-density isotropic background (Fig. 3.3 a). The outcome of this phase separation at late times depends on the value of the anisotropy parameters, Ξ and τ_0; however, the latter plays a minor role. We observe that without the loss of generality we can set $\tau_0 = 0.5$, and vary only Ξ and ρ_0. For small Ξ, domains coarsen to leave a single static band (Fig. 3.3a), the minimal and maximal densities depend on the parameters. Inside the band, MTs are ordered nematically, with residual polar order confined at the interface with the isotropic phase.

For large enough Ξ, we instead observe an ever-evolving pattern (Fig. 3.3b). In this case, microtubular bands periodically form, self-extend, rotate, split up and disappear in the isotropic background. This behaviour is superficially reminiscent of "active turbulence" [13] in wet active gels. By analogy, call this spatiotemporal pattern observed in our model *dry active turbulence*.

We plot the time evolution of the domain size ℓ, computed via the first moment of the structure factor (Fig. 3.3f). First, we compute the structure factor, $S = \langle \rho(t, \mathbf{k}) \rho(t, -\mathbf{k}) \rangle$, by averaging the output of the simulation at late times. The typical length scale of the domain is inversely proportional to the average wave vector ($\ell = 2\pi / \langle k \rangle$), which can be calculated as the first moment of the structure factor:

$$\ell(t) = \frac{2\pi}{\langle k \rangle} = \frac{2\pi}{\frac{\int kS(\mathbf{k},t)d\mathbf{k}}{\int S(\mathbf{k},t)d\mathbf{k}}} = 2\pi \frac{\int S(\mathbf{k},t)d\mathbf{k}}{\int kS(\mathbf{k},t)d\mathbf{k}}, \tag{3.25}$$

where $k = |\mathbf{k}|$.

We also plot the Fourier transform of the domain size (Fig. 3.3h). It is apparent that there is a selected lengthscale in the isotropic case, while the dynamics in the anisotropic case appear to be chaotic (as the Fourier transform in Fig. 3.3h contains all frequencies). Our findings are summarised in the phase diagram in Figure 3.3d. As we discuss later an analogous dynamical pattern was observed at the level of kinetic theory for a very different physical system, a suspension of flocking self-propelled particles with nematic alignment.

To identify the fundamental mechanism leading to pattern formation in our system, we now search for a minimal model. The details of the minimal model construction are provided below.

3.5.2 Minimal model

We define the minimal model as a set of simple equations, which simultaneously satisfies two conditions. First, it needs to have qualitatively similar dynamics as the full model (Figs. 3.3a and b): it should retain both a transition between a uniform and a phase separated nematic state, as well as a regime with chaotic dynamics. In small domains, it should exhibit features similar to Figure 3.3c. Second, we require that the location of the phase boundaries in the minimal and full models (Figs. 3.3d and e), is quantitatively similar.

As a first step, we exploit the observation that polar order plays a minor role (Fig. 3.3c), and adiabatically eliminate p_i in favour of $\partial_i \rho$ and $\partial_j Q_{ij}$ Eq. (3.19).

If we introduce parameter $\epsilon \sim \rho_0 - \rho_{cr}$, balancing the terms in Eq. (3.20) implies that $Q_{ij} \sim \partial_t \sim \epsilon$, $p_i \sim \partial_t \sim \epsilon^2$. So we can rewrite Eq. (3.19) keeping only terms $\sim \epsilon^2$.

Then, we systematically switched off each term individually in the resulting equations, and computed the resulting phase diagram in each case. The term was reinstated only if it significantly changed the position of the phase

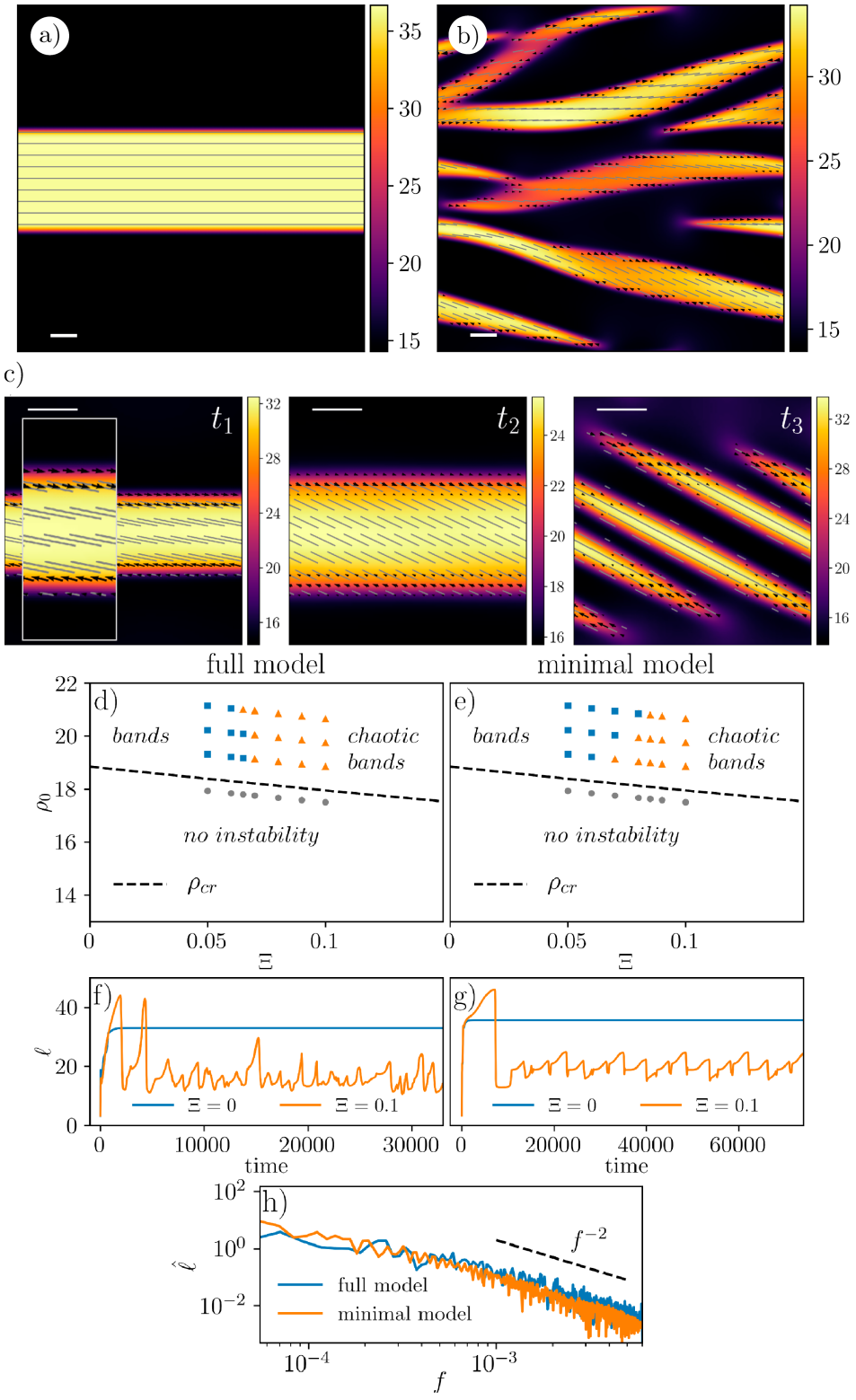

Figure 3.3: (A-c) Numerical solutions of the full model. (a) Formation of a stable band ($\Xi = 0, \rho_0 = 1.1\rho_{cr}$, 150×150). (b) Chaotic dynamics for $\Xi \neq 0$ ($\Xi = 0.1, \tau_0 = 0.5, \rho_0 = 1.1\rho_{cr}$, 150×150). (c) Same as (b), but for system size equal 50; snapshots $t_1 - t_2 - t_3$ show the evolution of a nematic band. In (a-c) colormaps represent the MT density, black arrows are for polar order field, and gray segments illustrate the largest eigenvector of the Q_{ij}-tensor. Scale bar: 10 L. (d,e) Phase diagram for the full (d) and minimal (e) model. (f,g) Domain size ℓ versus time for the full (f) and minimal (g) model. (h) Fourier transform of ℓ versus frequency.

boundary. Thus, we obtained the simplified version of our full field equations:

$$\partial_t\rho = \frac{1}{32}\nabla^2\rho + \frac{\pi}{48}\partial_i\partial_j Q_{ij} + \left(\frac{1+a_1}{16\pi}\eta^2 - \frac{1+a_3}{48\pi}\right)\nabla^2\rho^2 + \left(\frac{1+a_1}{8}\eta^2 - \frac{1+a_3}{36}\right)\partial_i\partial_j(\rho Q_{ij}) - \pi\left(\frac{1+a_1}{12}\eta^2 - \frac{1+a_3}{36}\right)\nabla^2\left(Q_{kl}Q_{kl}\right), \tag{3.26}$$

$$p_i = \frac{\rho_0}{1+(1+a_1)\frac{3}{11\pi}\rho_0}\left[\left(\frac{1+a_1}{4\pi^2}\eta - \frac{a_2}{16\pi^2}\right)\partial_i\rho + \left(\frac{1+a_1}{4\pi}\eta - \frac{a_2}{96\pi}\right)\partial_j Q_{ij}\right], \tag{3.27}$$

$$\begin{aligned}\partial_t Q_{ij} =& -4Q_{ij} + \frac{1}{32}\nabla^2 Q_{ij} + \frac{1}{192\pi}\mathcal{D}_{ij}\rho + (1+a_1)\left[\frac{2}{3\pi}\rho Q_{ij} - A_4\frac{6}{5}Q_{kl}Q_{kl}Q_{ij}\right] \\ &+ a_2\left[-\frac{1}{16\pi}\left(\partial_i(\rho p_j) + \partial_j(\rho p_i) - \delta_{ij}\partial_k\left(\rho p_k\right)\right) - \frac{1}{24\pi}\rho\left(\partial_i p_j + \partial_j p_i - \delta_{ij}(\partial_k p_k)\right)\right] \\ &+ (1+a_3)\frac{1}{8}\Bigg[-\frac{1}{36\pi^2}\Big(3\left[\partial_i\rho\partial_j\rho - \tfrac{\delta_{ij}}{2}\partial_k\rho\partial_k\rho\right] + \rho\mathcal{D}_{ij}\rho\Big) \\ &\qquad + \frac{5}{9\pi}\rho\nabla^2 Q_{ij} - \frac{1}{6\pi}\nabla^2(\rho Q_{ij}) + \frac{1}{12}\mathcal{D}_{ij}(Q_{kl}Q_{kl}) - \frac{1}{5}Q_{\alpha\beta}\mathcal{D}_{ij}Q_{\alpha\beta}\Bigg] \\ &+ (1+a_1)\frac{\eta^2}{8}\left[\frac{1}{4\pi^2}\mathcal{D}_{ij}\rho^2 - \frac{5}{6}\mathcal{D}_{ij}(Q_{kl}Q_{kl}) + \frac{1}{2\pi}\nabla^2(\rho Q_{ij})\right].\end{aligned} \tag{3.28}$$

where we again use the operator $\mathcal{D}_{ij} = \partial_i\partial_j - (1/2)\delta_{ij}\partial_k\partial_k$.

After that we put expression (3.27) for the polar order p_i into the simplified equation for nematic alignment tensor (3.28). And finally, we linearise density in Eq. (3.28) everywhere except the linear term, and obtain the following minimal model:

$$\partial_t\rho = \nabla^2\left[\frac{1}{32}\rho + \mu\rho^2\right] + \partial_i\partial_j\left[\frac{\pi}{48} + \chi\rho\right]Q_{ij} - \lambda\nabla^2\left(Q_{kl}Q_{kl}\right), \tag{3.29}$$

$$\begin{aligned}\partial_t Q_{ij} =& \left[4\left(\rho/\rho_{cr} - 1\right) - \alpha Q_{kl}Q_{kl} + \kappa\nabla^2\right]Q_{ij} + \zeta\mathcal{D}_{ij}\rho \\ &- \beta_1\mathcal{D}_{ij}\left(Q_{kl}Q_{kl}\right) - \beta_2 Q_{kl}\mathcal{D}_{ij}Q_{kl}.\end{aligned} \tag{3.30}$$

All eight parameters – μ, χ, λ, α, κ, ζ, β_1, β_2 – are essential to get quantitative agreement with the full model; their expressions in terms of the microscopic

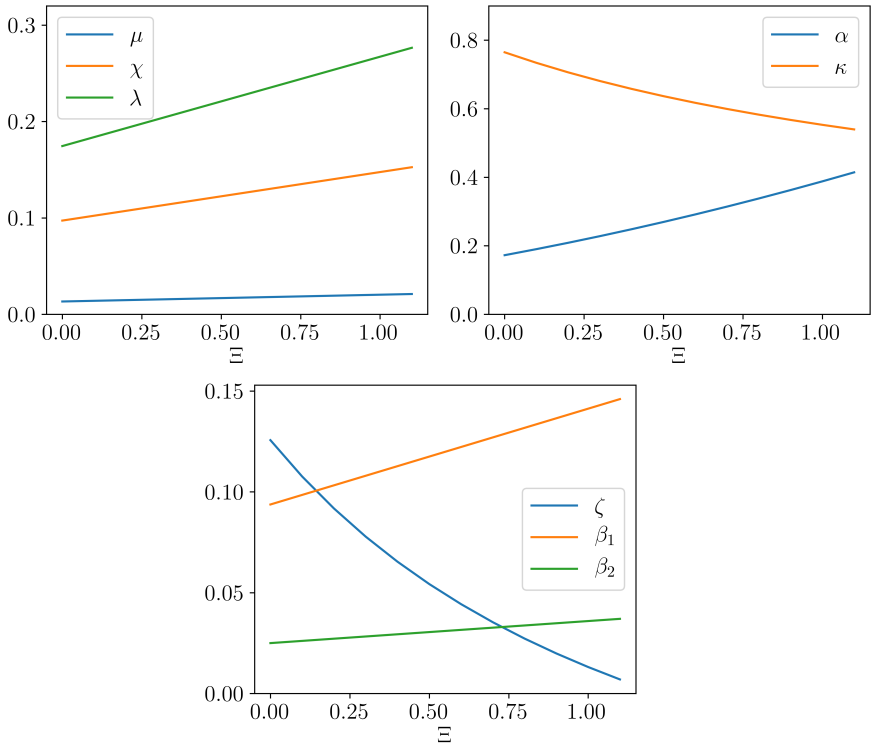

Figure 3.4: Dependence of the minimal model parameters on Ξ ($\rho_0 = 1.1\rho_{cr}, \tau_0 = 0.5$).

quantities ρ_0, Ξ, τ_0 and η are given as follows:

$$\mu = \frac{1+a_1}{16\pi}\eta^2 - \frac{1+a_3}{48\pi}, \quad \chi = \frac{1+a_1}{8}\eta^2 - \frac{1+a_3}{36}, \quad \lambda = \pi\left(\frac{1+a_1}{12}\eta^2 - \frac{1+a_3}{36}\right),$$
$$\kappa = \frac{1}{32} + \left(\frac{1+a_1}{16\pi}\eta^2 + \frac{7(1+a_3)}{144\pi}\right)\rho_0 - \frac{5a_2}{48\pi\left(1+(1+a_1)\frac{3}{11\pi}\rho_0\right)}\left(\frac{1+a_1}{4\pi}\eta - \frac{a_2}{96\pi}\right)\rho_0^2,$$
$$\zeta = \frac{1}{192\pi} + \left(\frac{1+a_1}{16\pi^2}\eta^2 - \frac{1+a_3}{288\pi^2}\right)\rho_0 - \frac{5a_2}{24\pi\left(1+(1+a_1)\frac{3}{11\pi}\rho_0\right)}\left(\frac{1+a_1}{4\pi^2}\eta - \frac{a_2}{16\pi^2}\right)\rho_0^2,$$
$$\beta_1 = \frac{1+a_3}{96} - \frac{5\eta^2(1+a_1)}{48}, \quad \beta_2 = -\frac{1+a_3}{40}, \qquad \rho_{cr} = \frac{6\pi}{1+a_1}, \quad \alpha = \frac{2(1+a_1)}{\frac{5}{1+a_1} + \frac{\rho_0}{\pi}}. \tag{3.31}$$

Within this set, ζ is the only parameter that can change sign – the others are always positive (Fig. 3.4).

Numerical solutions

Numerically simulating minimal model we use the same technique as for the full model. Since from the beginning we require the similarity between the

full and minimal model, it indeed reproduces main features including the formation of steady bands in case of small Ξ and chaotic bands for increased Ξ (Fig. 3.5 a).

The phase diagram corresponding to the minimal model is given in Figure 3.3e. It mirrors the transition between stable and unstable isotropic states (has the same ρ_{cr}), as well as a regime with chaotic dynamics; in small domains, it demonstrates features similar to Figure 3.3c, and the location of the phase boundaries in the minimal and full models (Figs. 3.3d and e) is similar .

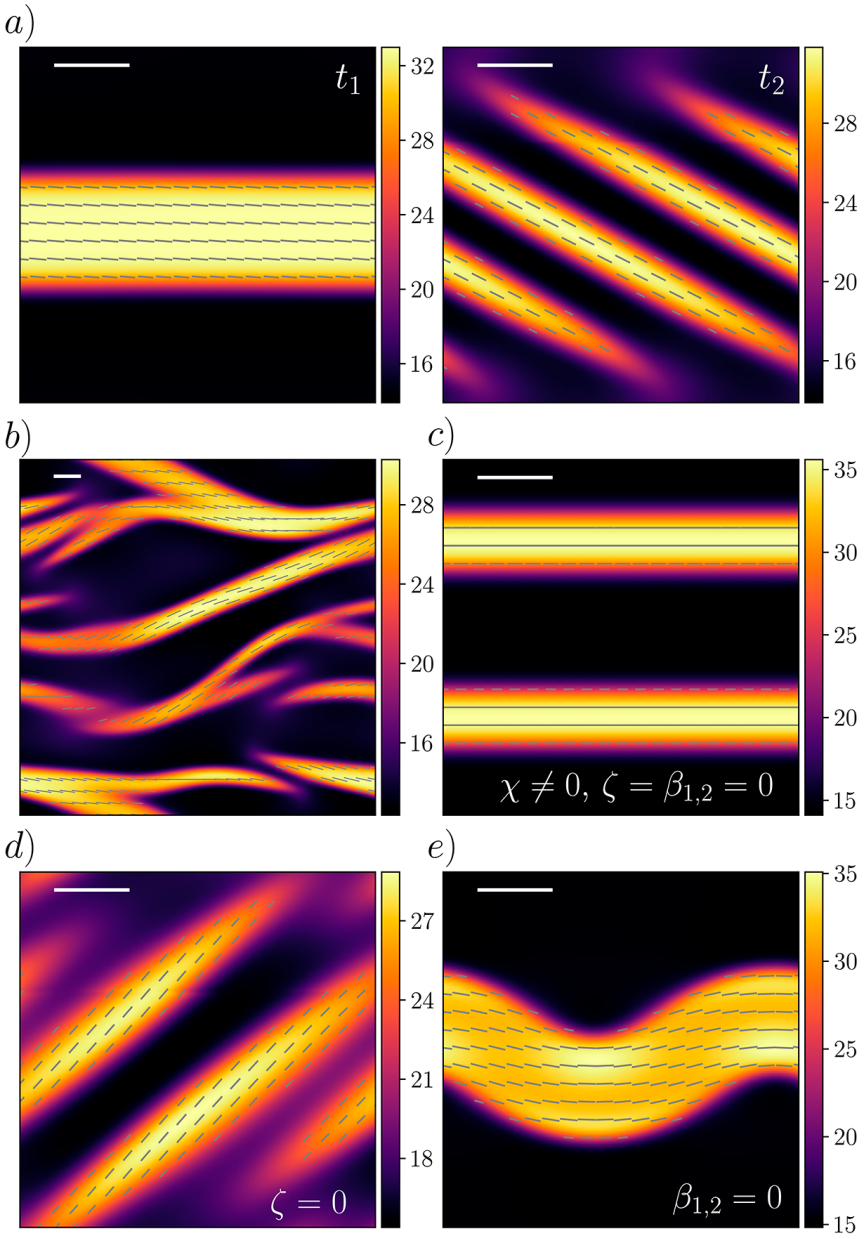

Figure 3.5: Pattern formation within the minimal model. (a) Chaotic dynamics similar to Figure 2b ($\Xi = 0.1, \tau_0 = 0.5$). (b) Chaotic dynamics for larger system size and anisotropy ($\Xi = 0.3, \tau_0 = 0.5$). (c) Non-equilibrium phase separation with $\beta_{1,2} = \zeta = 0$ ($\Xi = 0$). (d) Chaotic dynamics with $\zeta = 0$ ($\Xi = 0$). (e) Interfacial undulation and chaos with $\beta_{1,2} = 0$ ($\Xi = 0$). For all plots $\rho_0 = 1.1\rho_{cr}$, scale bar: $10\ L$.

Linear stability analysis

Here we perform a linear stability analysis of the minimal model, Eqs. (3.29) and (3.30). Without loss of generality, we assume that the base state has a uniform density ρ_0 and a uniform nematic order Q_0, oriented along the x-direction. We introduce infinitesimal perturbations to the ρ and Q_{ij} fields

$$\begin{aligned}\rho(\mathbf{r},t) &= \rho_0 + \delta\rho e^{i\mathbf{k}\cdot\mathbf{r}} e^{\hat{\sigma}t},\\ Q_{xx}(\mathbf{r},t) &= Q_0 + \delta Q_{xx} e^{i\mathbf{k}\cdot\mathbf{r}} e^{\hat{\sigma}t},\\ Q_{xy}(\mathbf{r},t) &= \delta Q_{xy} e^{i\mathbf{k}\cdot\mathbf{r}} e^{\hat{\sigma}t},\end{aligned} \tag{3.32}$$

where k_x and k_y set the lengthscale of the perturbation, and $\hat{\sigma}$ is a temporal eigenvalue. We substitute these expressions into Eqs. (3.29) and (3.30), and linearise the resulting equations with respect to the perturbations to obtain

$$\hat{\sigma}\begin{pmatrix}\delta\rho\\ \delta Q_{xx}\\ \delta Q_{xy}\end{pmatrix} = M\begin{pmatrix}\delta\rho\\ \delta Q_{xx}\\ \delta Q_{xy}\end{pmatrix}, \tag{3.33}$$

where matrix M is given by:

$$\begin{pmatrix} -(\frac{1}{32}+2\mu\rho_0)k^2 - \chi Q_0\bar{k}^2 & -(\frac{\pi}{48}+\chi\rho_0)\bar{k}^2 + 4Q_0\lambda k^2 & -(\frac{\pi}{24}+2\chi\rho_0)k_xk_y \\ \frac{4Q_0}{\rho_{cr}} - \zeta\bar{k}^2/2 & -4\alpha Q_0^2 + (2\beta_1+\beta_2)Q_0\bar{k}^2 - \kappa k^2 & 0 \\ -\zeta k_xk_y & 2(2\beta_1+\beta_2)Q_0k_xk_y & 4\left(\frac{\rho_0}{\rho_{cr}}-1\right) - 2\alpha Q_0^2 - \kappa k^2 \end{pmatrix} \tag{3.34}$$

where $k^2 = k_x^2 + k_y^2$, and $\bar{k}^2 = k_x^2 - k_y^2$. We proceed by studying the linear stability of various base states.

Stability of the homogeneous and isotropic state

Linear stability of the homogeneous and isotropic state is determined by the eigenvalue problem, Eq. (3.33) with $Q_0 = 0$. Explicitly solving the eigenvalue problem, yields

$$\hat{\sigma} = 4\left(\rho_0/\rho_{cr} - 1\right) - \kappa k^2 \tag{3.35}$$

for the most unstable eigenvalue. The instability sets in at $k = 0$ and $\rho_0 = \rho_{cr}$, corresponding to the transition to a globally-ordered nematic state (see Fig. 3.6 (left)).

Linear Stability of the Nematic State

For $\rho_0 > \rho_{cr}$, the homogeneous and isotropic state is unstable towards the formation of a global nematic phase with the amplitude Q_0, given by the spatially-independent terms in Eq. 3.30

$$Q_0 = \sqrt{\frac{2}{\alpha}\left(\frac{\rho_0}{\rho_{cr}} - 1\right)}. \tag{3.36}$$

Using this value in Eq. (3.33) yields an eigenvalue problem that is too complicated to analyse analytically, and, instead, we study it numerically using Wolfram Mathematica. First, we observe that the globally oriented nematic state is always linearly unstable for $\rho_{cr} < \rho_0 < \rho_N$ (i.e., the region between the blue and orange lines in Fig. 3.6 (right)), where the upper phase boundary ρ_N is determined numerically. The most unstable perturbations correspond to $k_x = 0$, with the eigenvector in the form $(\delta\rho, \delta Q_{xx}, 0)$. This instability results in the modulation of the density and nematic order in the direction perpendicular to the nematic direction and indicates the formation of the nematic bands.

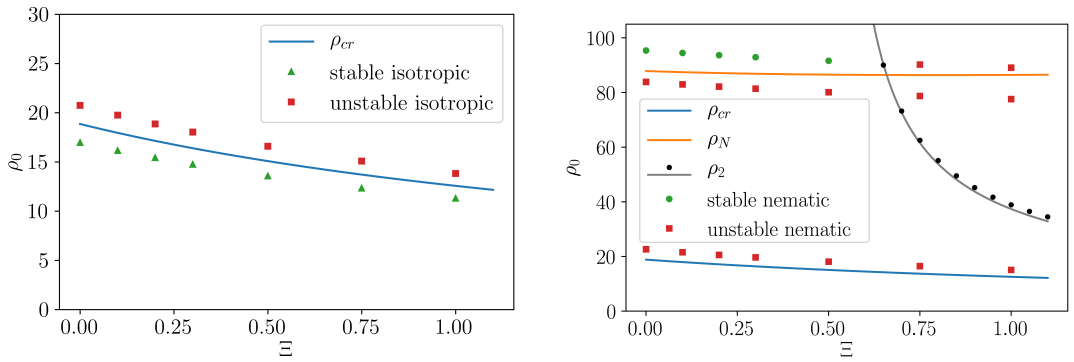

Figure 3.6: Liner stability of the minimal model: (left) stability of the homogeneous isotropic state, green triangles and red squares represent stable and unstable solutions obtained in the numerical solutions; (right) stability of the nematic phase. The region between the blue and orange lines is unstable to phase separation; the region above the black dots denote the second instability described in the text (the gray line is the analytical approximation for this instability based on Eq. (3.37)). Green circles and red squares represent stable and unstable solutions obtained in the numerical solutions. For both cases $\eta = 1$ and $\tau_0 = 0.5$.

Second Linear Instability of the Nematic State

As discussed in the main text, for densities significantly larger than ρ_{cr}, there exists another linear instability of the global nematic state, which is different from the one discussed above. Numerical analysis shows that the correspond-

ing eigenvector has a significant δQ_{xx} component, and a very small density modulation $\delta\rho$. To get an insight into the nature of this instability, we set $\delta\rho$ to zero in Eq. (3.33) to obtain a simple problem with the most unstable eigenvalue given by

$$\hat{\sigma} = 4\left(\rho_0/\rho_{cr} - 1\right) - 6\alpha Q_0^2 + (2\beta_1 + \beta_2)Q_0\bar{k}^2 - \kappa k^2. \tag{3.37}$$

For all the values of parameters discussed in this work, the coefficient in front of k_y^2 is always negative, and we conclude that the most unstable eigenvalue corresponds to $k_y = 0$. This eigenvalue becomes positive when $(2\beta_1 + \beta_2)Q_0 > \kappa$. For the parameters used in our analysis, $\eta = 1$ and $\tau_0 = 1/2$, this condition can be satisfied for $\Xi > 0.49$, and the corresponding densities above which the instability arises are given in Fig. 3.6 (right) as black circles (the analytical approximation for the instability boundary, Eq. (3.37), is shown as a grey line). As Eq. (3.37) suggests, our minimal model does not predict a selected lengthscale for this instability due to the lack of higher-order spatial gradients in Eqs. (3.29) and (3.30), and, instead, the fastest growth is observed at the smallest scale available. This instability exists only for relatively large values of Ξ and ρ_0 and is superseded by the main instability.

3.5.3 Coarsening

As was mentioned in the Subsections 3.5.1 and 3.5.2, in the case where the interaction rates are isotropic ($\Xi = 0$), nematic domains undergo a coarsening process and tend to form one band in the steady state. (It is valid for both full and minimal models, and below we consider the minimal one).

To characterise the way in which domains coarsen, we here quantify how the typical domain length scale ℓ grows with time. Simulations to compute ℓ as a function of time t are initialised with a system with uniform density and nematic order, with a small amount of noise.

After a brief transient period (not shown) we observe that the length scale ℓ of nematic domains grows as $\ell \sim t^{\theta}$, where $\theta \approx 0.25$ (Fig. 3.7a), in line with numerical results obtained for the growth of passive nematic droplets [14]. We note that the value of the exponent is also numerically close to the one observed for the growth of droplets of spherical self-propelled particles in motility-induced phase separation[15]. We also observe that the width of eventual band scales with the system size (Fig. 3.7b).

In the regime where we observe dry active turbulence, domains transiently coarsen to form one or few bands; however they undergo subsequent instabilities according to the mechanism described later.

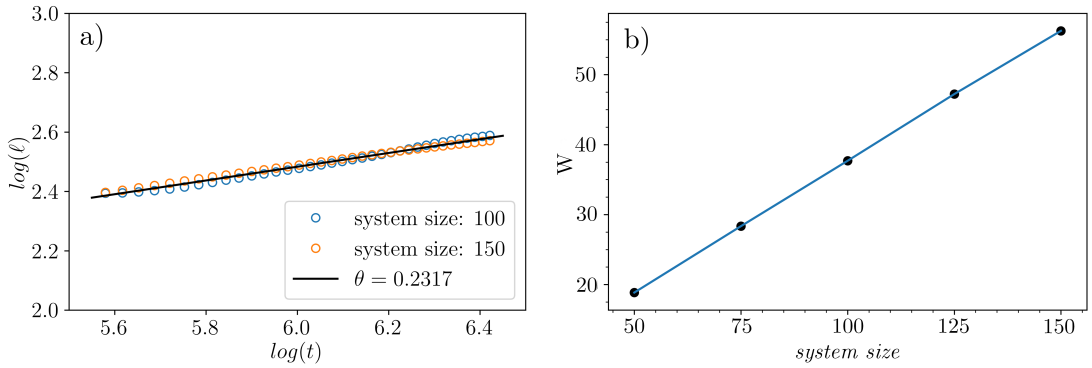

Figure 3.7: a) plot of the characteristic lengthscale ℓ as a function of time. Blue and orange circles are numerical result corresponding the systems of different size (minimal model, $\Xi = 0$, $\rho_0 = 1.1\rho_{cr}$); the solid line is the power-law fit $\ell \sim t^{\theta}$. b) the width of the band W scales with the system size.

3.5.4 Main mechanisms

We now discuss the physical meaning of each term in Eqs. (3.29) and (3.30). First, μ and λ determine the non-equilibrium chemical potential of our mixture: their main role is to set the values of the densities in the isotropic and nematic phases. Next, α is a non-equilibrium Landau coefficient setting the magnitude of order in the bulk (together with the term $4\,(\rho/\rho_{cr} - 1)\,Q_{ij}$), while κ is the nematic elastic constant. Similar terms are also present in a purely passive *Model C* [16] describing, for instance, phase separation in passive liquid crystals. The key *qualitative* ingredients that produce chaotic behaviour in our model are the "active" terms proportional to χ, ζ, β_1 and β_2. Among them, χ is the "extensile flux", whose role is similar to that of extensile stress in active gels [17, 18]. This term enhances diffusion along the direction of the local nematic order (i.e., the eigenvector of Q_{ij} corresponding to its positive eigenvalue), and decreases it along the perpendicular direction (Fig. 3.8a). Second, ζ creates an effective torque at the interface, as the associated term depends on density gradients, which are largest at the interface (Fig. 3.8b). When ζ is positive (negative), it tends to orient MTs parallel (perpendicular) to an isotropic-nematic interface. Finally, β_1 and β_2 create modulation of the nematic ordering (i.e., the positive eigenvalue of Q_{ij}). These terms promote activity-induced disorder and act similarly to a negative elastic constant in conventional liquid crystals. Additionally, they contribute to the interfacial torque at the boundary of a nematic band, where $Q_{kl}Q_{kl}$ drops sharply to zero, following the density field (Fig. 3.8b).

The minimal model obtained above is simple enough for us to dissect the mechanisms underlying pattern formation. The kinetic pathway leading to non-equilibrium phase separation proceeds as follows. Starting from a uniform disordered solution with $\rho > \rho_{cr}$, MTs rapidly acquire an orientational

order, through the Landau coupling in Eq. (3.30). At this point, the extensile active flux, arising from MT sliding, enhances diffusion along the nematic direction and hinders it perpendicularly. When this effect is strong enough, the perpendicular diffusion becomes effectively negative, causing MT bundling and the formation of one or more nematically ordered high-density bands (see Fig. 3.3). Although the phase separation is driven by a non-equilibrium phenomenon (MM activity), the kinetic growth laws resemble phase separation in passive mixtures of liquid crystalline and isotropic fluids [14, 16], as it was discussed above (see Fig. 3.7).

When the anisotropy in motor-induced alignment, measured by Ξ is sufficiently large, the $\beta_{1,2}$ terms dominate over both the restoring elastic constant κ and the ζ term: the associated torque rotates the MTs at the nematic-isotropic interface, so that they tend to orient perpendicular to the band border. This interfacial alignment conflicts with the direction of the nematic order within the bulk of the band; it couples to the extensile flux to yield locally synchronous rotation (and stretching) of nematic bands as observed in our simulations. This cycle repeats, creating a never-settling pattern, as seen in our simulations in the dry active turbulent regime (Figs. 3.3 and 3.5a). The direction of the emerging band rotation (clockwise or anticlockwise) is selected by spontaneous symmetry breaking, it may be different in different regions of our simulation domain, yielding a chaotic pattern (Fig. 3.5b). Measuring the time evolution of the domain size in this regime yields statistically the same results as for the full model (Figs. 3.3g and h).

There is also a second mechanism that can destabilise a homogeneous nematic state, again dependent on $\beta_{1,2}$. A linear stability analysis starting from the uniform nematic phase (Section 3.5.2) shows that when these terms are large enough, they trigger the development of modulation in Q_{ij} – in the direction parallel to that of the nematic order, for $\beta_{1,2} > 0$. This instability is independent of density fluctuations and ultimately fragments the nematic phase into infinitely small microdomains. This pathway to chaos is related to that identified in [19, 20] for the dry active matter with near-uniform density. However, in our model, this instability is only relevant for $\rho_0 \gg \rho_{cr}$, and for lower ρ_0 is superseded by the turbulent phase separation dynamics discussed above.

3.5.5 Phenomenological model

While our minimal model is the result of a systematic coarse-graining, we can view Eqs. (3.29) and (3.30), more generally, as a phenomenological model that contains the lowest terms of the correct tensorial nature [21]. Upon coarse-graining, a microscopic model within the same universality class as the one studied here would, therefore, provide the expressions for the parameters in

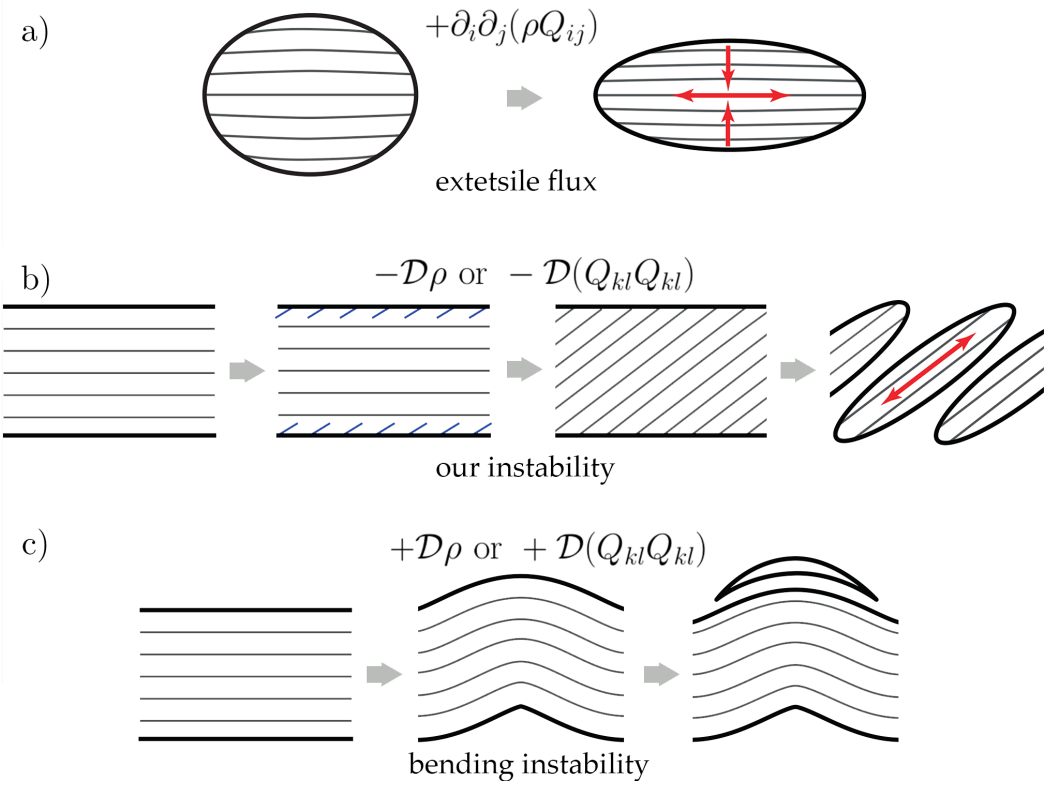

Figure 3.8: Cartoons depicting corresponding mechanisms. a) extensile flux; b-c) destabilisation of the band due to the effective torque at the interface: b) our instability, c) bending instability observed in the phenomenological model.

Eqs. (3.29) and (3.30), but would not generate extra terms. Indeed, setting $\beta_{1,2} = \lambda = \mu = 0$ shows that our equations, in this limit, reduce to the minimal model for flocking of self-propelled particles with nematic order [22–25]. We, therefore, propose Eqs. (3.29) and (3.30) as a unifying model for dry active systems with nematic order. Recently, similar arguments were used to propose active versions of Models B and H [15, 26] in Hohenberg-Halperin classification [16]. We follow this analogy and refer to Eqs. (3.29) and (3.30) as *active Model C*. This model is in a different universality class with respect to active gel theory [18], which exhibits instabilities in an active nematic fluid with constant density, whereas in our case patterns are always associated with non-equilibrium phase separation. We want to stress that while previous work reported types of chaotic behaviour similar to the limiting cases of our model, either based on hydrodynamic [22, 23] or kinetic theories [24], active Model C unifies all this into a general universality class.

Analysis of active Model C with phenomenological coefficients re-enforces our physical interpretation of the instability modes. First, nematic-isotropic phase separation also occurs with $\zeta = \beta_{1,2} = 0$, confirming that this phenomenon relies solely on a non-zero extensile flux, $\chi \neq 0$ (Fig. 3.5c). Second, setting $\chi = 0$ whilst retaining $\beta_{1,2}$ and ζ only leads to a uniform nematic phase, confirming that χ is necessary for any patterning. Third, switching off only ζ

leads to chaotic dynamics for a much wider parameter range, including $\Xi = 0$ (Fig. 3.5d), as now $\beta_{1,2}$ only need to compete with the elastic constant κ. Fourth, switching off only $\beta_{1,2}$ whilst retaining $\zeta > 0$ does not lead to chaotic dynamics as in Fig. 3.3b and 3.5 a,b, as there is no competition between the orientational order in bulk and at the interface. This case, however, yields another interesting instability associated with interfacial undulations and an elastic bend deformation in the nematic order (Figs. 3.5e and 3.8c). The ensuing patterns may also be chaotic for sufficiently large ζ , and are similar to the structures seen experimentally in microtubule-kinesin mixtures [5].

Thus, the essential physics of active Model C is the following: 1) evolution equation for scalar parameter (density) contains a generalised chemical potential and term responsible for the extensile flux, (eventually these two terms govern the phase separation in density), 2) evolution equation for the tensor parameter (Q_{ij}) consists of classic Landau terms organising the isotropic-nematic transition and terms proportional to $\beta_{1,2}$ and ζ, that eventually cause the instability of MT bands. The type of instability depends on the values of parameters $\beta_{1,2}$ and ζ, in our minimal model we observe only one type of instability but in phenomenological model the additional instability (bending instability) can be realised.

One should notice, that we use term Model C just to emphasise the analogy to the Hohenberg-Halperin classification of passive systems, while the system we consider is active. Unlike the usual Model C we cannot construct a free energy functional able to provide our field equations after the taking the Euler-Lagrange functional derivative.

For various values of its parameters, active Model C serves as a catalogue of patterns in dry active systems. As mentioned above, a subset of terms in Eqs. (3.29) and (3.30) was obtained in models of flocking of self-propelled particles with nematic order [22–25]. Within those models, rigorous coarse-graining shows that χ and ζ are both positive, and, accordingly, the generic outcome found by numerical solutions [22–25] is non-equilibrium phase separation and chaos through band undulations (as in Fig. 3.5e). Based on our phenomenological model and interpretation, we also expect dry active turbulence with contractile active flux, $\chi < 0$, and interfacial torques favouring parallel alignment at the interface, as would occur when ζ, or $\beta_{1,2}$ are positive. This scenario may be relevant for pattern formation in MT-MM mixtures where the underlying microscopic collision rules differ from those in Figure 3.1, e.g., where the critical angle below which there is polar ordering differs from $\pi/2$.

3.6 Discussion

In this Chapter, we built on the kinetic theory of microtubule-motor mixtures and methods of coarse-graining developed in the previous Chapter. We started with the kinetic equation encoding sliding/clustering interaction motor-induced interaction between MTs, in accordance with the current view of kinesin motors. This equation was coarse-grained into a set of dynamical equations for the density field, polar and nematic alignment order parameters. We call resulting set of equations the "full model".

With the linear stability analysis and direct numerical solutions, we studied the full model, analysed the corresponding pattern formation and instabilities and obtained a phase diagram.

For the explored range of parameters, the full model exhibited the formation of high-density clusters at high enough densities, with ensuing formation of bands with nematic order in the bulk (and polar order at the interface). Depending on the anisotropy parameters these structures appeared to be either stable or unstable.

To establish the mechanism of pattern formation in the full model we obtained a simpler set of equations (minimal model), recapitulating general properties of the full model.

The linear stability analysis and numeric simulations of the minimal model demonstrated that its phase diagram is similar to the full one. Thus, comparing full and minimal sets of equations we conclude that within the relevant range of parameters the minimal model reproduces the long-wavelength dynamics of the full model, and assume, that behaviour of both sets of equations can be explained with the same physical mechanism.

The minimal model allowed us to elucidate this mechanism and detect the following necessary ingredients: an extensile flux and interfacial torque providing ordering along the gradients of densities. We also determined the physical meaning of each term of the minimal model.

Finally, we investigated our minimal model with phenomenological coefficients, and arrived at a conclusion, that this model provides an active case of Model C [16]. By analogy to the active turbulence [27] we offered the term *dry active turbulence* and assumed that our model may constitute a general universality class shared between nematically ordered microtubules and flocking self-propelled particles. However, further work is required to identify the criteria for a microscopic model to belong to the universality class of our active Model C.

References

[1] A. Mogilner and E. Craig, "Towards a quantitative understanding of mitotic spindle assembly and mechanics," *J. Cell Sci.*, vol. 123, pp. 3435–3445, 2010.

[2] K. S. Burbank, T. J. Mitchison, and D. S. Fisher, "Slide-and-Cluster Models for Spindle Assembly," *Curr. Biol.*, vol. 17, no. 16, pp. 1373–1383, 2007.

[3] J. Brugués and D. Needleman, "Physical basis of spindle self-organization.," *Proc. Natl. Acad. Sci. U. S. A.*, vol. 111, pp. 18496–500, 2014.

[4] T. Sanchez, D. Welch, D. Nicastro, and Z. Dogic, "Cilia-Like Beating of Active Microtubule Bundles," *Science (80-.).*, vol. 333, pp. 456–459, 2011.

[5] T. Sanchez, D. T. N. Chen, S. J. Decamp, M. Heymann, and Z. Dogic, "Spontaneous motion in hierarchically assembled active matter," *Nature*, vol. 491, no. 11591, pp. 1–5, 2012.

[6] P. Guillamat, J. Ignés-Mullol, and F. Sagués, "Control of active liquid crystals with a magnetic field," *Proc. Natl. Acad. Sci.*, vol. 113, no. 20, pp. 5498–5502, 2016.

[7] C. Leduc, K. Padberg-Gehle, V. Varga, *et al.*, "Molecular crowding creates traffic jams of kinesin motors on microtubules," *Proc. Natl. Acad. Sci.*, vol. 109, pp. 6100–6105, 2012.

[8] A. Parmeggiani, T. Franosch, and E. Frey, "Phase Coexistence in Driven One-Dimensional Transport," *Phys. Rev. Lett.*, vol. 90, p. 086601, 2003.

[9] M. Doi and S. F. Edwards, *Theory Polym. Dyn.* Oxford University Press, 1986.

[10] I. Maryshev, D. Marenduzzo, A. B. Goryachev, and A. Morozov, "Kinetic theory of pattern formation in mixtures of microtubules and molecular motors," *Phys. Rev. E*, vol. 97, p. 22412, 2018.

[11] I. S. Aranson and L. S. Tsimring, "Theory of self-assembly of microtubules and motors," *Phys. Rev. E*, vol. 74, p. 31915, 2006.

[12] F. Ziebert and W. Zimmermann, "Comment on "Instabilities of isotropic solutions of active polar filaments"," *Phys. Rev. Lett.*, vol. 93, no. 15, p. 159801, 2004.

[13] L. Giomi, T. B. Liverpool, and M. C. Marchetti, "Sheared active fluids: Thickening, thinning, and vanishing viscosity," *Phys. Rev. E*, vol. 81, p. 051908, 2010.

[14] M. Mata, C. J. García-Cervera, and H. D. Ceniceros, "Ordering kinetics of a conserved binary mixture with a nematic liquid crystal component," *J. Non-Newton. Fluid Mech.*, vol. 212, pp. 18–27, 2014.

[15] J. Stenhammar, A. Tiribocchi, R. J. Allen, D. Marenduzzo, and M. E. Cates, "Continuum theory of phase separation kinetics for active Brownian particles," *Phys. Rev. Lett.*, vol. 111, no. 14, p. 145702, 2013.

[16] P. C. Hohenberg and B. I. Halperin, "Theory of dynamic critical phenomena," *Rev. Mod. Phys.*, vol. 49, no. 3, p. 435, 1977.

[17] R. A. Simha and S. Ramaswamy, "Hydrodynamic fluctuations and instabilities in ordered suspensions of self-propelled particles," *Phys. Rev. Lett.*, vol. 89, no. 5, p. 058101, 2002.

[18] M. C. Marchetti, J.-F. Joanny, S. Ramaswamy, *et al.*, "Hydrodynamics of soft active matter," *Rev. Mod. Phys.*, vol. 85, no. 3, p. 1143, 2013.

[19] E. Putzig, G. S. Redner, A. Baskaran, and A. Baskaran, "Instabilities, defects, and defect ordering in an overdamped active nematic," *Soft Matter*, vol. 12, no. 17, pp. 3854–3859, 2016.

[20] P. Srivastava, P. Mishra, and M. C. Marchetti, "Negative stiffness and modulated states in active nematics," *Soft Matter*, vol. 12, no. 39, pp. 8214–8225, 2016.

[21] A. N. Beris and B. J. Edwards, *Thermodynamics of Flowing Systems: with Internal Microstructure*. Oxford Engineering Science Series, Oxford University Press, 1994.

[22] A. Peshkov, I. S. Aranson, E. Bertin, H. Chaté, and F. Ginelli, "Nonlinear field equations for aligning self-propelled rods," *Phys. Rev. Lett.*, vol. 109, no. 26, p. 268701, 2012.

[23] S. Ngo, A. Peshkov, I. S. Aranson, *et al.*, "Large-scale chaos and fluctuations in active nematics," *Phys. Rev. Lett.*, vol. 113, no. 3, pp. 1–6, 2014.

[24] X.-Q. Q. Shi, H. Chaté, and Y.-Q. Q. Ma, "Instabilities and chaos in a kinetic equation for active nematics," *New J. Phys.*, vol. 16, no. 3, p. 35003, 2014.

[25] R. Großmann, F. Peruani, and M. Bär, "Mesoscale pattern formation of self-propelled rods with velocity reversal," *Phys. Rev. E*, vol. 94, no. 5, p. 50602, 2016.

[26] A. Tiribocchi, R. Wittkowski, D. Marenduzzo, and M. E. Cates, "Active model H: scalar active matter in a momentum-conserving fluid," *Phys. Rev. Lett.*, vol. 115, no. 18, p. 188302, 2015.

[27] L. Giomi, "Geometry and Topology of Turbulence in Active Nematics," *Phys. Rev. X*, vol. 5, p. 31003, 2015.

Summary and outlook

Using our kinetic theory of the pattern formation in MT-MM mixtures we derived two continuous models, describing two types of motor-induced interaction between microtubules.

For the sake of brevity let us introduce short names and denote the model devoted to the polar clustering of MTs as "Model 1" (see Chapter 2) and the model investigating sliding/clustering interaction of MTs as "Model 2" (see Chapter 3); corresponding interaction rules are depicted in Fig. S1. In this summary, we discuss the features that unify these two models and emphasise the discrepancies between them (Fig. S1).

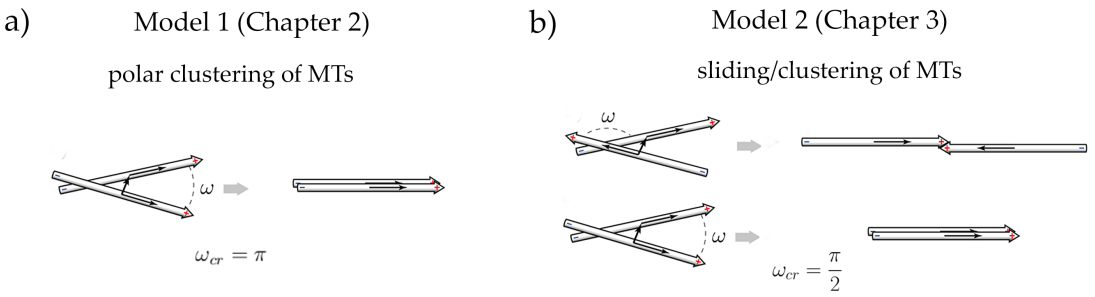

Figure S1: Two models provided in the work: a) Model 1 devoted to polar clustering of MTs, b) Model 2 devoted to polar sliding/clustering of MTs.

Since the obtained models are based on different microscopic rules, they yield the formation of distinct complex patterns. We observe that the polar clustering considered in Model 1 gives rise to structures with a polar order, while sliding/clustering interaction in Model 2 eventually leads to the formation of the patterns with a nematic symmetry.

Both models demonstrate that initially three slow variables should be taken into account: the MT density field ρ, orientation p_i and nematic alignment tensor Q_{ij}. In both cases, one variable can be eventually enslaved, namely nematic alignment Q_{ij} in case of Model 1(QC) and orientation p_i in Model 2.

In both cases, the homogeneous isotropic distribution of MTs becomes unstable with respect to small perturbations, and at densities exceeding the critical one, systems acquire an orientational state (polar for Model 1 and nematic for Model 2). This spontaneous ordering is induced by the Landau-like coupling in the evolution equations for the corresponding order parameter. As one can see, Landau terms are present in the equation for orientation in our Model 1 and in the equation for nematic alignment in Model 2.

In both scenarios we observe the formation of domains with increased density; however, the reasons for this phase separation are different. Generally, we found two mechanisms of the density "demixing": 1) "bundling instability", which can be reduced to the effective negative diffusion in the equation the MT

density; 2) extensile (or contractile) MT flux, which enhances diffusion along the nematic direction, and hinders it perpendicular direction (or vice versa in case of contractile flux). The first mechanism takes place in Model 1; the second one is implemented in both models; extensile flux is considered in Model 2, while term responsible for the contractile flux can be found in the density equation of Model 1 (QC). Note, that "bundling instability" is an isotropic process, while fluxes, whose roles are analogue to that of the active stresses in active gels, are intrinsically anisotropic (Fig. S2).

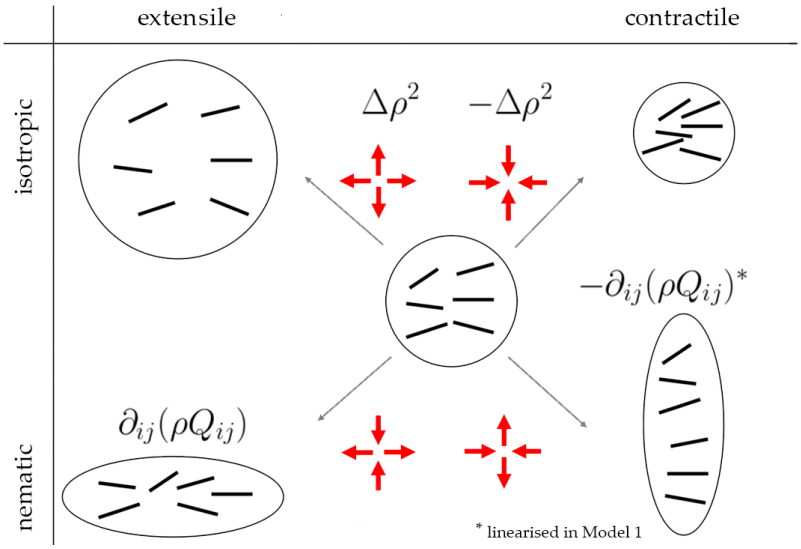

Figure S2: Motor-induced MT fluxes can be isotropic/nematic or extensile/-contractile. Effective diffusion is isotropic extensile flux, term yielding the "bundling instability" represents isotropic contractile flux, extensile and contractie fluxes $\partial_{ij}(\rho Q_{ij})$ have anisotropic (nematic) nature.

Finally, at least within some range of the parameters space, both models produce ever-evolving chaotic bands with the polar (Model 1) or nematic (Model 2) order in bulk. To some extent, we can say that both models provide an example of the *dry active turbulence*.

Regarding the basic MT patterns discussed in Chapter 1, our models successfully reproduce formation of asters, parallel arrays (see results of Model 1) and mixed arrays (see results of Model 2).

Thus, we obtained a kinetic theory able to bridge two scales – macroscopic dynamics of the active cytoskeleton and the underlying microscopic interactions of MTs provided by MMs. However, several open questions remain, and we hope to address some of them in future work.

First of all, in our model we used quite oversimplified collision rules, however nowadays interaction between biofilaments are actively investigated, and therefore new quantitative data can be used in the future for more realistic rules of interaction.

In the developed theory molecular motors enter the model implicitly by

specifying the interaction rules. It means that the distribution of accessible motors is homogeneous. We plan to introduce an additional variable for the concentration of motors and investigate the role of spatial inhomogeneity of motors. This improvement is more relevant to the formation of structures with polar order since in the nematic MT arrangement motors jump between antiparallel filaments, so they change direction stochastically, and hence their global advection is suppressed.

This step would allow us to explore MT pattern formation in the presence of two types of motors, e.g. minus-directed clustering motors and plus-directed sliding motors. Two evolving populations motors can help to address the problem of formation of the mitotic spindle and other self-organising *in vivo* structures.

Additionally, the computational part of this thesis could be improved by switching to the Fourier spectral methods.

It would be interesting to determine the role of confinement (or boundary conditions) and the dynamics of MT pattern formation processes on curved surfaces.

Other exciting directions include the addition of motors fixed to the substrate. Introduction of such motors could connect our model and existing theories devoted to motility assays.

Finally, our models make some predictions that could be experimentally verified. E.g. we predict that phase diagram of MT-MM mixture depends on the anisotropy of motor distribution along the individual MT. This fact was mentioned in several experimental works but have never been studied directly. In Model 2, we observe polar order at the interface of nematic domains, which has not previously been mentioned in experimental studies.

Appendix A

Kinetic equation derivation

Rule of interaction between MTs imposes the conditions for initial configuration $(\mathbf{r}_i^b, \mathbf{n}_i^b)$ necessary for the interaction, and determine resulting arrangement $(\mathbf{r}_i^a, \mathbf{n}_i^a)$. In case of polar clustering interaction rule can be written in vector notation:

$$\begin{cases} \mathbf{n}_1^a = \mathbf{n}_2^a = \frac{\mathbf{n}_1^b + \mathbf{n}_2^b}{|\mathbf{n}_1^b + \mathbf{n}_2^b|}, \\ \mathbf{r}_1^a = \mathbf{r}_2^a = \frac{\mathbf{r}_1^b + \mathbf{r}_2^b}{2}. \end{cases} \tag{A1}$$

It is convenient to rewrite the angular part of the interaction rule in angles. Let us introduce relative angle between the MTs $\omega = \phi_2^b - \phi_1^b$. Because of 2π periodicity of angular space different collision rules should be defined for two areas: $C_1 : |\omega| \in (0, \phi_0)$ and $C_2 : |\omega| \in (2\pi - \phi_0, 2\pi)$, where ϕ_0 is critical angle:

$$\begin{cases} \phi_1^a = \phi_2^a = \frac{\phi_1^b + \phi_2^b}{2}, & \text{if } |\phi_2^b - \phi_1^b| \in (0, \phi_0) \\ \phi_1^a + \pi = \phi_2^a - \pi = \frac{\phi_1^b + \phi_2^b}{2}, & \text{if } |\phi_2^b - \phi_1^b| \in (2\pi - \phi_0, 2\pi). \end{cases} \tag{A2}$$

For area C_2 substitution $\phi_1^a \to \phi_1^a + \pi,\ \phi_2^a \to \phi_2^a - \pi$ has been used to pick a smaller angle between rods. In the following ϕ_0 is assumed to be equal π, therefore integration regions C_1 and C_2 correspond to $|\omega| \in (0, \pi)$ and $|\omega| \in (\pi, 2\pi)$ respectively. Interaction integral reads:

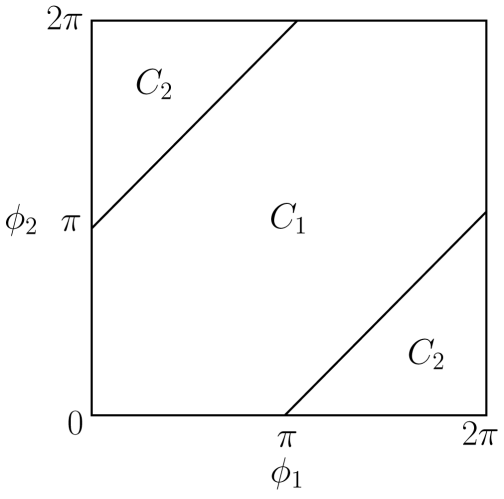

Figure A1: Angular phase space.

$$
\begin{aligned}
I_{int} = \iint d\mathbf{r}_1 d\mathbf{r}_2 \Bigg\{ & \iint_{C_1} d\phi_1 d\phi_2 \Bigg[W\left(\mathbf{r}_1, \mathbf{r}_2; \phi_1, \phi_2\right) \\
& \times P\left(\mathbf{r}_1, \phi_1\right) P\left(\mathbf{r}_2, \phi_2\right) \delta\left(\frac{\phi_1 + \phi_2}{2} - \phi\right) \delta\left(\frac{\mathbf{r}_1 + \mathbf{r}_2}{2} - \mathbf{r}\right) \\
& - W\left(\mathbf{r}_1, \mathbf{r}_2; \phi_1, \phi_2\right) P(\mathbf{r}_1, \phi_1) P(\mathbf{r}_2, \phi_2) \, \delta\left(\phi_2 - \phi\right) \delta(\mathbf{r}_2 - \mathbf{r}) \Bigg] \\
& + \iint_{C_2} d\phi_1 d\phi_2 \Bigg[W\left(\mathbf{r}_1, \mathbf{r}_2; \phi_1, \phi_2\right) \\
& \times P\left(\mathbf{r}_1, \phi_1\right) P\left(\mathbf{r}_2, \phi_2\right) \delta\left(\frac{\phi_1 + \phi_2}{2} + \pi - \phi\right) \delta\left(\frac{\mathbf{r}_1 + \mathbf{r}_2}{2} - \mathbf{r}\right) \\
& - W\left(\mathbf{r}_1, \mathbf{r}_2; \phi_1, \phi_2\right) P(\mathbf{r}_1, \phi_1) P(\mathbf{r}_2, \phi_2) \, \delta\left(\phi_2 - \phi\right) \delta(\mathbf{r}_2 - \mathbf{r}) \Bigg] \Bigg\}
\end{aligned}
\tag{A3}
$$

Introducing the following substitutions:

$$
x = \phi_1 + \phi_2, \quad \omega = \phi_2 - \phi_1 \quad (\phi_1 = x/2 - w/2, \quad \phi_2 = x/2 + w/2) \tag{A4}
$$

and performing integration over the angular dependent Dirac δ-functions we obtain:

$$
\begin{aligned}
\iint d\mathbf{r}_1 d\mathbf{r}_2 \int_{-\pi}^{\pi} d\omega \Bigg[& W\left(\mathbf{r}_1, \mathbf{r}_2; \phi - \frac{\omega}{2}, \phi + \frac{\omega}{2}\right) \\
& \times P\left(\mathbf{r}_1, \phi - \frac{\omega}{2}\right) P\left(\mathbf{r}_2, \phi + \frac{\omega}{2}\right) \delta\left(\frac{\mathbf{r}_1 + \mathbf{r}_2}{2} - \mathbf{r}\right) \\
& - W(\mathbf{r}_1, \mathbf{r}_2; \phi - \omega, \phi) P(\mathbf{r}_1, \phi - \omega) P(\mathbf{r}_2, \phi) \delta(\mathbf{r}_2 - \mathbf{r}) \Bigg],
\end{aligned}
\tag{A5}
$$

Integrating over position dependent δ-functions we obtain:

$$
\begin{aligned}
\int d\mathbf{r}_1 \Bigg[& 4 \int_{-\pi}^{\pi} d\omega W\left(\mathbf{r}_1, 2\mathbf{r} - \mathbf{r}_1; \phi - \frac{\omega}{2}, \phi + \frac{\omega}{2}\right) P\left(\mathbf{r}_1, \phi - \frac{\omega}{2}\right) P\left(2\mathbf{r} - \mathbf{r}_1, \phi + \frac{\omega}{2}\right) \\
& - \int_{-\pi}^{\pi} d\omega W(\mathbf{r}_1, \mathbf{r}; \phi - \omega, \phi) P\left(\mathbf{r}_1, \phi - \omega\right) P\left(\mathbf{r}, \phi\right) \Bigg].
\end{aligned}
\tag{A6}
$$

And finally, performing the coordinate transformation:

$$
\begin{aligned}
& r_1 = r - \frac{\xi}{2}, d\xi = 4dr, \\
& r_1 = r - \xi, d\xi = dr,
\end{aligned}
\tag{A7}
$$

we obtain final expression for the interaction integral Eq.2.2:

$$\int d\boldsymbol{\xi} \int_{-\pi}^{\pi} d\omega \Bigg[W\left(\mathbf{r}-\frac{\boldsymbol{\xi}}{2},\phi-\frac{\omega}{2};\mathbf{r}+\frac{\boldsymbol{\xi}}{2},\phi+\frac{\omega}{2}\right) \times P\left(\mathbf{r}-\frac{\boldsymbol{\xi}}{2},\phi-\frac{\omega}{2}\right) P\left(\mathbf{r}+\frac{\boldsymbol{\xi}}{2},\phi+\frac{\omega}{2}\right) - W(\mathbf{r},\phi;\mathbf{r}-\boldsymbol{\xi},\phi-\omega) P(\mathbf{r},\phi)\, P(\mathbf{r}-\boldsymbol{\xi},\phi-\omega) \Bigg]. \tag{A8}$$

Interaction integrals

Below we describe evaluation of the interaction integrals necessary to derive hydordynamic equations from Eq 2.5 in the Chapter 2. All integrals are expressed in terms of auxiliary variables $\chi = \psi - \phi$ and $\boldsymbol{\zeta} = \boldsymbol{\xi}/L$. The interaction kernels W_1 and W_2, defined in the Chapter 2, can therefore be written as

$$W_1 = G\,\Theta\left(|\sin\omega| - 2\zeta\left|\sin\left(\chi+\frac{\omega}{2}\right)\right|\right)\Theta\left(|\sin\omega| - 2\zeta\left|\sin\left(\chi-\frac{\omega}{2}\right)\right|\right) \times\left\{1+\Xi\left[\Theta\left(-2\zeta\frac{\sin\left(\chi+\frac{\omega}{2}\right)}{\sin\omega}-\tau_0\right)+\Theta\left(-2\zeta\frac{\sin\left(\chi-\frac{\omega}{2}\right)}{\sin\omega}-\tau_0\right)\right]\right\}, \tag{A9}$$

$$W_2 = G\,\Theta\left(|\sin\omega| - 2\zeta\,|\sin\chi|\right)\Theta\left(|\sin\omega| - 2\zeta\,|\sin(\chi+\omega)|\right) \times\left\{1+\Xi\left[\Theta\left(-2\zeta\frac{\sin\chi}{\sin\omega}-\tau_0\right)+\Theta\left(-2\zeta\frac{\sin(\chi+\omega)}{\sin\omega}-\tau_0\right)\right]\right\}. \tag{A10}$$

Zeroth-order integrals $\overline{I_{nm}^{(0)}}^{s}$ and $\overline{J_{nm}^{(0)}}^{s}$

The zeroth-order integrals are given by

$$\overline{I_{nm}^{(0)}}^{s} = \overline{e^{i(n+m)\phi}L^2\int_0^{2\pi}d\chi\int_0^{\infty}d\zeta\,\zeta\int_{-\pi}^{\pi}d\omega\,W_1 e^{i(m-n)\frac{\omega}{2}}}^{s}, \tag{A11}$$

$$\overline{J_{nm}^{(0)}}^{s} = \overline{e^{i(n+m)\phi}L^2\int_0^{2\pi}d\chi\int_0^{\infty}d\zeta\,\zeta\int_{-\pi}^{\pi}d\omega\,W_2 e^{-im\omega}}^{s}. \tag{A12}$$

Projection on the s-th Fourier mode trivially yields

$$\frac{1}{2\pi}\int_0^{2\pi} e^{is\phi}e^{i(n+m)\phi}d\phi = \delta_{n,s-m}, \tag{A13}$$

and, hence,

$$\overline{I_{j,nm}^{(0)}}^{s} = \delta_{n,s-m}L^2\int_0^{2\pi}d\chi\int_0^{\infty}d\zeta\,\zeta\int_{-\pi}^{\pi}d\omega W_1 e^{i(m-n)\frac{\omega}{2}}, \tag{A14}$$

$$\overline{J^{(0)}_{j,nm}}^{s} = \delta_{n,s-m} L^2 \int_0^{2\pi} d\chi \int_0^{\infty} d\zeta\, \zeta \int_{-\pi}^{\pi} d\omega W_2 e^{-im\omega}. \tag{A15}$$

Evaluating these integrals numerically, we observe that their joint contribution to the equation of motion for the probability distribution function P, Eq.2.5 of the main text, can be conveniently written as

$$\partial_t P_s = \sum_{n,m} \left[\overline{I^{(0)}_{j,nm}}^{s} - \overline{J^{(0)}_{j,nm}}^{s} \right] P_n P_m + \cdots = GL^2 \left(1 + a_1\right) \sum_m P_{s-m} P_m I_{s-m,m} + \cdots , \tag{A16}$$

where '$\cdots$' denotes contributions from other terms, $a_1 = \Xi(1 - \tau_0)$, and the constants $I_{s-m,m}$ for the relevant values of s and m are given by

s \ m	-2	-1	0	1	2
0	0	0	0	0	0
1	$\frac{20}{21}$	$-\frac{8}{5}$	$\frac{4}{3}$	$\frac{8}{3}$	$-\frac{4}{15}$
2	$\frac{4}{3}$	$-\frac{4}{3}$	-4	4	$\frac{4}{3}$

First-order integrals $\overline{I^{(1)}_{j,nm}}^{s}$ and $\overline{J^{(1)}_{j,nm}}^{s}$

The first-order integrals are given by

$$\overline{I^{(1)}_{j,nm}}^{s} = \overline{L^3 e^{i(n+m)\phi} \int_0^{2\pi} d\chi \int_0^{\infty} d\zeta\, \zeta^2 \int_{-\pi}^{\pi} d\omega W_1 e^{i(m-n)\frac{\omega}{2}} \begin{pmatrix} \cos(\chi+\phi) \\ \sin(\chi+\phi) \end{pmatrix}_j}^{s}, \tag{A17}$$

$$\overline{J^{(1)}_{j,nm}}^{s} = \overline{L^3 e^{i(n+m)\phi} \int_0^{2\pi} d\chi \int_0^{\infty} d\zeta\, \zeta^2 \int_{-\pi}^{\pi} d\omega W_2 e^{-im\omega} \begin{pmatrix} \cos(\chi+\phi) \\ \sin(\chi+\phi) \end{pmatrix}_j}^{s}. \tag{A18}$$

Projection on the s-th Fourier mode is readily performed to give

$$\frac{1}{2\pi} \int_0^{2\pi} e^{-is\phi} e^{i(n+m)\phi} \begin{pmatrix} \cos(\chi+\phi) \\ \sin(\chi+\phi) \end{pmatrix} d\phi = \begin{bmatrix} \left(e^{i\chi}\delta_{n,s-m-1} + e^{-i\chi}\delta_{n,s-m+1}\right)/2 \\ \left(e^{i\chi}\delta_{n,s-m-1} - e^{-i\chi}\delta_{n,s-m+1}\right)/(2i) \end{bmatrix}, \tag{A19}$$

and, hence,

$$\overline{I^{(1)}_{j,nm}}^{s} = L^3 \int_0^{2\pi} d\chi \int_0^{\infty} d\zeta\, \zeta^2 \int_{-\pi}^{\pi} d\omega W_1 e^{i(m-n)\frac{\omega}{2}} \begin{bmatrix} \left(e^{i\chi}\delta_{n,s-m-1} + e^{-i\chi}\delta_{n,s-m+1}\right)/2 \\ \left(e^{i\chi}\delta_{n,s-m-1} - e^{-i\chi}\delta_{n,s-m+1}\right)/(2i) \end{bmatrix}_j, \tag{A20}$$

$$\overline{J^{(1)}_{j,nm}}^{s} = L^3 \int_0^{2\pi} d\chi \int_0^{\infty} d\zeta\, \zeta^2 \int_{-\pi}^{\pi} d\omega W_2 e^{-im\omega} \begin{bmatrix} \left(e^{i\chi}\delta_{n,s-m-1} + e^{-i\chi}\delta_{n,s-m+1}\right)/2 \\ \left(e^{i\chi}\delta_{n,s-m-1} - e^{-i\chi}\delta_{n,s-m+1}\right)/(2i) \end{bmatrix}_j . \tag{A21}$$

The spatial components of these integrals are conveniently expressed as

$$\overline{I^{(1)}_{x,nm}}^{s} = L^3 G a_2 \frac{B^{(1)}_{s,m}\delta_{n,s-m-1} + B^{(2)}_{s,m}\delta_{n,s-m+1}}{2}, \tag{A22}$$

$$\overline{I^{(1)}_{y,nm}}^{s} = L^3 G a_2 \frac{B^{(1)}_{s,m}\delta_{n,s-m-1} - B^{(2)}_{s,m}\delta_{n,s-m+1}}{2i}, \tag{A23}$$

$$\overline{J^{(1)}_{x,nm}}^{s} = L^3 G a_2 \frac{B^{(3)}_{s,m}\delta_{n,s-m-1} + B^{(3)}_{s,m}\delta_{n,s-m+1}}{2}, \tag{A24}$$

$$\overline{J^{(1)}_{y,nm}}^{s} = L^3 G a_2 \frac{B^{(4)}_{s,m}\delta_{n,s-m-1} - B^{(4)}_{s,m}\delta_{n,s-m+1}}{2i}, \tag{A25}$$

where $a_2 = \Xi\left(1-\tau_0^2\right)$, and $B^k_{s,m}$ are given by

$$B^{(1)}_{s,m} = G^{-1}\int_0^{2\pi} d\chi \int_0^{\infty} d\zeta\zeta^2 \int_{-\pi}^{\pi} d\omega W_1 e^{i(2m-s+1)\frac{\omega}{2}} e^{i\chi}, \tag{A26}$$

$$B^{(2)}_{s,m} = G^{-1}\int_0^{2\pi} d\chi \int_0^{\infty} d\zeta\zeta^2 \int_{-\pi}^{\pi} d\omega W_1 e^{i(2m-s-1)\frac{\omega}{2}} e^{-i\chi}, \tag{A27}$$

$$B^{(3)}_{s,m} = G^{-1}\int_0^{2\pi} d\chi \int_0^{\infty} d\zeta\zeta^2 \int_{-\pi}^{\pi} d\omega W_2 e^{-im\omega} e^{i\chi}, \tag{A28}$$

$$B^{(4)}_{s,m} = G^{-1}\int_0^{2\pi} d\chi \int_0^{\infty} d\zeta\zeta^2 \int_{-\pi}^{\pi} d\omega W_2 e^{-im\omega} e^{-i\chi}. \tag{A29}$$

Numerical evaluation of these coefficients for the relevant ranges of s and m yields

m	$B^{(1)}_{0,m}$	$B^{(2)}_{0,m}$	$B^{(3)}_{0,m}$	$B^{(4)}_{0,m}$	$B^{(1)}_{1,m}$	$B^{(2)}_{1,m}$	$B^{(3)}_{1,m}$	$B^{(4)}_{1,m}$	$B^{(1)}_{2,m}$	$B^{(2)}_{2,m}$	$B^{(3)}_{2,m}$	$B^{(4)}_{2,m}$
-2	$-\frac{1}{6}$	$-\frac{1}{6}$	$\frac{1}{6}$	$\frac{1}{6}$	—	—	—	—	$\frac{1}{6}$	$\frac{1}{30}$	$\frac{1}{6}$	$\frac{1}{6}$
-1	$-\frac{1}{2}$	$\frac{1}{6}$	$\frac{1}{2}$	$-\frac{1}{6}$	$-\frac{8}{15}$	—	$\frac{1}{2}$	—	$-\frac{1}{6}$	$-\frac{1}{6}$	$\frac{1}{2}$	$-\frac{1}{6}$
0	$\frac{1}{2}$	$\frac{1}{2}$	$-\frac{1}{2}$	$-\frac{1}{2}$	0	$\frac{8}{15}$	$-\frac{1}{2}$	$-\frac{1}{2}$	$-\frac{1}{2}$	$\frac{1}{6}$	$-\frac{1}{2}$	$-\frac{1}{2}$
1	$\frac{1}{6}$	$-\frac{1}{2}$	$-\frac{1}{6}$	$\frac{1}{2}$	$\frac{8}{15}$	0	$-\frac{1}{6}$	$\frac{1}{2}$	$\frac{1}{2}$	$\frac{1}{2}$	$-\frac{1}{6}$	$\frac{1}{2}$
2	$-\frac{1}{6}$	$-\frac{1}{6}$	$\frac{1}{6}$	$\frac{1}{6}$	—	$\frac{1}{6}$	—	$\frac{1}{6}$	$\frac{1}{6}$	$-\frac{1}{2}$	$\frac{1}{6}$	$\frac{1}{6}$

where hyphens denote coefficients that correspond to higher-order terms, neglected within both the ATC and QC closures. The contribution of the first-

order integrals to the evolution equation for P can now be written as

$$\partial_t P_s = L^3 G a_2 \sum_{n,m} \Bigg[B_m^{(1)} \delta_{n,s-m-1} \left(\frac{A_{x,nm}}{4} + \frac{A_{y,nm}}{4i} \right) + B_m^{(2)} \delta_{n,s-m+1} \left(\frac{A_{x,nm}}{4} - \frac{A_{y,nm}}{4i} \right) + B_m^{(3)} \delta_{n,s-m-1} P_n \left(\frac{\nabla_x P_m}{2} + \frac{\nabla_y P_m}{2i} \right) + B_m^{(4)} \delta_{n,s-m+1} P_n \left(\frac{\nabla_x P_m}{2} - \frac{\nabla_y P_m}{2i} \right) \Bigg]. \quad \text{(A30)}$$

Second-order integrals $\overline{I_{ij,nm}^{(2)}}^s$ and $\overline{J_{ij,nm}^{(2)}}^s$

The second-order integrals are given by

$$I_{ij,nm}^{(2)} = \overline{L^4 e^{i(n+m)\phi} \int_0^{2\pi} d\chi \int_0^{\infty} d\zeta\, \zeta^3 \int_{-\pi}^{\pi} d\omega W_1 e^{i(m-n)\frac{\omega}{2}} \begin{pmatrix} \cos(\chi+\phi) \\ \sin(\chi+\phi) \end{pmatrix}_i \begin{pmatrix} \cos(\chi+\phi) \\ \sin(\chi+\phi) \end{pmatrix}_j}^s, \quad \text{(A31)}$$

$$J_{ij,nm}^{(2)} = \overline{L^4 e^{i(n+m)\phi} \int_0^{2\pi} d\chi \int_0^{\infty} d\zeta\, \zeta^3 \int_{-\pi}^{\pi} d\omega W_2 e^{-im\omega} \begin{pmatrix} \cos(\chi+\phi) \\ \sin(\chi+\phi) \end{pmatrix}_i \begin{pmatrix} \cos(\chi+\phi) \\ \sin(\chi+\phi) \end{pmatrix}_j}^s. \quad \text{(A32)}$$

Projection on the s-th Fourier mode yields

$$\frac{1}{2\pi} \int_0^{2\pi} e^{is\phi} e^{i(n+m)\phi} \begin{pmatrix} \cos(\chi+\phi) \\ \sin(\chi+\phi) \end{pmatrix}_i \begin{pmatrix} \cos(\chi+\phi) \\ \sin(\chi+\phi) \end{pmatrix}_j d\phi = \begin{pmatrix} \frac{e^{2\chi}\delta_{n,s-m-2} + 2\delta_{n,s-m} + e^{-2\chi}\delta_{n,s-m+2}}{4} & \frac{e^{2\chi}\delta_{n,s-m-2} - e^{-2\chi}\delta_{n,s-m+2}}{4i} \\ \frac{e^{2\chi}\delta_{n,s-m-2} - e^{-2\chi}\delta_{n,s-m+2}}{4i} & -\frac{e^{2\chi}\delta_{n,s-m-2} - 2\delta_{n,s-m} + e^{-2\chi}\delta_{n,s-m+2}}{4} \end{pmatrix}. \quad \text{(A33)}$$

The spatial components of the second-order integrals are expressed as

$$\overline{I_{xx,nm}^{(2)}}^s = L^4 G(1+a_3) \frac{B_{s,m}^{(1)}\delta_{n,s-m-2} + 2B_{s,m}^{(2)}\delta_{n,s-m} + B_{s,m}^{(3)}\delta_{n,s-m+2}}{4}, \quad \text{(A34)}$$

$$\overline{I_{xy,nm}^{(2)}}^s = \overline{I_{yx,nm}^{(2)}}^s = L^4 G(1+a_3) \frac{B_{s,m}^{(1)}\delta_{n,s-m-2} - B_{s,m}^{(3)}\delta_{n,s-m+2}}{4i}, \quad \text{(A35)}$$

$$\overline{I_{yy,nm}^{(2)}}^s = -L^4 G(1+a_3) \frac{B_{s,m}^{(1)}\delta_{n,s-m-2} - 2B_{s,m}^{(2)}\delta_{n,s-m} + B_{s,m}^{(3)}\delta_{n,s-m+2}}{4}, \quad \text{(A36)}$$

$$\overline{J_{xx,nm}^{(2)}}^s = L^4 G(1+a_3) \frac{B_{s,m}^{(4)}\delta_{n,s-m-2} + 2B_{s,m}^{(5)}\delta_{n,s-m} + B_{s,m}^{(6)}\delta_{n,s-m+2}}{4}, \quad \text{(A37)}$$

$$\overline{J_{xy,nm}^{(2)}}^s = \overline{J_{yx,nm}^{(2)}}^s = L^4 G(1+a_3) \frac{B_{s,m}^{(4)}\delta_{n,s-m-2} - B_{s,m}^{(6)}\delta_{n,s-m+2}}{4i}, \quad \text{(A38)}$$

$$\overline{J_{yy,nm}^{(2)}}^s = -L^4 G(1+a_3) \frac{B_{s,m}^{(4)}\delta_{n,s-m-2} - 2B_{s,m}^{(5)}\delta_{n,s-m} + B_{s,m}^{(6)}\delta_{n,s-m+2}}{4}, \quad \text{(A39)}$$

where $a_3 = \Xi\left(1 - \frac{\tau_0(1+\tau_0^2)}{2}\right)$, and the coefficients $B^k_{s,m}$ are given by

$$B^{(1)}_{s,m} = G^{-1}\int_0^{2\pi} d\chi \int_0^{\infty} d\zeta\zeta^3 \int_{-\pi}^{\pi} d\omega W_1 e^{i(2m-s+2)\frac{\omega}{2}} e^{i2\chi}, \tag{A40}$$

$$B^{(2)}_{s,m} = G^{-1}\int_0^{2\pi} d\chi \int_0^{\infty} d\zeta\zeta^3 \int_{-\pi}^{\pi} d\omega W_1 e^{i(2m-s)\frac{\omega}{2}}, \tag{A41}$$

$$B^{(3)}_{s,m} = G^{-1}\int_0^{2\pi} d\chi \int_0^{\infty} d\zeta\zeta^3 \int_{-\pi}^{\pi} d\omega W_1 e^{i(2m-s-2)\frac{\omega}{2}} e^{-i2\chi}, \tag{A42}$$

$$B^{(4)}_{s,m} = G^{-1}\int_0^{2\pi} d\chi \int_0^{\infty} d\zeta\zeta^3 \int_{-\pi}^{\pi} d\omega W_2 e^{-im\omega} e^{i2\chi}, \tag{A43}$$

$$B^{(5)}_{s,m} = G^{-1}\int_0^{2\pi} d\chi \int_0^{\infty} d\zeta\zeta^3 \int_{-\pi}^{\pi} d\omega W_2 e^{-im\omega}, \tag{A44}$$

$$B^{(6)}_{s,m} = G^{-1}\int_0^{2\pi} d\chi \int_0^{\infty} d\zeta\zeta^3 \int_{-\pi}^{\pi} d\omega W_2 e^{-im\omega} e^{-i2\chi}. \tag{A45}$$

Numerical evaluation of these coefficients for the relevant ranges of s and m yields

m	$B^{(1)}_{0,m}$	$B^{(2)}_{0,m}$	$B^{(3)}_{0,m}$	$B^{(4)}_{0,m}$	$B^{(5)}_{0,m}$	$B^{(6)}_{0,m}$
-2	$\frac{2}{9}$	$-\frac{2}{15}$	$-\frac{2}{9}$	$\frac{2}{9}$	$-\frac{2}{15}$	$-\frac{2}{9}$
-1	0	0	0	0	0	0
0	$\frac{2}{9}$	$\frac{2}{9}$	$\frac{2}{3}$	$\frac{2}{9}$	$\frac{2}{9}$	$\frac{2}{3}$
1	0	0	0	0	0	0
2	$-\frac{2}{15}$	$\frac{2}{9}$	$-\frac{2}{9}$	$-\frac{2}{15}$	$\frac{2}{9}$	$-\frac{2}{9}$
m	$B^{(1)}_{1,m}$	$B^{(2)}_{1,m}$	$B^{(3)}_{1,m}$	$B^{(4)}_{1,m}$	$B^{(5)}_{1,m}$	$B^{(6)}_{1,m}$
-2	—	—	—	—	—	—
-1	$\frac{67}{750}$	—	—	0	0	0
0	$\frac{67}{750}$	—	$\frac{4}{9}$	$\frac{2}{9}$	—	$\frac{2}{3}$
1	—	—	$\frac{4}{9}$	—	—	0
2	—	—	—	—	—	—
m	$B^{(1)}_{2,m}$	$B^{(2)}_{2,m}$	$B^{(3)}_{2,m}$	$B^{(4)}_{2,m}$	$B^{(5)}_{2,m}$	$B^{(6)}_{2,m}$
-2	0	—	—	$\frac{2}{9}$	—	—
-1	0	0	0	0	0	0
0	$\frac{1}{3}$	—	$\frac{1}{3}$	$\frac{2}{9}$	—	$\frac{2}{3}$
1	0	0	0	0	0	0
2	0	$\frac{1}{3}$	$\frac{1}{3}$	$-\frac{2}{15}$	$\frac{2}{9}$	$-\frac{2}{9}$

,

where hyphens denote coefficients that correspond to higher-order terms, neglected within both the ATC and QC closures. The contribution of the second-order integrals to the evolution equation for P is given by

$$\begin{aligned}\partial_t P_s =& L^4 G\,(1+a_3)\sum_{n,m}\left[B^{(1)}_{s,m}\delta_{n,s-m-2}\frac{1}{8}\left(\frac{A_{xx,nm}-A_{yy,nm}}{4}+\frac{A_{xy,nm}+A_{yx,nm}}{4i}\right)\right.\\ &\left.+\,B^{(2)}_{s,m}\delta_{n,s-m}\frac{A_{xx,nm}+A_{yy,nm}}{16}\right.\end{aligned}$$

$$
\begin{aligned}
&+ B^{(3)}_{s,m}\delta_{n,s-m+2}\frac{1}{8}\left(\frac{A_{xx,nm}-A_{yy,nm}}{4}+\frac{A_{xy,nm}+A_{yx,nm}}{4i}\right)\\
&+ B^{(4)}_{s,m}\delta_{n,s-m-2}P_n\left(\frac{\nabla_x\nabla_y 2P_m-\nabla_y^2P_m}{4}+\frac{\nabla_x\nabla_y P_m}{2i}\right)\\
&+ B^{(5)}_{s,m}\delta_{n,s-m}P_n\frac{\nabla_x^2P_m-\nabla_y^2P_m}{4}\\
&+ B^{(6)}_{s,m}\delta_{n,s-m+2}P_n\left(\frac{\nabla_x\nabla_y 2P_m-\nabla_y^2P_m}{4}+\frac{\nabla_x\nabla_y P_m}{2i}\right)\Bigg].
\end{aligned}
\tag{A46}
$$

Third-order integrals $\overline{I^{(3)}_{ijk,nm}}^{s}$ and $\overline{J^{(3)}_{ijk,nm}}^{s}$

The third-order integrals are given by

$$
\begin{aligned}
\overline{I^{(3)}_{ijk,nm}}^{s} =&\overline{L^5e^{i(n+m)\phi}\int_0^{2\pi}d\chi\int_0^{\infty}\zeta^4d\zeta}\\
&\overline{\times\int_{-\pi}^{\pi}d\omega e^{i(m-n)\frac{\omega}{2}}W_1\begin{pmatrix}\cos(\chi+\phi)\\ \sin(\chi+\phi)\end{pmatrix}_i\begin{pmatrix}\cos(\chi+\phi)\\ \sin(\chi+\phi)\end{pmatrix}_j\begin{pmatrix}\cos(\chi+\phi)\\ \sin(\chi+\phi)\end{pmatrix}_k}^{s},
\end{aligned}
\tag{A47}
$$

$$
\begin{aligned}
\overline{J^{(3)}_{ijk,nm}}^{s} =&\overline{L^5e^{i(n+m)\phi}\int_0^{2\pi}d\chi\int_0^{\infty}\zeta^4d\zeta}\\
&\overline{\times\int_{-\pi}^{\pi}d\omega e^{-im\omega}W_2\begin{pmatrix}\cos(\chi+\phi)\\ \sin(\chi+\phi)\end{pmatrix}_i\begin{pmatrix}\cos(\chi+\phi)\\ \sin(\chi+\phi)\end{pmatrix}_j\begin{pmatrix}\cos(\chi+\phi)\\ \sin(\chi+\phi)\end{pmatrix}_k}^{s}.
\end{aligned}
\tag{A48}
$$

We do not need to calculate all of these integrals as most of them correspond to high-order terms, neglected within both the ATC and QC closures. As can be seen from Eq.2.5 of the main text, $\overline{I^{(3)}_{ijk,nm}}^{s}$ and $\overline{J^{(3)}_{ijk,nm}}^{s}$ only contribute to the density equation, i.e., we only need to evaluate them for $s=0$. Performing projection on the $s=0$ mode yields straightforward but cumbersome expressions that we omit here. Inserting the results of the projection into Eq.2.5 of the main text and re-arranging the terms gives the following expression for the contribution of the third-order terms to the equation for $s=0$

$$
\begin{aligned}
\partial_t P_0 =&\frac{1}{48}L^5Ga_4\sum_{n,m}\Bigg[\frac{1}{8}B^{(1)}_m\Big\{3A_{xxx,nm}-i\left(A_{xxy,nm}+A_{xyx,nm}+A_{yxx,nm}\right)\\
&+\left(A_{xyy,nm}+A_{yxy,nm}+A_{yyx,nm}\right)-3iA_{yyy,nm}\Big\}\delta_{n,-m-1}\\
&+\frac{1}{8}B^{(2)}_m\Big\{3A_{xxx,nm}+i\left(A_{xxy,nm}+A_{xyx,nm}+A_{yxx,nm}\right)\\
&+\left(A_{xyy,nm}+A_{yxy,nm}+A_{yyx,nm}\right)+3iA_{yyy,nm}\Big\}\delta_{n,-m+1}\\
&+3B^{(3)}_mP_n\Big\{\nabla_x^3P_m-i\nabla_x^2\nabla_yP_m+\nabla_x\nabla_y^2P_m-i\nabla_y^3P_m\Big\}\delta_{n,-m-1}
\end{aligned}
\tag{A49}
$$

$$+ 3B_m^{(4)} P_n \Big\{ \nabla_x^3 P_m + i\nabla_x^2 \nabla_y P_m + \nabla_x \nabla_y^2 P_m + i\nabla_y^3 P_m \Big\} \delta_{n,-m+1} \Bigg],$$

where $a_4 = \Xi\left(1 - \frac{\tau_0^2\left(1+\tau_0^2\right)}{2}\right)$, and we have omitted terms proportional to $\delta_{n,-m\pm3}$ since they also correspond to higher-order terms. The constants $B_m^{(k)}$ are given by

$$B_m^{(1)} = G^{-1} \int_0^{2\pi} d\chi \int_0^{\infty} d\zeta \zeta^4 \int_{-\pi}^{\pi} d\omega W_1 e^{i(2m+1)\frac{\omega}{2}} e^{i\chi}, \tag{A50}$$

$$B_m^{(2)} = G^{-1} \int_0^{2\pi} d\chi \int_0^{\infty} d\zeta \zeta^4 \int_{-\pi}^{\pi} d\omega W_1 e^{i(2m-1)\frac{\omega}{2}} e^{-i\chi}, \tag{A51}$$

$$B_m^{(3)} = G^{-1} \int_0^{2\pi} d\chi \int_0^{\infty} d\zeta \zeta^4 \int_{-\pi}^{\pi} d\omega W_2 e^{-im\omega} e^{i\chi}, \tag{A52}$$

$$B_m^{(4)} = G^{-1} \int_0^{2\pi} d\chi \int_0^{\infty} d\zeta \zeta^4 \int_{-\pi}^{\pi} d\omega W_2 e^{-im\omega} e^{-i\chi}, \tag{A53}$$

and the relevant values are

$$-B_{-1}^{(1)} = B_0^{(1)} = B_0^{(2)} = -B_1^{(2)} = B_{-1}^{(3)} = -B_0^{(3)} = -B_0^{(4)} = B_1^{(4)} = \frac{2}{15}. \tag{A54}$$

Fourth-order integrals $\overline{I_{ijkl,nm}^{(4)}}^s$ and $\overline{J_{ijkl,nm}^{(4)}}^s$: coefficient of the bilaplacian term

The fourth order integrals are given by

$$\overline{I_{ijkl,nm}^{(4)}}^s = \overline{L^6 e^{i(n+m)\phi} \int_0^{2\pi} d\chi \int_0^{\infty} \zeta^5 d\zeta} \Bigg/ \overline{\times \int_{-\pi}^{\pi} d\omega e^{i(m-n)\frac{\omega}{2}} W_1 \begin{pmatrix} \cos(\chi+\phi) \\ \sin(\chi+\phi) \end{pmatrix}_i \begin{pmatrix} \cos(\chi+\phi) \\ \sin(\chi+\phi) \end{pmatrix}_j \begin{pmatrix} \cos(\chi+\phi) \\ \sin(\chi+\phi) \end{pmatrix}_k \begin{pmatrix} \cos(\chi+\phi) \\ \sin(\chi+\phi) \end{pmatrix}_l}^s, \tag{A55}$$

$$\overline{J_{ijkl,nm}^{(4)}}^s = \overline{L^6 e^{i(n+m)\phi} \int_0^{2\pi} d\chi \int_0^{\infty} \zeta^5 d\zeta} \Bigg/ \overline{\times \int_{-\pi}^{\pi} d\omega e^{-im\omega} W_2 \begin{pmatrix} \cos(\chi+\phi) \\ \sin(\chi+\phi) \end{pmatrix}_i \begin{pmatrix} \cos(\chi+\phi) \\ \sin(\chi+\phi) \end{pmatrix}_j \begin{pmatrix} \cos(\chi+\phi) \\ \sin(\chi+\phi) \end{pmatrix}_k \begin{pmatrix} \cos(\chi+\phi) \\ \sin(\chi+\phi) \end{pmatrix}_l}^s. \tag{A56}$$

As noted in the main text, the only purpose of keeping such high-order terms is to ensure that there is a lengthscale selection for the density instability, which is provided by the bilaplacian term in Eqs.(50) and (57) of the main text. Therefore, the only relevant fourth-order integrals are $\overline{I_{ijkl,00}^{(4)}}^0$ and $\overline{J_{ijkl,00}^{(4)}}^0$. Using the same method as for lower-order integrals above, we obtain

$$
\begin{aligned}
&\overline{I^{(4)}_{xxxx,00}}^{0} = \overline{I^{(4)}_{yyyy,00}}^{0} = L^6 G(1+a_5)\frac{3}{8}B^{(1)},\\
&\overline{I^{(4)}_{xxyy,00}}^{0} = \overline{I^{(4)}_{xyxy,00}}^{0} = \overline{I^{(4)}_{xyyx,00}}^{0} =\\
&\overline{I^{(4)}_{yxxy,00}}^{0} = \overline{I^{(4)}_{yxyx,00}}^{0} = \overline{I^{(4)}_{yyxx,00}}^{0} = L^6 G(1+a_5)\frac{1}{8}B^{(1)},\\
&\overline{J^{(4)}_{xxxx,00}}^{0} = \overline{J^{(4)}_{yyyy,00}}^{0} = L^6 G(1+a_5)\frac{3}{8}B^{(2)},\\
&\overline{J^{(4)}_{xxyy,00}}^{0} = \overline{J^{(4)}_{xyxy,00}}^{0} = \overline{J^{(4)}_{xyyx,00}}^{0} =\\
&\overline{J^{(4)}_{yxxy,00}}^{0} = \overline{J^{(4)}_{yxyx,00}}^{0} = \overline{J^{(4)}_{yyxx,00}}^{0} = L^6 G(1+a_5)\frac{1}{8}B^{(2)},
\end{aligned}
\tag{A57}
$$

where $a_5 = \Xi\left(1 - \frac{\tau_0(1+\tau_0^2)^2}{4}\right)$, and

$$
B^{(1)} = G^{-1}\int_0^{2\pi} d\chi \int d\zeta \zeta^5 \int_{-\pi}^{\pi} d\omega\, W_1 = \frac{26}{135}, \tag{A58}
$$

$$
B^{(2)} = G^{-1}\int_0^{2\pi} d\chi \int d\zeta \zeta^5 \int_{-\pi}^{\pi} d\omega\, W_2 = \frac{26}{135}. \tag{A59}
$$

Stability Analysis

AT closure (ATC)

$$\begin{aligned}\partial_t\delta\rho =&A\delta\rho + B_i m_i,\\ \partial_t m_i =&C_i\delta\rho + D_{ij}m_j,\end{aligned} \tag{A60}$$

$$\begin{aligned}A =&\left[-\frac{1}{32}+\frac{(1+a_3)\rho_0}{24\pi}-\frac{\alpha\rho_0}{192\pi}e^{\frac{\alpha\rho_0}{6}}\left(12+\alpha\rho_0\right)-\frac{91(1+a_5)\rho_0}{69120\pi}k^2+\frac{a_4}{80}ik_xP\right]k^2,\\ B_i =&-\frac{a_4}{80}ik^2k_i\rho_0,\\ C_i =&-\frac{a_2}{16\pi^2}ik_i\rho_0+\frac{2(1+a_1)}{3\pi}P\delta_{ix},\\ D_{ij} =&\delta_{ij}\left[-1-\frac{5k^2}{192}+\frac{2(1+a_1)}{3\pi}\rho_0-\frac{(1+a_3)}{40\pi}k^2\rho_0+a_2\frac{9}{20}ik_xP\right]\\ &+\left[-\frac{1}{96}-\frac{(1+a_3)}{180\pi}\rho_0\right]k_ik_j-\frac{28}{15}(1+a_1)A_0P^2\left(\delta_{ij}+2\delta_{ix}\delta_{jx}\right)\\ &+a_2\frac{i}{20}P\delta_{ix}k_j-a_2\frac{i}{12}Pk_i\delta_{jx},\end{aligned} \tag{A61}$$

New closure with Q_{ij} (QC)

$$\begin{aligned}\partial_t\delta\rho =&A\delta\rho + B_i m_i + C_{ij}\delta Q_{ij},\\ \partial_t m_i =&D_i\delta\rho + E_{ij}m_j + F_j\delta Q_{ij},\end{aligned} \tag{A62}$$

$$\begin{aligned}A =&\left[-\frac{1}{32}+\frac{(1+a_3)\rho_0}{24\pi}-\frac{\alpha\rho_0}{192\pi}e^{\frac{\alpha\rho_0}{6}}\left(12+\alpha\rho_0\right)-\frac{91(1+a_5)\rho_0}{69120\pi}k^2\right]k^2,\\ B_i =&-\frac{a_4}{80}ik^2k_i\rho_0,\\ C_{ij} =&-\left[\frac{\pi}{48}-\frac{1}{36}\left(1+a_3\right)\rho_0\right]k_ik_j,\quad D_i=-\frac{a_2}{16\pi^2}ik_i\rho_0+\frac{2(1+a_1)}{3\pi}P\delta_{ix},\\ E_{ij} =&\delta_{ij}\left[-1-\frac{5k^2}{192}+\frac{2(1+a_1)}{3\pi}\rho_0-\frac{(1+a_3)}{40\pi}k^2\rho_0+a_2\frac{9}{20}ik_xP\right]\\ &+\left[-\frac{1}{96}-\frac{(1+a_3)}{180\pi}\rho_0\right]k_ik_j\\ &-\frac{28}{15}(1+a_1)W_{ij}+a_2\frac{i}{20}P\delta_{ix}k_j-a_2\frac{i}{12}Pk_i\delta_{jx},\\ F_j =&-(1+a_1)\frac{28}{15}P\delta_{jx}-\frac{a_2\rho_0}{240}ik_j,\end{aligned} \tag{A63}$$

Where:

$$\delta Q_{ij} =\frac{1}{1+\frac{\rho_0}{3\pi}(1+a_1)}\Big[2P(1+a_1)\left(m_i\delta_{jx}+\delta_{ix}m_j-\delta_{ij}m_x\right)$$

$$+\frac{a_2\rho_0 i}{48\pi}\left(k_i m_j + k_j m_i - \delta_{ij} m_l k_l\right)\Bigg],$$

$$W_{xx} = -W_{yy} = \frac{15}{28}\frac{\frac{2}{3\pi}\rho_0(1+a_1)-1}{1+a_1},$$

$$W_{xy} = 0,$$

Appendix B

Interaction integrals

Below we describe evaluation of the interaction integrals necessary to derive hydordynamic equations from Eq.3.6 in Chapter 3. All integrals are expressed in terms of auxiliary variables $\chi = \psi - \phi$ and $\boldsymbol{\zeta} = \boldsymbol{\xi}/L$. The interaction kernels W_1 $\tilde{W}_1$ and W_2, defined in Chapter 3, can, therefore, be written as

$$
\begin{aligned}
W_1 =& G\,\Theta\Big(|\sin\omega| - 2\zeta\left|\chi + \frac{\omega}{2}\right|\Big)\,\Theta\Big(|\sin\omega| - 2\zeta\left|\chi - \frac{\omega}{2}\right|\Big) \\
&\times\left\{1 + \Xi\left[\Theta\left(2\zeta\frac{\sin\left(-\chi-\frac{\omega}{2}\right)}{\sin\omega} - \tau_0\right) + \Theta\left(2\zeta\frac{\sin\left(-\chi+\frac{\omega}{2}\right)}{\sin\omega} - \tau_0\right)\right]\right\}, \\
\tilde{W}_1 =& G\,\Theta\Big(|\sin\omega| - 2\zeta\left|\chi + \frac{\omega}{2} - \frac{\pi}{2}\right|\Big)\,\Theta\Big(|\sin\omega| - 2\zeta\left|\chi - \frac{\omega}{2} - \frac{\pi}{2}\right|\Big) \\
&\times\left\{1 + \Xi\left[\Theta\left(2\zeta\frac{\sin\left(-\chi-\frac{\omega}{2}+\frac{\pi}{2}\right)}{\sin\omega} - \tau_0\right)\right.\right. \\
&\qquad\left.\left. + \Theta\left(2\zeta\frac{\sin\left(-\chi+\frac{\omega}{2}+\frac{\pi}{2}\right)}{\sin\omega} - \tau_0\right)\right]\right\}, \\
W_2 =& G\,\Theta(|\sin\omega| - 2\zeta\,|\chi|)\,\Theta(|\sin\omega| - 2\zeta\,|\chi+\omega|) \\
&\times\left\{1 + \Xi\left[\Theta\left(2\zeta\frac{\sin\left(-\chi\right)}{\sin\omega} - \tau_0\right) + \Theta\left(2\zeta\frac{\sin\left(-\chi-\omega\right)}{\sin\omega} - \tau_0\right)\right]\right\},
\end{aligned}
\tag{B1}
$$

Term $T^{(1)}_{nm}$

Term $T^{(1)}_{nm}$ is proportional to the zeroth order of $\boldsymbol{\xi}$ and $\mathbf{n}$. It ontains three parts corresponding to $\overline{I^{(0)}_{nm}}^{\,s}$, $\overline{\tilde{I}^{(0)}_{nm}}^{\,s}$ and $\overline{J^{(0)}_{nm}}^{\,s}$. Again, all integrals are expressed in terms of auxiliary variables $\chi = \psi - \phi$ and $\boldsymbol{\zeta} = \boldsymbol{\xi}/L$.

The zeroth-order integrals are given by Eqs.3.9, 3.10, 3.12 :

$$
\begin{aligned}
\overline{I^{(0)}_{nm}}^{\,s} =& \overline{e^{i(n+m)\phi}L^2\int_0^{2\pi}d\chi\int_0^{\infty}d\zeta\,\zeta\int_{-\pi/2}^{\pi/2}d\omega\,W_1 e^{i(m-n)\frac{\omega}{2}}}^{\,s}, \\
\overline{\tilde{I}^{(0)}_{nm}}^{\,s} =& \overline{e^{i(n+m)\phi}L^2\int_0^{2\pi}d\chi\int_0^{\infty}d\zeta\,\zeta\int_{-\pi/2}^{\pi/2}d\omega\,\tilde{W}_1 e^{i(m-n)\frac{\omega}{2}}e^{i(m+n)\frac{\pi}{2}}}^{\,s}, \\
\overline{J^{(0)}_{nm}}^{\,s} =& \overline{e^{i(n+m)\phi}L^2\int_0^{2\pi}d\chi\int_0^{\infty}d\zeta\,\zeta\int_{-\pi}^{\pi}d\omega\,W_2 e^{-im\omega}}^{\,s}.
\end{aligned}
\tag{B2}
$$

$$
\begin{aligned}
\overline{I^{(0)}_{j,nm}}^{\,s} =& \delta_{n,s-m}L^2\int_0^{2\pi}d\chi\int_0^{\infty}d\zeta\,\zeta\int_{-\pi/2}^{\pi/2}d\omega W_1 e^{i(m-n)\frac{\omega}{2}}, \\
\overline{\tilde{I}^{(0)}_{j,nm}}^{\,s} =& \delta_{n,s-m}L^2\int_0^{2\pi}d\chi\int_0^{\infty}d\zeta\,\zeta\int_{\frac{\pi}{2}}^{\frac{3\pi}{2}}d\omega\tilde{W}_1 e^{i(m-n)\frac{\omega}{2}}e^{i(m+n)\frac{\pi}{2}},
\end{aligned}
$$

$$\overline{J^{(0)}_{j,nm}}^{s} = \delta_{n,s-m} L^2 \int_0^{2\pi} d\chi \int_0^{\infty} d\zeta\, \zeta \int_{-\pi}^{\pi} d\omega W_2 e^{-im\omega}. \tag{B3}$$

Evaluating these integrals numerically, we observe that:

$$T^{(1)}_{nm} = \sum_{n,m} \left[\overline{I^{(0)}_{j,nm}}^{s} + \overline{\tilde{I}^{(0)}_{j,nm}}^{s} - \overline{J^{(0)}_{j,nm}}^{s} \right] P_n P_m = GL^2 (1 + a_1) \sum_m P_{s-m} P_m I_{s-m,m}, \tag{B4}$$

where $a_1 = \Xi(1 - \tau_0)$, and the constants $I_{s-m,m}$ for the relevant values of s and m are given by

s \ m	-4	-3	-2	-1	0	1	2	3	4
0	0	0	0	0	0	0	0	0	0
1	—	0	$-\frac{7}{9}$	0	$-\frac{6}{11}$	0	$\frac{29}{19}$	0	$-\frac{24}{25}$
2	—	—	$-\frac{2}{3}$	0	-2	0	$\frac{10}{3}$	0	$-\frac{26}{15}$
3	—	—	—	0	$-\frac{19}{15}$	0	$\frac{24}{5}$	0	$-\frac{46}{25}$
4	—	—	—	—	$-\frac{16}{3}$	0	$\frac{16}{3}$	0	$-\frac{16}{15}$

where hyphens denote coefficients that correspond to higher-order terms, neglected within the closures.

Term $T^{(2)}_{i,nm}$

According to (3.15):

$$T^{(2)}_{i,nm} = \sum_{n,m=-\infty}^{\infty} \left[\frac{1}{2} \overline{I^{(1)}_{i,nm}}^{s} A_{i,nm} + \frac{1}{2} \overline{\tilde{I}^{(1)}_{i,nm}}^{s} A_{i,nm} + \overline{J^{(1)}_{i,nm}}^{s} P_n \nabla_i P_m \right]. \tag{B5}$$

Relevant integrals are given by

$$\begin{aligned}
\overline{I^{(1)}_{j,nm}}^{s} &= \overline{L^3 e^{i(n+m)\phi} \int_0^{2\pi} d\chi \int_0^{\infty} d\zeta\, \zeta^2 \int_{-\pi}^{\pi} d\omega W_1 e^{i(m-n)\frac{\omega}{2}} \begin{pmatrix} \cos(\chi+\phi) \\ \sin(\chi+\phi) \end{pmatrix}_j}^{s}, \\
\overline{\tilde{I}^{(1)}_{j,nm}}^{s} &= \overline{L^3 e^{i(n+m)\phi} \int_0^{2\pi} d\chi \int_0^{\infty} d\zeta\, \zeta^2 \int_{\frac{\pi}{2}}^{\frac{3\pi}{2}} d\omega \tilde{W}_1 e^{i(m-n)\frac{\omega}{2}} e^{i(m+n)\frac{\pi}{2}} \begin{pmatrix} \cos(\chi+\phi) \\ \sin(\chi+\phi) \end{pmatrix}_j}^{s}, \\
\overline{J^{(1)}_{j,nm}}^{s} &= \overline{L^3 e^{i(n+m)\phi} \int_0^{2\pi} d\chi \int_0^{\infty} d\zeta\, \zeta^2 \int_{-\pi}^{\pi} d\omega W_2 e^{-im\omega} \begin{pmatrix} \cos(\chi+\phi) \\ \sin(\chi+\phi) \end{pmatrix}_j}^{s}.
\end{aligned} \tag{B6}$$

Projection on the s-th Fourier mode yields:

$$\begin{aligned}
\overline{I^{(1)}_{j,nm}}^{s} =& L^3 \int_0^{2\pi} d\chi \int_0^{\infty} d\zeta\, \zeta^2 \int_{-\pi}^{\pi} d\omega W_1 e^{i(m-n)\frac{\omega}{2}} \\
& \times \begin{bmatrix} \left(e^{i\chi}\delta_{n,s-m-1} + e^{-i\chi}\delta_{n,s-m+1}\right)/2 \\ \left(e^{i\chi}\delta_{n,s-m-1} - e^{-i\chi}\delta_{n,s-m+1}\right)/(2i) \end{bmatrix}_j , \\
\overline{\tilde{I}^{(1)}_{j,nm}}^{s} =& L^3 \int_0^{2\pi} d\chi \int_0^{\infty} d\zeta\, \zeta^2 \int_{\frac{\pi}{2}}^{\frac{3\pi}{2}} d\omega \tilde{W}_1 e^{i(m-n)\frac{\omega}{2}} e^{i(m+n)\frac{\pi}{2}} \\
& \times \begin{bmatrix} \left(e^{i\chi}\delta_{n,s-m-1} + e^{-i\chi}\delta_{n,s-m+1}\right)/2 \\ \left(e^{i\chi}\delta_{n,s-m-1} - e^{-i\chi}\delta_{n,s-m+1}\right)/(2i) \end{bmatrix}_j , \\
\overline{J^{(1)}_{j,nm}}^{s} =& L^3 \int_0^{2\pi} d\chi \int_0^{\infty} d\zeta\, \zeta^2 \int_{-\pi}^{\pi} d\omega W_2 e^{-im\omega} \begin{bmatrix} \left(e^{i\chi}\delta_{n,s-m-1} + e^{-i\chi}\delta_{n,s-m+1}\right)/2 \\ \left(e^{i\chi}\delta_{n,s-m-1} - e^{-i\chi}\delta_{n,s-m+1}\right)/(2i) \end{bmatrix}_j .
\end{aligned} \tag{B7}$$

The spatial components of these integrals are conveniently expressed as

$$\begin{aligned}
\overline{I^{(1)}_{x,nm}}^{s} + \overline{\tilde{I}^{(1)}_{x,nm}}^{s} &= L^3 G a_2 \frac{S^{(1)}_{s,m}\delta_{n,s-m-1} + S^{(2)}_{s,m}\delta_{n,s-m+1}}{2}, \\
\overline{I^{(1)}_{y,nm}}^{s} + \overline{\tilde{I}^{(1)}_{y,nm}}^{s} &= L^3 G a_2 \frac{S^{(1)}_{s,m}\delta_{n,s-m-1} - S^{(2)}_{s,m}\delta_{n,s-m+1}}{2i}, \\
\overline{J^{(1)}_{x,nm}}^{s} &= L^3 G a_2 \frac{S^{(3)}_{s,m}\delta_{n,s-m-1} + S^{(3)}_{s,m}\delta_{n,s-m+1}}{2}, \\
\overline{J^{(1)}_{y,nm}}^{s} &= L^3 G a_2 \frac{S^{(4)}_{s,m}\delta_{n,s-m-1} - S^{(4)}_{s,m}\delta_{n,s-m+1}}{2i},
\end{aligned} \tag{B8}$$

where $a_2 = \Xi\,(1-\tau_0^2)$. Numerical evaluation of the coefficients $S^k_{s,m}$ for the relevant ranges of s and m yields

m	$S^{(1)}_{1,m}$	$S^{(2)}_{1,m}$	$S^{(3)}_{1,m}$	$S^{(4)}_{1,m}$	$S^{(1)}_{2,m}$	$S^{(2)}_{2,m}$	$S^{(3)}_{2,m}$	$S^{(4)}_{2,m}$
-2	$-\frac{4}{15}$	$-\frac{4}{15}$	$\frac{1}{6}$	$\frac{1}{6}$	$-\frac{1}{4}$	$-\frac{1}{4}$	$\frac{1}{6}$	$\frac{1}{6}$
-1	$-\frac{4}{9}$	$\frac{4}{15}$	$\frac{1}{2}$	$-\frac{1}{6}$	$-\frac{1}{4}$	$\frac{1}{4}$	$\frac{1}{2}$	$-\frac{1}{6}$
0	$\frac{4}{9}$	$\frac{4}{9}$	$-\frac{1}{2}$	$-\frac{1}{2}$	$\frac{3}{11}$	$\frac{1}{4}$	$-\frac{1}{2}$	$-\frac{1}{2}$
1	$-\frac{1}{36}$	$-\frac{4}{9}$	$-\frac{1}{6}$	$\frac{1}{2}$	$-\frac{1}{4}$	$-\frac{1}{4}$	$-\frac{1}{6}$	$\frac{1}{2}$
2	$\frac{1}{36}$	$\frac{1}{36}$	$\frac{1}{6}$	$\frac{1}{6}$	$\frac{1}{4}$	$-\frac{3}{11}$	$\frac{1}{6}$	$\frac{1}{6}$

.

The contribution of described integrals to the evolution equation for P_s can

now be written as

$$T^{(2)}_{i,nm} = L^3 G a_2 \sum_{n,m} \left[S^{(1)}_m \delta_{n,s-m-1} \left(\frac{A_{x,nm}}{4} + \frac{A_{y,nm}}{4i} \right) + S^{(2)}_m \delta_{n,s-m+1} \left(\frac{A_{x,nm}}{4} - \frac{A_{y,nm}}{4i} \right) \right.$$

$$\left. + S^{(3)}_m \delta_{n,s-m-1} P_n \left(\frac{\nabla_x P_m}{2} + \frac{\nabla_y P_m}{2i} \right) + S^{(4)}_m \delta_{n,s-m+1} P_n \left(\frac{\nabla_x P_m}{2} - \frac{\nabla_y P_m}{2i} \right) \right]. \tag{B9}$$

Term $T^{(3)}_{ij,nm}$

This term is proportional to ξ^2 and n^0. It contains second-order integrals $\overline{I^{(2)}_{ij,nm}}^s$, $\overline{\tilde{I}^{(2)}_{ij,nm}}^s$ and $\overline{J^{(2)}_{ij,nm}}^s$. Integrals are given by

$$\overline{I^{(2)}_{ij,nm}}^s = \overline{L^4 e^{i(n+m)\phi} \int_0^{2\pi} d\chi \int_0^{\infty} d\zeta\, \zeta^3 \int_{-\pi/2}^{\pi/2} d\omega W_1 e^{i(m-n)\frac{\omega}{2}} \begin{pmatrix} \cos(\chi+\phi) \\ \sin(\chi+\phi) \end{pmatrix}_i \begin{pmatrix} \cos(\chi+\phi) \\ \sin(\chi+\phi) \end{pmatrix}_j}^s,$$

$$\overline{\tilde{I}^{(2)}_{ij,nm}}^s = \overline{L^4 e^{i(n+m)\phi} \int_0^{2\pi} d\chi \int_0^{\infty} d\zeta\, \zeta^3 \int_{\pi/2}^{3\pi/2} d\omega \tilde{W}_1 e^{i(m-n)\frac{\omega}{2}} e^{i(m+n)\frac{\pi}{2}} \times \begin{pmatrix} \cos(\chi+\phi) \\ \sin(\chi+\phi) \end{pmatrix}_i \begin{pmatrix} \cos(\chi+\phi) \\ \sin(\chi+\phi) \end{pmatrix}_j}^s,$$

$$\overline{J^{(2)}_{ij,nm}}^s = \overline{L^4 e^{i(n+m)\phi} \int_0^{2\pi} d\chi \int_0^{\infty} d\zeta\, \zeta^3 \int_{-\pi}^{\pi} d\omega W_2 e^{-im\omega} \begin{pmatrix} \cos(\chi+\phi) \\ \sin(\chi+\phi) \end{pmatrix}_i \begin{pmatrix} \cos(\chi+\phi) \\ \sin(\chi+\phi) \end{pmatrix}_j}^s. \tag{B10}$$

Projection on the s-th Fourier mode yields

$$\frac{1}{2\pi} \int_0^{2\pi} e^{is\phi} e^{i(n+m)\phi} \begin{pmatrix} \cos(\chi+\phi) \\ \sin(\chi+\phi) \end{pmatrix}_i \begin{pmatrix} \cos(\chi+\phi) \\ \sin(\chi+\phi) \end{pmatrix}_j d\phi = \begin{pmatrix} \frac{e^{2\chi}\delta_{n,s-m-2} + 2\delta_{n,s-m} + e^{-2\chi}\delta_{n,s-m+2}}{4} & \frac{e^{2\chi}\delta_{n,s-m-2} - e^{-2\chi}\delta_{n,s-m+2}}{4i} \\ \frac{e^{2\chi}\delta_{n,s-m-2} - e^{-2\chi}\delta_{n,s-m+2}}{4i} & -\frac{e^{2\chi}\delta_{n,s-m-2} - 2\delta_{n,s-m} + e^{-2\chi}\delta_{n,s-m+2}}{4} \end{pmatrix}. \tag{B11}$$

The spatial components of the second-order integrals are expressed as

$$\overline{I^{(2)}_{xx,nm}}^s + \overline{\tilde{I}^{(2)}_{xx,nm}}^s = L^4 G(1+a_3) \frac{S^{(1)}_{s,m}\delta_{n,s-m-2} + 2S^{(2)}_{s,m}\delta_{n,s-m} + S^{(3)}_{s,m}\delta_{n,s-m+2}}{4},$$

$$\overline{I^{(2)}_{xy,nm}}^s + \overline{\tilde{I}^{(2)}_{xy,nm}}^s = \overline{I^{(2)}_{yx,nm}} + \overline{\tilde{I}^{(2)}_{yx,nm}}^s = L^4 G(1+a_3) \frac{S^{(1)}_{s,m}\delta_{n,s-m-2} - S^{(3)}_{s,m}\delta_{n,s-m+2}}{4i},$$

$$\overline{I^{(2)}_{yy,nm}}^s + \overline{\tilde{I}^{(2)}_{yy,nm}}^s = -L^4 G(1+a_3) \frac{S^{(1)}_{s,m}\delta_{n,s-m-2} - 2S^{(2)}_{s,m}\delta_{n,s-m} + S^{(3)}_{s,m}\delta_{n,s-m+2}}{4},$$

$$\overline{J^{(2)}_{xx,nm}}^s = L^4 G(1+a_3) \frac{S^{(4)}_{s,m}\delta_{n,s-m-2} + 2S^{(5)}_{s,m}\delta_{n,s-m} + S^{(6)}_{s,m}\delta_{n,s-m+2}}{4},$$

$$\overline{J^{(2)}_{xy,nm}}^{s} = \overline{J^{(2)}_{yx,nm}}^{s} = L^4 G(1+a_3)\frac{S^{(4)}_{s,m}\delta_{n,s-m-2} - S^{(6)}_{s,m}\delta_{n,s-m+2}}{4i},$$
$$\overline{J^{(2)}_{yy,nm}}^{s} = -L^4 G(1+a_3)\frac{S^{(4)}_{s,m}\delta_{n,s-m-2} - 2S^{(5)}_{s,m}\delta_{n,s-m} + S^{(6)}_{s,m}\delta_{n,s-m+2}}{4}, \tag{B12}$$

where $a_3 = \Xi\left(1 - \frac{\tau_0(1+\tau_0^2)}{2}\right)$. Numerical evaluation of the coefficients $S^k_{s,m}$ for the relevant ranges of s and m yields

m	$S^{(1)}_{0,m}$	$S^{(2)}_{0,m}$	$S^{(3)}_{0,m}$	$S^{(4)}_{0,m}$	$S^{(5)}_{0,m}$	$S^{(6)}_{0,m}$
-2	$\frac{2}{9}$	$-\frac{2}{9}$	$-\frac{2}{15}$	$\frac{2}{9}$	$-\frac{2}{9}$	$-\frac{2}{15}$
-1	0	0	0	0	0	0
0	$\frac{2}{9}$	$\frac{2}{3}$	$\frac{2}{9}$	$\frac{2}{9}$	$\frac{2}{3}$	$\frac{2}{9}$
1	0	0	0	0	0	0
2	$-\frac{2}{15}$	$-\frac{2}{9}$	$\frac{2}{9}$	$-\frac{2}{15}$	$-\frac{2}{9}$	$\frac{2}{9}$

m	$S^{(1)}_{1,m}$	$S^{(2)}_{1,m}$	$S^{(3)}_{1,m}$	$S^{(4)}_{1,m}$	$S^{(5)}_{1,m}$	$S^{(6)}_{1,m}$
-2	$\frac{1}{9}$	$-\frac{5}{14}$	$-\frac{1}{7}$	$\frac{2}{9}$	$-\frac{2}{9}$	$-\frac{2}{15}$
-1	0	0	0	0	0	0
0	$\frac{14}{45}$	$\frac{26}{45}$	$\frac{1}{9}$	$\frac{2}{9}$	$\frac{2}{3}$	$\frac{2}{9}$
1	0	0	0	0	0	0
2	$-\frac{1}{11}$	0	$\frac{14}{45}$	$-\frac{2}{15}$	$-\frac{2}{9}$	$\frac{2}{9}$

m	$S^{(1)}_{2,m}$	$S^{(2)}_{2,m}$	$S^{(3)}_{2,m}$	$S^{(4)}_{2,m}$	$S^{(5)}_{2,m}$	$S^{(6)}_{2,m}$
-2	0	$-\frac{1}{3}$	$-\frac{1}{9}$	$\frac{2}{9}$	$-\frac{2}{9}$	$-\frac{2}{15}$
-1	0	0	0	0	0	0
0	$\frac{1}{3}$	$\frac{1}{3}$	0	$\frac{2}{9}$	$\frac{2}{3}$	$\frac{2}{9}$
1	0	0	0	0	0	0
2	0	$\frac{1}{3}$	$\frac{1}{3}$	$-\frac{2}{15}$	$-\frac{2}{9}$	$\frac{2}{9}$

The contribution to the evolution equation for P_s is given by

$$\begin{aligned}T^{(3)}_{ij,nm} =& L^4 G\,(1+a_3)\sum_{n,m}\Bigg[S^{(1)}_{s,m}\delta_{n,s-m-2}\frac{1}{8}\left(\frac{A_{xx,nm}-A_{yy,nm}}{4}+\frac{A_{xy,nm}+A_{yx,nm}}{4i}\right)\\ &+S^{(2)}_{s,m}\delta_{n,s-m}\frac{A_{xx,nm}+A_{yy,nm}}{16}\\ &+S^{(3)}_{s,m}\delta_{n,s-m+2}\frac{1}{8}\left(\frac{A_{xx,nm}-A_{yy,nm}}{4}+\frac{A_{xy,nm}+A_{yx,nm}}{4i}\right)\\ &+S^{(4)}_{s,m}\delta_{n,s-m-2}P_n\left(\frac{\nabla_x\nabla_y 2P_m-\nabla_y^2 P_m}{4}+\frac{\nabla_x\nabla_y P_m}{2i}\right)\\ &+S^{(5)}_{s,m}\delta_{n,s-m}P_n\frac{\nabla_x^2 P_m-\nabla_y^2 P_m}{4}\\ &+S^{(6)}_{s,m}\delta_{n,s-m+2}P_n\left(\frac{\nabla_x\nabla_y 2P_m-\nabla_y^2 P_m}{4}+\frac{\nabla_x\nabla_y P_m}{2i}\right)\Bigg].\end{aligned} \tag{B13}$$

Term $T^{(4)}_{i,nm}$

This term is proportional to ξ^0 and n^1. According to (3.15):

$$T^{(4)}_{i,nm}=\sum_{n,m=-\infty}^{\infty}\left[\frac{1}{2}\eta L\overline{K^{(1)}_{i,nm}}^{s}B_{i,nm}\right]. \tag{B14}$$

Relevant integrals are given by

$$\begin{aligned}\overline{K^{(1)}_{j,nm}}^{s} =& \overline{L^2 e^{i(n+m)\phi}\int_0^{2\pi}d\chi\int_0^{\infty}d\zeta\,\zeta\int_{\frac{\pi}{2}}^{\frac{3\pi}{2}}d\omega\tilde{W}_1}\\ &\overline{\times e^{i(m-n)\frac{\omega}{2}}e^{i(m+n)\frac{\pi}{2}}\begin{pmatrix}\cos(\phi)\\ \sin(\phi)\end{pmatrix}_j}^{s},\end{aligned} \tag{B15}$$

Projection on the s-th Fourier mode yields:

$$\begin{aligned}\overline{K^{(1)}_{j,nm}}^{s} =& L^2\int_0^{2\pi}d\chi\int_0^{\infty}d\zeta\,\zeta\int_{\frac{\pi}{2}}^{\frac{3\pi}{2}}d\omega\tilde{W}_1 e^{i(m-n)\frac{\omega}{2}}e^{i(m+n)\frac{\pi}{2}}\\ &\times\begin{bmatrix}\left(\delta_{n,s-m-1}+\delta_{n,s-m+1}\right)/2\\ \left(\delta_{n,s-m-1}-\delta_{n,s-m+1}\right)/(2i)\end{bmatrix}_j,\end{aligned} \tag{B16}$$

The spatial components of these integrals are conveniently expressed as

$$\begin{aligned}\overline{K^{(1)}_{x,nm}}^{s} &= L^2 G(1+a_1)\frac{S^{(1)}_{s,m}\delta_{n,s-m-1}+S^{(2)}_{s,m}\delta_{n,s-m+1}}{2},\\ \overline{K^{(1)}_{y,nm}}^{s} &= L^2 G(1+a_1)\frac{S^{(1)}_{s,m}\delta_{n,s-m-1}-S^{(2)}_{s,m}\delta_{n,s-m+1}}{2i},\end{aligned} \tag{B17}$$

where $a_1 = \Xi(1-\tau_0)$, and $S^k_{s,m}$ are just coefficients. Numerical evaluation of the coefficients $S^k_{s,m}$ for the relevant ranges of s and m yields

m	$S^{(1)}_{1,m}$	$S^{(2)}_{1,m}$
-2	$-\frac{2}{3}$	-1
-1	-1	$\frac{2}{3}$
0	2	1
1	-1	-2
2	$-\frac{2}{3}$	1

.

The contribution of described integrals to the evolution equation for P_s can now be written as

$$T^{(4)}_{i,nm} = \frac{L^3\eta}{2} G(1+a_1) \sum_{n,m} \left[S^{(1)}_m \delta_{n,s-m-1} \left(\frac{B_{x,nm}}{2} + \frac{B_{y,nm}}{2i} \right) + S^{(2)}_m \delta_{n,s-m+1} \left(\frac{B_{x,nm}}{2} - \frac{B_{y,nm}}{2i} \right) \right]. \tag{B18}$$

Term $T^{(5)}_{ij,nm}$

This term is proportional to ξ^0 and n^2.

$$T^{(5)}_{ij,nm} = \sum_{n,m=-\infty}^{\infty} \left[\frac{1}{8} \eta^2 L^2 \overline{K^{(2)}_{ij,nm}}^{\,s} B_{ij,nm} \right]. \tag{B19}$$

Associated integrals are given by

$$\overline{K^{(2)}_{ij,nm}}^{\,s} = \overline{L^2 e^{i(n+m)\phi} \int_0^{2\pi} d\chi \int_0^{\infty} d\zeta\, \zeta \int_{\pi/2}^{3\pi/2} d\omega \tilde{W}_1 e^{i(m-n)\frac{\omega}{2}} e^{i(m+n)\frac{\pi}{2}} \times \begin{pmatrix} \cos(\phi) \\ \sin(\phi) \end{pmatrix}_i \begin{pmatrix} \cos(\phi) \\ \sin(\phi) \end{pmatrix}_j}^{\,s}, \tag{B20}$$

Projection on the s-th Fourier mode yields

$$\frac{1}{2\pi} \int_0^{2\pi} e^{is\phi} e^{i(n+m)\phi} \begin{pmatrix} \cos(\phi) \\ \sin(\phi) \end{pmatrix}_i \begin{pmatrix} \cos(\phi) \\ \sin(\phi) \end{pmatrix}_j d\phi = \begin{pmatrix} \frac{\delta_{n,s-m-2} + 2\delta_{n,s-m} + \delta_{n,s-m+2}}{4} & \frac{\delta_{n,s-m-2} - \delta_{n,s-m+2}}{4i} \\ \frac{\delta_{n,s-m-2} - \delta_{n,s-m+2}}{4i} & -\frac{\delta_{n,s-m-2} - 2\delta_{n,s-m} + \delta_{n,s-m+2}}{4} \end{pmatrix}. \tag{B21}$$

The spatial components of the second-order integrals are expressed as

$$\begin{aligned}
\overline{K^{(2)}_{xx,nm}}^{s} &= L^2 G(1+a_1)\frac{S^{(1)}_{s,m}\delta_{n,s-m-2} + 2S^{(2)}_{s,m}\delta_{n,s-m} + S^{(3)}_{s,m}\delta_{n,s-m+2}}{4},\\
\overline{K^{(2)}_{xy,nm}}^{s} &= \overline{K^{(2)}_{yx,nm}}^{s} = L^2 G(1+a_1)\frac{S^{(1)}_{s,m}\delta_{n,s-m-2} - S^{(3)}_{s,m}\delta_{n,s-m+2}}{4i},\\
\overline{K^{(2)}_{yy,nm}}^{s} &= -L^2 G(1+a_1)\frac{S^{(1)}_{s,m}\delta_{n,s-m-2} - 2S^{(2)}_{s,m}\delta_{n,s-m} + S^{(3)}_{s,m}\delta_{n,s-m+2}}{4}.
\end{aligned} \tag{B22}$$

where $a_1 = \Xi(1-\tau_0)$, and the coefficients $S^k_{s,m}$ are given by Numerical evaluation of these coefficients for the relevant ranges of s and m yields

m	$S^{(1)}_{0,m}$	$S^{(2)}_{0,m}$	$S^{(3)}_{0,m}$	$S^{(1)}_{2,m}$	$S^{(2)}_{2,m}$	$S^{(3)}_{2,m}$
-2	1	$-\frac{2}{3}$	-1	$-\frac{2}{3}$	-1	$-\frac{2}{15}$
-1	-2	-1	$\frac{2}{3}$	-1	$\frac{2}{3}$	1
0	1	2	1	2	1	$-\frac{2}{3}$
1	$\frac{2}{3}$	-1	-2	-1	-2	-1
2	-1	$-\frac{2}{3}$	1	$-\frac{2}{3}$	1	2

The contribution to the evolution equation for P_s is given by

$$\begin{aligned}
T^{(5)}_{ij,nm} =& \frac{L^4\eta^2}{8} G\,(1+a_1)\sum_{n,m}\Bigg[S^{(1)}_{s,m}\delta_{n,s-m-2}\left(\frac{B_{xx,nm}-B_{yy,nm}}{4} + \frac{B_{xy,nm}+B_{yx,nm}}{4i}\right)\\
&+ S^{(2)}_{s,m}\delta_{n,s-m}\frac{B_{xx,nm}+B_{yy,nm}}{2}\\
&+ S^{(3)}_{s,m}\delta_{n,s-m+2}\left(\frac{B_{xx,nm}-B_{yy,nm}}{4} + \frac{B_{xy,nm}+B_{yx,nm}}{4i}\right)\Bigg].
\end{aligned} \tag{B23}$$

Term $T^{(6)}_{ij,nm}$

This term is proportional to ξ^0 and n^2.

$$T^{(6)}_{ij,nm} = \sum_{n,m=-\infty}^{\infty}\left[\frac{1}{4}\eta L\overline{F^{(2)}_{ij,nm}}^{s} C_{ij,nm}\right] \tag{B24}$$

Associated integrals are given by

$$\overline{F^{(2)}_{ij,nm}}^{s} = \overline{L^2 e^{i(n+m)\phi}\int_0^{2\pi} d\chi \int_0^{\infty} d\zeta\, \zeta^2 \int_{\pi/2}^{3\pi/2} d\omega \tilde{W}_1 e^{i(m-n)\frac{\omega}{2}} e^{i(m+n)\frac{\pi}{2}}}$$

$$\times \begin{pmatrix} \cos(\phi) \\ \sin(\phi) \end{pmatrix}_i \begin{pmatrix} \cos(\chi+\phi) \\ \sin(\chi+\phi) \end{pmatrix}_j \Bigg)^s, \tag{B25}$$

Projection on the s-th Fourier mode yields

$$\frac{1}{2\pi}\int_0^{2\pi} e^{is\phi} e^{i(n+m)\phi} \begin{pmatrix} \cos(\phi) \\ \sin(\phi) \end{pmatrix}_i \begin{pmatrix} \cos(\phi+\chi) \\ \sin(\phi+\chi) \end{pmatrix}_j d\phi = \begin{pmatrix} \frac{e^{i\chi}\delta_{n,s-m-2}+\delta_{n,s-m}(e^{i\chi}+e^{-i\chi})+e^{-i\chi}\delta_{n,s-m+2}}{4} & \frac{e^{i\chi}\delta_{n,s-m-2}-e^{-i\chi}\delta_{n,s-m+2}}{4i} \\ \frac{e^{i\chi}\delta_{n,s-m-2}-e^{-i\chi}\delta_{n,s-m+2}}{4i} & -\frac{e^{i\chi}\delta_{n,s-m-2}-\delta_{n,s-m}(e^{i\chi}+e^{-i\chi})+e^{-i\chi}\delta_{n,s-m+2}}{4} \end{pmatrix}. \tag{B26}$$

(terms proportional to $(e^{i\chi}-e^{-i\chi})$ are excluded from the previous expression since they eventually disappear).

The spatial components of the integrals are expressed as

$$\begin{aligned} \overline{K^{(2)}_{xx,nm}}^s &= L^3 G(1+a_1)\frac{S^{(1)}_{s,m}\delta_{n,s-m-2}+2S^{(2)}_{s,m}\delta_{n,s-m}+S^{(3)}_{s,m}\delta_{n,s-m+2}}{4}, \\ \overline{K^{(2)}_{xy,nm}}^s &= L^3 G(1+a_1)\frac{S^{(1)}_{s,m}\delta_{n,s-m-2}-S^{(3)}_{s,m}\delta_{n,s-m+2}}{4i}, \\ \overline{K^{(2)}_{yy,nm}}^s &= -L^3 G(1+a_1)\frac{S^{(1)}_{s,m}\delta_{n,s-m-2}-2S^{(2)}_{s,m}\delta_{n,s-m}+S^{(3)}_{s,m}\delta_{n,s-m+2}}{4}. \end{aligned} \tag{B27}$$

where $a_2 = \Xi\,(1-\tau_0^2)$. Numerical evaluation of these coefficients $S^k_{s,m}$ for the relevant ranges of s and m yields

m	$S^{(1)}_{1,m}$	$S^{(2)}_{1,m}$	$S^{(3)}_{1,m}$
-2	$\frac{1}{22}$	$-\frac{3}{14}$	$-\frac{1}{7}$
-1	$-\frac{17}{44}$	$-\frac{1}{22}$	$-\frac{3}{14}$
0	$\frac{17}{44}$	$\frac{17}{44}$	$\frac{1}{22}$
1	$-\frac{1}{22}$	$-\frac{17}{44}$	$-\frac{17}{44}$
2	$-\frac{3}{14}$	$\frac{1}{22}$	$\frac{17}{44}$

.

The contribution to the evolution equation for P_s is given by

$$\begin{aligned} T^{(5)}_{ij,nm} =& \frac{L^4\eta}{4} G a_2 \sum_{n,m}\Bigg[S^{(1)}_{s,m}\delta_{n,s-m-2}\left(\frac{C_{xx,nm}-C_{yy,nm}}{4}+\frac{C_{xy,nm}+C_{yx,nm}}{4i}\right) \\ &+ S^{(2)}_{s,m}\delta_{n,s-m}\frac{C_{xx,nm}+C_{yy,nm}}{2} \end{aligned}$$

$$+ S^{(3)}_{s,m}\delta_{n,s-m+2}\left(\frac{C_{xx,nm} - C_{yy,nm}}{4} + \frac{C_{xy,nm} + C_{yx,nm}}{4i}\right)\Bigg]. \tag{B28}$$